



Numerical Simulation of the 3D Flow around Junctions

VU Minh Tuan

Master Thesis

presented in partial fulfillment
of the requirements for the double degree:
“Advanced Master in Naval Architecture” conferred by University of Liege
“Master of Sciences in Applied Mechanics, specialization in Hydrodynamics,
Energetics and Propulsion” conferred by Ecole Centrale de Nantes

Developed at University of Galati, Galati in the framework of the

**“EMSHIP”
Erasmus Mundus Master Course
in “Integrated Advanced Ship Design”**

Ref. 159652-1-2009-1-BE-ERA MUNDUS-EMMC

Supervisor : Prof. Adrian Lungu, "Dunarea de Jos" University of Galati
Reviewer: Prof. Pierre Ferrant, Ecole Centrale de Nantes

Galati, January 2012



Traditio et innovatio



Zachodniopomorski
Uniwersytet
Technologiczny
w Szczecinie

This page is intentionally left blank

ABSTRACT

When an oncoming boundary layer flow encounters an appendage fixed on the plate, the flow separates in front of the body due to the blocking effect. The separated flow forms several vortices around the body, which are called horseshoe vortices because their top view looks like a horseshoe. The flow is completely 3D and becomes complicated as the horseshoe vortex interacts with the boundary layer developed on the body surface. This convoluted three-dimensional flow has been called a juncture flow. Juncture flow can affect the lift and stability/control characteristics of appendages through the generation of horseshoe vortices from these appendages. In spite of its engineering importance, there is no established method for estimating the appendage resistance or wake characteristics since the detailed mechanism of the juncture flow is not fully understood. Although some systematic experimental studies have been performed through conventional tests, the estimation of the resistance is hampered by the uncertainty associated with the scale effect. The flow complexity is due to the number of vortices originating upstream of the strut. These vortices result from the separation of the boundary layer due to the adverse pressure gradient in front of the strut. Creation of the vortex system in front of the circular cylinder is clearly seen in the famous photograph taken by Sutton where an array of vortices is visualized with the injection of smoke. Sutton's photograph has helped clarify the horseshoe vortex system. The number of vortices increases as the Reynolds number is increased or the thickness of the oncoming boundary layer decreases. Although many experimental studies have been conducted to understand the structure of the horseshoe vortex system, the precise flow topology is still controversial due to the lack of resolution in experimental data. However, rapid advances in computing technology have cleared the road to simulate the flow by solving the RANS equations.

The master thesis focuses on the numerical simulation of 3D flow around junctures, in which the unsteady nature of the flow represents the main point of interest. Various geometries of the juncture are investigated to grasp a better understanding of the phenomena and develop proper modeling techniques. Besides, the study also focuses on the free-surface influence on the overall hydrodynamic field around the juncture.

In the first part of the thesis, the theoretical aspects of the numerical approach are briefly described. The governing equations and the initial and boundary conditions are presented. In addition, some quantities which are used to estimate and evaluate the solutions of the governing equations are also mentioned. Emphasis is put on the turbulence treatment. A comparison between different turbulence models is performed to motivate the choice for the Spalart-Allmaras model, which proved to be the most suitable one for this work. The validation of the computed solution is achieved through comparisons with the experimental data provided by the literature.

The second part of the work discusses the 3D flow around a circular cylinder mounted on a plate. The characteristics of the flow around a circular cylinder such as Reynolds and Strouhal numbers, vortex shedding, drag and lift coefficients are also pointed out specifically. In these cases, the free surface effect is not taken into account. The shape of plate is changed ranging from the flat one to a concave or a convex one. For each geometric configuration of the plate, the circular cylinder will be inclined with various aspect angles (10° , 20° and 30°) longitudinally and laterally. All simulation cases are done for two different Reynolds numbers of 3900, and 1 million, respectively.

In the third part, the unsteady simulation is performed at Reynolds number of 3,900. Only the circular cylinder mounted on the convex plate and inclined laterally is studied and the numerical solution is compared with the cases of the steady flow corresponding case. Besides, once again, these simulations do not take into account the effect of free surface. The mechanism of vortex shedding will be unveiled by the results of this simulation.

Finally, several conclusions outline the achievements and findings of the work, drawing out the potential directions for further studies.

CONTENT

1. INTRODUCTION	1
1.1. Aim of work	2
1.2. Objectives of work	2
1.3. Methodology of work	3
1.4. Thesis structure	3
2 . MATHEMATICAL MODEL	5
2.1. Overview	5
2.2. Numerical approach	5
2.2.1. <i>Governing equations</i>	6
2.2.2. <i>Turbulence models</i>	8
2.2.3. <i>Initial and boundary conditions</i>	17
2.3. Discretization	18
2.3.1. <i>Spatial discretization</i>	18
2.3.2. <i>Temporal discretization</i>	22
2.3.3. <i>Quality of discretization</i>	23
2.4. Summary	25
3. GRID GENERATION	26
3.1. Overview of grid	26
3.1.1. <i>Grid topology</i>	26
3.1.2. <i>Input parameter of grid generation</i>	27
3.1.3. <i>The process of grid generation</i>	29
3.2. Models of the problem	32
3.2.1. <i>Turbulence parameters of simulation</i>	32
3.2.2. <i>Choosing the turbulence models and the mesh</i>	33
3.3. Conclusion	40
4. FLOW AROUND A CIRCULAR CYLINDER	41
4.1. Conceptual overview of flow around a circular cylinder	42
4.1.1. <i>Reynolds number</i>	42
4.1.2. <i>Vortex shedding</i>	46
4.1.3. <i>Strouhal number</i>	47
4.1.4. <i>Drag and lift coefficients</i>	49
4.1.5. <i>Pressure coefficient</i>	51

4.2. Flow around a circular cylinder mounted on the flat plate	52
4.2.1. <i>CFD simulation</i>	52
4.2.2. <i>The results and discussions</i>	53
4.3. Flow around a circular cylinder mounted on the curved plate	62
4.3.1. <i>CFD simulation</i>	62
4.3.2. <i>The results and discussions</i>	63
4.4. Conclusion	78
5. UNSTEADY NUMERICAL SIMULATION	79
5.1. Introduction	79
5.2. 3-D computational domain and boundary conditions	79
5.3. 3-D mesh	79
5.4. Modeling turbulent flow	80
5.5. Simulation results and discussions	80
5.5.1. <i>Flow field</i>	80
5.5.2. <i>Drag coefficients</i>	82
6. FINAL CONCLUSIONS AND FUTURE WORK	84
6.1. Conclusions and remarks	84
6.2. Future work	85
7. ACKNOWLEDGEMENTS	87
8. REFERENCES	88

LIST OF FIGURES

Figure 2.1. The classification of turbulence models	8
Figure 2.2. Time averaging of turbulence using RANS models	10
Figure 2.3: An example of structured mesh	19
Figure 2.4: An example of unstructured mesh	19
Figure 2.5: An example of hybrid mesh	20
Figure 2.6. An explicit finite difference module	22
Figure 2.7. An implicit finite difference module	22
Figure 2.8. Relationship between qualities of discretization	23
Figure 3.1. Grid topology around the cylinder	27
Figure 3.2. Structure of near-wall layers	28
Figure 3.3. The computational domain	30
Figure 3.4. One kind of the meshes of computational domain	31
Figure 3.5. Domains to model the flow around a circular cylinder	34
Figure 3.6. Some types of mesh used to calculate the flow around a circular cylinder	36
Figure 4.1. Regimes of flow around a smooth, circular cylinder in steady current	44
Figure 4.2. Formation and development of vortex shedding in the wake region of the flow around a circular cylinder	47
Figure 4.3. Strouhal number for a smooth circular cylinder. Experimental data from: Solid curve: William (1989). Dashed curve: Roshko (1961). Dots: Schewe (1983).	48
Figure 4.4. Sketch showing positions of separation points at different separation regimes	48
Figure 4.5. Forces acting on the cylinder	49
Figure 4.6. Drag coefficient for cylinders (1) and spheres (2) as a function of Reynolds number (Re), Polezhaev et al. (2003)	51
Figure 4.7. Experimental pressure coefficient distributions on cylinder surface compared to theoretical result, Roshko (1960)	52
Figure 4.8. Front view of the horseshoe vortex at $Re=3,900$	54
Figure 4.9. Rear view of the horseshoe vortex at $Re=3,900$	55
Figure 4.10. The vortex structure in front of the cylinder	55
Figure 4.11. Flow topology around the cylinder at $Re = 3,900$	57
Figure 4.12. Pressure fields around a circular cylinder mounted inclined longitudinally on a flat plate	58

Figure 4.13. Pressure fields around a circular cylinder mounted inclined laterally on a flat plate	58
Figure 4.14. Front view of the horseshoe vortex at $Re=10^6$	59
Figure 4.15. Rear view of the horseshoe vortex at $Re=10^6$	59
Figure 4.16. Streamtraces pattern upstream the cylinder for $Re = 10^6$	60
Figure 4.17. Pressure fields around a circular cylinder mounted inclined longitudinally on a flat plate	61
Figure 4.18. Pressure fields around a circular cylinder mounted inclined laterally on a flat plate	61
Figure 4.19. Curvature influence on the pressure distribution on a juncture flow in concave plate case	64
Figure 4.20. Curvature influence on the pressure distribution on a juncture flow in convex plate case	64
Figure 4.21. Transversal streamlines around the juncture	65
Figure 4.22. Curvature influence on the drag coefficient of the cylinder mounted on the concave plate and inclined upstream	66
Figure 4.23. Curvature influence on the drag coefficient of the cylinder mounted on the concave plate and inclined downstream	66
Figure 4.24. Curvature influence on the drag coefficient of the cylinder mounted on the concave plate and inclined laterally	67
Figure 4.25. Curvature influence on the drag coefficient of the cylinder mounted on the convex plate and inclined upstream	67
Figure 4.26. Curvature influence on the drag coefficient of the cylinder mounted on the convex plate and inclined downstream	68
Figure 4.27. Curvature influence on the drag coefficient of the cylinder mounted on the convex plate and inclined laterally	68
Figure 4.28. Inclination angle influence on the drag coefficient of the cylinder in flat plate case	69
Figure 4.29. Inclination angle influence on the drag coefficient of the cylinder in concave plate case	69
Figure 4.30. Inclination angle influence on the drag coefficient of the cylinder in convex plate case	69
Figure 4.31. Viscous drag coefficient variation with the inclination angle in flat plate	70

Figure 4.32. Curvature influence on the pressure distribution on a juncture flow in concave plate case	71
Figure 4.33. Curvature influence on the pressure distribution on a juncture flow in convex plate case	71
Figure 4.34. Transversal streamlines around the juncture	72
Figure 4.35. Curvature influence on the drag coefficient of the cylinder mounted on the concave plate and inclined upstream	73
Figure 4.36. Curvature influence on the drag coefficient of the cylinder mounted on the concave plate and inclined downstream	73
Figure 4.37. Velocity fields	74
Figure 4.38. Curvature influence on the drag coefficient of the cylinder mounted on the concave plate and inclined laterally	75
Figure 4.39. Curvature influence on the drag coefficient of the cylinder mounted on the convex plate and inclined upstream	75
Figure 4.40. Curvature influence on the drag coefficient of the cylinder mounted on the convex plate and inclined downstream	75
Figure 4.41. Curvature influence on the drag coefficient of the cylinder mounted on the convex plate and inclined laterally	76
Figure 4.42. Inclination angle influence on the drag coefficient of the cylinder in flat plate case	76
Figure 4.43. Inclination angle influence on the drag coefficient of the cylinder in concave plate case	77
Figure 4.44. Inclination angle influence on the drag coefficient of the cylinder in convex plate case	77
Figure 4.45. Viscous drag coefficient variation with the inclination angle in flat plate case	77
Figure 5.1. Mesh domain	79
Figure 5.2. Comparison of velocity contours at different flow time	80
Figure 5.3. The pressure field around the cylinder	81
Figure 5.4. The flow topology around the cylinder at $Re = 3,900$	81
Figure 5.5. The velocity vectors existing near the cylinder	82
Figure 5.6. Drag coefficient	82
Figure 5.7. Lift coefficient	83

LIST OF TABLES

Table 3.1. The number of cells in each Grid	37
Table 3.2. Drag coefficient of the flow around a circular cylinder using the RANS turbulence models with 2D computational domain and $Re = 3900$	38
Table 3.3. Drag coefficient of the flow around a circular cylinder using the RANS turbulence models with 2D computational domain and $Re = 1,000,000$	39
Table 3.4. Drag coefficient of the flow around a circular cylinder using the RANS turbulence models with 3D computational domain and $Re = 1,000,000$	40
Table 4.1. Summary of cylinder flow regimes	43
Table 5.1. The total drag coefficients	82

DECLARATION OF AUTHORSHIP

I declare that this thesis and the work presented in it are my own and have been generated by me as the result of my own original research.

Where I have consulted the published work of others, this is always clearly attributed.

Where I have quoted from the work of others, the source is always given. With the exception of such quotations, this thesis is entirely my own work.

I have acknowledged all main sources of help.

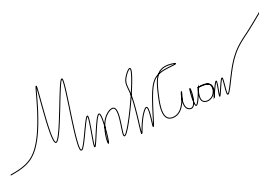
Where the thesis is based on work done by myself jointly with others, I have made clear exactly what was done by others and what I have contributed myself.

This thesis contains no material that has been submitted previously, in whole or in part, for the award of any other academic degree or diploma.

I cede copyright of the thesis in favor of the University of Galati

Date: 25th January 2012

Signature

A handwritten signature in black ink, appearing to read 'M. M. Tuon', written in a cursive style.

1. INTRODUCTION

Junction flow occurs when a boundary layer encounters an obstacle mounted on the same surface. Practically, there are a lot of obstacle-surfaces where junction flow exists, such as building-ground, pier-riverbed, wing-body of an aircraft and keel-hull of ship. Junction flow is characterized by three dimensional boundary layer separation and vortices that wrap around the obstacle. The origin of the boundary layer separation and the vortices formation is caused by the adverse pressure gradient.

Junction flow determines two kinds of vortices: one is the so-called horseshoe vortex, which is formed in front of the obstacle, and the other is the free vortex formed at the lee side of it. The horseshoe vortex is caused by the rotation in the incoming flow: the boundary layer on the plate, upstream of the strut, undergoes a three-dimensional separation under the influence of the adverse pressure gradient produced by the strut, and the separated boundary layer rolls up to form a swirling vortex around the strut, which then trails downstream. The lee-side vortices, on the other hand, are caused by the rotation in the boundary layer over the surface of the strut: the shear layers emanating from the side edges of the strut roll up to form these vortices.

The presence of the horseshoe and the lee-side vortices has usually an unfavorable effect in the practice of engineering. In civil engineering for instance, soil, sands and rocks in the upstream vicinity of a pier foundation are scoured away by the horseshoe vortices, which threaten the safety of the bridge, Ahmed F. et al. (1998). In naval architecture the significant unsteadiness of the horseshoe vortex system in front of the keel-hull junction of the ship engenders noise and vibration, which, from the naval viewpoint, should be restricted as much as possible, Devenport W. J. et al. (1992). Because of such problems, the junction flow has been investigated quite extensively.

The most studied blunt body is the circular cylinder, so one of the most reported juncture in literature is the one between a cylinder and a plate. Not only the wide area of applications, but also and the complex vortex dynamics have stimulated extensive studies on such junction flow, as reviewed recently by Simpson (2001). Baker (1979) investigated systematically the laminar junction flow around the cylinder-plate junction and gave the variation of the horseshoe vortex number with the Reynolds number. Davenport and Simpson (1990) found the bimodal structure of the turbulent junction flow. Wei et al. (2001) visualized the multiple-frequency phenomena at Reynolds numbers in the range of 5,000-8,000, and pointed out that the energy of the horseshoe vortices came mainly from the separated shear layer. Sumner et

al. (2004) and Pattenden et al. (2005) proved that the wake structure and the power spectrum of the low aspect-ratio junction flow were different from those of the large aspect-ratio one. Martinuzzi and Tropea (1993) as well as Chou and Chao (2000) noticed the horseshoe vortex breached if the aspect-ratio of the cylinder is small enough.

Regarding the lee-wake vortex flow, an extensive volume of knowledge has accumulated over the past two decades on the two-dimensional vortex flow behind a free cylinder subject to an oscillatory flow (see e.g. Sarpkaya & Isaacson (1981); Bearman et al. (1981); Williamson (1985)) and the complex behavior of vortex motions in various regimes is well understood.

Although much effort has been put into the study of the classic juncture flows, it appears that no consistent studies have been conducted to investigate the influence of the geometry, i.e. the cylinder inclination or the plate curvature, on the overall pattern of the flow. However, rapid advances in computing technology have cleared the road to simulate the flow by solving the RANS equations.

The present study aims at providing a grasp of understanding of the flow structure around such junctures. In the beginning several numerical simulations are carried out in which various turbulence treatments are considered to find out the advantages and disadvantages of each turbulence model, based on comparisons with experimental data. Several configurations of the circular cylinder mounted straight or inclined at various angles on plane or curved plates is then carried out to clarify the influence of the geometry on the flow structure.

1.1. Aim of work

The main aim of the work is to investigate numerically the viscous flow around 3D junctures by using the commercial computer software FLUENT. Comparative analyses between the numerical solutions and the experimental data are done to validate the accuracy of the theoretic approach.

1.2. Objectives of work

To achieve the above aims, three principal objectives are targeted:

- Studies of the viscous flow around a 3D circular cylinder mounted on the flat plate. Two different Reynolds numbers of 3,900 and 1,000,000 have been tested to check the capability of different turbulent models. Qualitative assertions on the vortex shedding phenomenon, drag calculation and pressure distribution on the solid boundaries will be done. To validate the advanced modeling approaches as well as to find the most suitable turbulent model used in the simulation, the results of research shall be compared with those of experiment data.

- Investigation of the viscous flow around a 3D inclined circular cylinder mounted on the flat plate. The circular cylinder is inclined in the XZ and YZ planes with the different angles of 10°, 20° and 30°, respectively. Various Reynolds numbers (3,900 and 1,000,000) will be tested to find out the effect of cylinder inclination on the flat plate. The force coefficient will be computed. Besides, the numerical results will be compared with experimental measurements and other numerical results to validate the present work.
- Studies of the viscous flow around a 3D circular cylinder mounted on the curved plate with the different curvatures, and, the circular cylinder inclined in XZ and YZ planes with the different angles of 10°, 20° and 30°, respectively. The turbulence model chosen before will be tested at two Reynolds numbers of 3,900, and 1,000,000 respectively.

1.3. Methodology of work

To reach the above-mentioned objectives, the work will be conducted in several successive steps, all being based on using the FLUENT solver. Firstly, simulating the viscous flow around a circular cylinder mounted on the flat plate at different Reynolds numbers will be done. The behavior of viscous flow will be investigated by inclining and rotating the cylinder in the different plane with various angles such 10°, 20° and 30°. To verify the modeling approach, the results of these simulations will be compared with those of the experiment which was carried out by Moin et al. (1995) and Zdravkovich (1997). This study is regarded as an initial stage for the further application of CFD on the complex flow at the later stage.

The next stage is represented by the simulation of the steady and unsteady viscous flow around the circular cylinder mounted on the curved plate, in an attempt to investigate the vortex shedding mechanism. This stage focuses on the behavior of vortices of the junction flow when the geometry of the computational domain is modified. An advanced CFD technique of grid generation is applied to bend the plate. The change of geometry includes the change of curvature of plate and the change of position of cylinder in the different plane. This idea was derived from the structure in practice. Obviously, the results of the simulation are compared with those of first stage and together.

1.4. Thesis structure

The content of the thesis is comprised of six chapters and a reference. The introductory chapter will introduce to the reader the objectives and the methodology of the research work. Chapter two discusses the principles of the computational fluid dynamics as well as the numerical approach of the turbulent flow. The governing equations describing the fluid motion are introduced. Several turbulent models that model the juncture flow are described.

The capability and limitations of each model in the applications of flow around juncture will be discussed. In last part of this chapter, some issues related to the consistency, stability and convergence will be discussed.

Chapter three describes the principles of grid generation. The steps that govern the problem are highlighted. Besides, the boundary conditions formulation is treated in there.

Chapter four contains the numerical investigation of the flow around a 3D circular cylinder mounted on the flat and curved plate based on solving the Reynolds Averaged Navier Stokes (RANS hereafter) at various Reynolds numbers. The drag and pressure distribution which are predicted from RANS solution will be compared with the experimental results. Then, this chapter focuses mainly on the influence of geometrical changes on the flow around a circular cylinder. This change includes the inclination of cylinder with various angles as well as the curvature of plate. The detailed comparisons of pressure and velocity profiles in the wake region of each other and with experimental data are also brought into focus.

Chapter five discusses the unsteady simulation of the flow around the cylinder inclined laterally and mounted on the convex plate. Throughout this simulation, the generated vortex shedding will be revealed. The results of this simulations will be presented by plotting the force coefficient, the contours of pressure distribution and velocity and they are compared those of the steady simulation.

Finally, chapter six brings out the final conclusions on the work done on this master thesis. It reiterates the main objectives of the work and the way they were attained. The second part of this chapter points out some suggestions and recommendations for the further study of the flow around junctures by using numerical methods.

2. MATHEMATICAL MODEL

In the followings the background theories of CFD as well as the techniques for solving the fluid flow problems are presented. The chapter contains of two main parts. The first part points out the governing equations describing fluid flow and the techniques used for solving these equations. Additional, the turbulence models which can be used for the study of flow around junctures will also introduced. The second part discusses how the governing equations are solved by discretization.

2.1. Overview

Flow always exists in two major regimes. They are either laminar or turbulent, depending on the Reynolds number. In practice as well as in engineering applications, most of the flows are turbulent. The laminar flow develops in parallel layers, with no disruption between the layers. There are no cross currents perpendicular to the direction of flow, nor eddies or swirls of fluids. Flows in the laminar regime are completely described by the continuity and momentum equations as it will be mentioned later in this chapter. In simple cases, they can be solved analytically. More complex flows, however, may have to be tackled numerically by making use of the CFD techniques. Inversely, turbulent flow is that flow regime which is characterized by recirculation, chaotic and stochastic property changes. It includes rapid variation of pressure and velocity in space and time.

Turbulence contains eddies with different dimensions which often rotate in motion. When observing the turbulence flow, various eddies are found out from large, average and small or tiny scales. The largest eddies, which are associated with the low frequency range of the energy spectrum, always transfer momentum and heat in a flow. The largest eddies interact with the mean flow, thus, they will extract kinetic energy from the mean flow and supply this energy to the smallest eddies where energy is dissipated by viscosity.

2.2. Numerical approach

In the past, there have been two approaches to uncover the laws of nature: a practical one and a theoretical one. The practical approach seeks to discover physical laws through observation aided by experiments and various devices and measuring instruments. The theoretical approach converts the laws of nature to relationships between mathematical quantities, most often employing the language of differential and integral calculus to describe how certain quantities change depending on others.

Both approaches, however, have their shortcomings. In certain areas, performing physical experiments waste a long time and is very expensive. Furthermore, they can be affected by

outside factors such as the weather, etc. On the other hand, mathematical equations that describe the physical world with reasonable accuracy are usually so complex that analytical solutions can no longer be obtained. Often an exact solution can be found only for considerably simplified models, such as those resorting to special symmetries or ignoring couplings between certain quantities.

To overcome these shortcomings of both the experimental and the theoretical approaches, numerical simulation has established itself in recent years as a third approach connecting the two traditional ones. Numerical simulation is characterized by the following procedure. From observations of the real world, mathematical equations are derived to valid at all (infinitely many) points in space and time. These equations are then discretized, i.e., considered at only a finite number of selected points. At these points, the underlying continuous equations are solved approximately.

2.2.1. Governing equations

The starting point of any numerical simulation method is the mathematical model, i.e. the set of partial differential or integro-differential equations and boundary conditions. This set of equations constitutes the so called governing equations. They contain the continuity, the momentum and the energy equations, which represent the conservation laws of physics.

- The mass of a fluid is conserved.
- The rate of change of momentum equals the sum of the forces on a fluid particle (Newton’s second law).
- The rate of change of energy is equal to the sum of the rate of heat addition to and the rate of work done on a fluid particle (first law of thermodynamics).

Moreover, the equations of state are also included to solve the set of differential equations completely and exactly.

2.2.1.1. The continuity equation

Equation based on the law of conservation of mass. Applying this concept to fluid flow, we ensure that the change of mass in a control volume is equal to the mass that enters through its faces minus the total mass leaving its faces.

Mass entering per unit time	=	Mass leaving per unit time	+	Increase of mass in the control volume per unit time
--------------------------------	---	-------------------------------	---	---

$$\frac{\partial u}{\partial x} + \frac{\partial v}{\partial y} + \frac{\partial w}{\partial z} = 0 \tag{Eq. 2.1}$$

2.2.1.2. The momentum equation

By applying Newton's Second Law of Motion, the momentum equation is expressed in terms of the pressure and viscous stresses acting on a particle in the fluid. This ensures that the rate of change of momentum of the fluid particles is equal to the total force due to surface stresses and body forces acting in an aligned direction of a chosen coordinate axis.

$$\frac{\partial u}{\partial t} + (u \cdot \nabla)u = -\frac{1}{\rho} \nabla p + F + \frac{\mu}{\rho} \nabla^2 u \quad \text{Eq. 2.2}$$

Where u is the fluid velocity vector, with components u , v , and w ,

p is the pressure,

ρ is the fluid mass density,

F is the external force per unit mass.

2.2.1.3. The energy equation

Based on the First Law of Thermodynamics, the rate of change of energy of a fluid particle is taken to be equal to the net rate of work done on that particle due to surface forces, heat and body forces such as gravitational force. The energy equation describes the transport of heat energy through a fluid and its effects.

$$\frac{\partial E}{\partial t} + \nabla \cdot (u(E + p)) = 0 \quad \text{Eq. 2.3}$$

Where $E = \rho e + \frac{1}{2} \rho (u^2 + v^2 + w^2)$ is the total energy per unit volume, with e being the internal energy per unit mass for fluid.

2.2.1.4. Navier-Stokes equations

Combining these fundamental principles, the physics of fluid flow is expressed in terms of a set of partial differential equations known as the Navier-Stokes equations. By solving these equations, the pressure and velocity of the fluid can be predicted throughout the flow.

$$\begin{aligned} \frac{\partial u}{\partial x} + \frac{\partial v}{\partial y} + \frac{\partial w}{\partial z} &= 0 \\ \frac{\partial u}{\partial t} + (u \cdot \nabla)u &= -\frac{1}{\rho} \nabla p + F + \frac{\mu}{\rho} \nabla^2 u \\ \frac{\partial E}{\partial t} + \nabla \cdot (u(E + p)) &= 0 \end{aligned} \quad \text{Eq. 2.4}$$

2.2.2. Turbulence models

As aforementioned, the remarkable feature of a turbulent flow is that the molecules move in a chaotic fashion along complex irregular paths. The strong chaotic motion leads to the various layers of the fluid to mix together intensely.

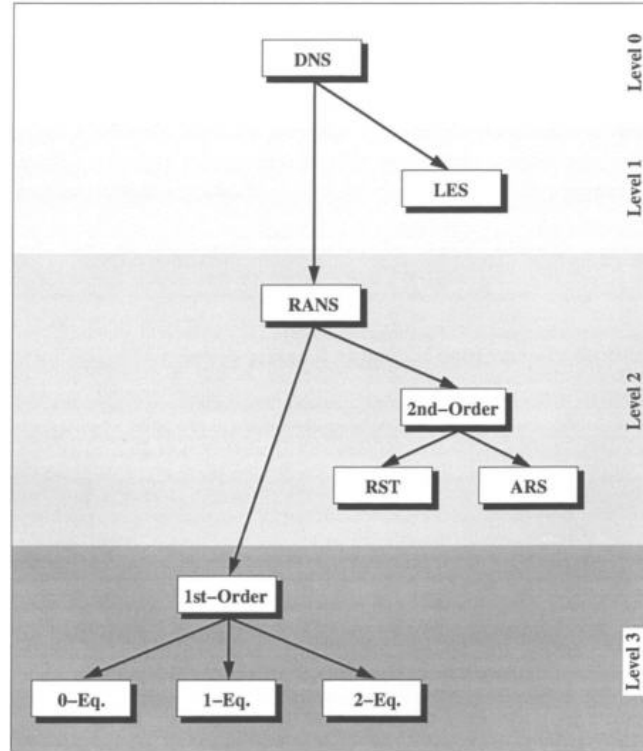


Figure 2.1. The classification of turbulence models [14]

LES: Large Eddy simulation

RST: Reynolds stress Transport models

ARS: Algebraic Reynolds-Stress models

Although the chaotic fluctuations of the flow variables are of deterministic nature, the simulation of turbulent flows still continues to present as a significant problem. A direct simulation of turbulence by the time-dependent Navier-Stokes equations, called Direct Numerical Simulation (DNS) has been used to model and solve the turbulent problem. However, it can only apply for rather simple flow cases at low Reynolds numbers because some restrictions appear when the number of grid points is too many. This does not mean that DNS is fully useless. DNS plays a vital role in the development and calibration of improved turbulence models. To overcome the shortcomings of DNS, a large variety of turbulence models was developed. Generally, the turbulence models can be classified as shown in Figure 2.1.

2.2.2.1. Large Eddy Simulation (LES)

LES is founded on the observation that the small scales of turbulent motion are more universal in character than the large eddies, which transport the turbulent energy. Therefore, the idea is to directly compute only the large eddies accurately and approximate the effects of the small scales, which are not resolved by the numerical scheme.

To classify between the large scales and small scales, LES used a filter function. This filter function define which eddies are large by introducing a length scale, usually denoted as Δ in LES, the characteristic filter width of the simulation. All eddies larger than Δ are resolved directly, while those smaller than Δ are approximated.

By imposing the filter function in the continuity and the Navier-Stokes equations, one obtains the filtered equations governing the fluid flow in LES

$$\frac{\partial \bar{u}_i}{\partial x} = 0 \quad \text{Eq. 2.5}$$

$$\frac{\partial \bar{u}_i}{\partial t} + \frac{\partial \bar{u}_i \bar{u}_j}{\partial x_j} = -\frac{1}{\rho} \left(\frac{\partial \bar{p}}{\partial x_i} \right) + \frac{\mu}{\rho} \left(\frac{\partial^2 \bar{u}_i}{\partial x_i \partial x_j} \right) \quad \text{Eq. 2.6}$$

where ρ , p and μ represent the air density, pressure and dynamic viscosity of the flow, respectively.

The unknown stress term $\overline{u_i u_j}$ needs to be approximated to solve the filtered Navier-Stokes Equations.

$$\overline{u_i u_j} = \overline{(\bar{u}_j + u'_j)(\bar{u}_i + u'_i)} = \overline{\bar{u}_i \bar{u}_j} + \overline{u'_i \bar{u}_j} + \overline{\bar{u}_i u'_j} + \overline{u'_i u'_j} \quad \text{Eq. 2.7}$$

This above equation can be described as below,

$$\tau_{ij} = (\overline{u_i u_j} - \overline{\bar{u}_i \bar{u}_j}) + (\overline{u'_i \bar{u}_j} + \overline{\bar{u}_i u'_j}) + \overline{u'_i u'_j} \quad \text{Eq. 2.8}$$

The term τ_{ij} is known as the subgrid scale (SGS) Reynolds Stress.

To approximate the SGS Reynolds stress τ_{ij} , a SGS model can be employed. The most commonly used SGS models in LES is the Smagorinsky model. This model assumed that the SGS Reynolds stress τ_{ij} is proportional to the modulus of the strain rate tensor of the resolve eddies,

$$\tau_{ij} - \frac{1}{3} \tau_{kk} = -2\nu_{SGS} \bar{S}_{ij} = \nu_{SGS} \left| \frac{\partial \bar{u}_i}{\partial x_j} + \frac{\partial \bar{u}_j}{\partial x_i} \right| \quad \text{Eq. 2.9}$$

Where ν_{SGS} is the SGS eddy viscosity and \bar{S} is the train rate tensor,

$$|\bar{S}| = [2.\overline{S_{ij}S_{ij}}]^{1/2} \quad \text{Eq. 2.10}$$

2.2.2.2. Reynolds Averaged Navier-Stokes (RANS)

The first approach for the approximate treatment of turbulent flows was presented by Reynolds in 1895. The methodology is based on the decomposition of the flow variables into a mean and a fluctuating part. The governing equations are then solved for the mean values, which are the most interesting for engineering applications. Thus, considering first incompressible flows, the velocity components in the governing equations are substituted by:

$$U = \bar{U} + u' \quad \text{Eq. 2.11}$$

where the mean value is denoted by an overbar and the turbulent fluctuations by a prime. The mean values are obtained by an averaging procedure. The time averaging velocity component is defined as,

$$\bar{U} = \frac{1}{T} \int_0^T U dt \quad \text{Eq. 2.12}$$

where T is the interval time of the simulation, usually chosen to be large compared to the typical timescale of turbulent fluctuations.

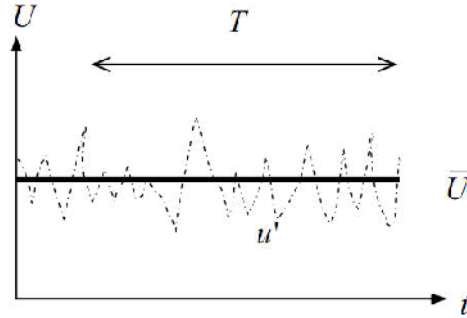


Figure 2.2. Time averaging of turbulence using RANS models [35]

We replace Eq. 2.11 into the Navier-Stokes equations for time averaging, the time averaged Navier-Stokes equations will be obtained as,

$$\frac{\partial \bar{u}_i}{\partial t} + \bar{u}_j \frac{\partial \bar{u}_i}{\partial x_j} = -\frac{1}{\rho} \left(\frac{\partial \bar{p}}{\partial x_i} \right) + \frac{\partial}{\partial x_j} \left(\nu \frac{\partial \bar{u}_i}{\partial x_j} - \overline{u_i u_j} \right) \quad \text{Eq. 2.13}$$

where ρ , p and ν represent the density, pressure and kinetic viscosity of the flow respectively.

In the averaged Navier-Stokes equations, the unknown term $\overline{u_i u_j}$, which are the correlation to the fluctuating velocity components, is known as the Reynolds Stress term. The existence of the Reynolds stress means that there is no longer a closed set of equations, and turbulence model assumptions needed to estimate the unknowns to solve this closure problem.

RANS models have been developed based on the concept that a velocity scale and a length scale is sufficient to describe the effect of turbulence in a flow. These models can be divided into first and second order closures, respectively.

The most complex, but also the most flexible, are second order closure models. The Reynolds stress transport model (RST) solves modeled transport equations for the Reynolds stress tensor. The partial differential equations for the six stress components have to be closed by one additional relation. Normally, an equation for the turbulent dissipation rate is employed. RSM gives more accurate solutions since it simulates the anisotropic nature of turbulence more realistically. However, this model is computationally more demanding among the RANS models.

Closely related to the RST are the ARS models. The ARS models employ only two transport equations, mostly for the turbulent kinetic energy and the dissipation rate. The components of the Reynolds stress tensor are related to the transport quantities by non-linear algebraic equations. The ARS is capable of predicting rotational turbulent flows with accuracy similar to RST models.

The first order closures can be classified into zero, one and two equation models, corresponding to the number of transport equations they utilize. Within the zero equation, the turbulent eddy viscosity is calculated from empirical relations. It limits the prediction of separated flows. To overcome the shortcomings of the zero equation models, the one equation models the convection and the diffusion of turbulence by transport equations. The most widely used one equation turbulence model is S-A model, which is based on an eddy-viscosity like variable. The model is numerically very stable and easy to implement on structured as well as unstructured grids.

On the other hand, the two equation models, which require less computer power compared to RST and ARS, are most often used in engineering applications. These models relate to the effect of the transport of turbulence quantities by considering the energy transfer in the flow. Apart from the transport of energy, the calculation of an empirical length scale from a second transport equation is also involved. Thus, they offer a reasonable compromise between computational effort and accuracy. In two equation models, the k- and k- models are the two most widely used models in CFD.

a. Mixing length models

Mixing length models attempt to describe the stresses by means of simple algebraic formulae for the turbulent viscosity μ_t as a function of position. To do that, we assume the kinetic

turbulent viscosity ν_t , which has dimensions m^2/s , can be expressed as a product of a turbulent velocity scale \mathcal{G} (m/s) and a turbulent length scale ℓ (m). If one velocity scale and one length scale suffice to describe the effects of turbulence, dimensional analysis yields,

$$\nu_t = C\ell\mathcal{G} \quad \text{Eq. 2.14}$$

where C is a dimensionless constant of proportionality

Of course the dynamic turbulent viscosity is given by:

$$\mu_t = \rho C\ell\mathcal{G} \quad \text{Eq. 2.15}$$

We can attempt to link the characteristic velocity scale of eddies with the mean flow properties. This has been found to work well in simple two-dimensional turbulent flows where the only significant Reynolds stress is $\tau_{xy} = \tau_{yx} = -\overline{u'v'}$ and the only significant mean velocity gradient is U/y . For such flows it is at least dimensionally correct to state that, if the eddy length scale is ℓ ,

$$\mathcal{G} = c\ell \left| \frac{\partial U}{\partial y} \right| \quad \text{Eq. 2.16}$$

where c is a dimensionless constant. The absolute value is taken to ensure that the velocity scale is always a positive quantity irrespective of the sign of the velocity gradient.

Combining (Eq. 2.14) and (Eq. 2.16) and absorbing the two constants C and c into a new length scale ℓ_m we obtain

$$\nu_t = \ell_m^2 \left| \frac{\partial U}{\partial y} \right| \quad \text{Eq. 2.17}$$

With U/y is the only significant mean velocity gradient, the turbulent Reynolds stress is described by:

$$\tau_{xy} = \tau_{yx} = -\overline{\rho u'v'} = \rho \ell_m^2 \left| \frac{\partial U}{\partial y} \right| \frac{\partial U}{\partial y} \quad \text{Eq. 2.18}$$

The mixing length has been found to be very useful in simple two-dimensional flows with slow changes in the flow direction. In these cases the production of turbulence is in balance with its dissipation throughout the flow, and turbulence properties develop in proportion with a mean flow length scale L . This means that in such flows the mixing length ℓ_m is proportional to L and can be described as a function of position by means of a simple algebraic formula.

The most advantage of these models is easy to implement and cheap in terms of computing resources. Besides, they can predict well for thin shear layers: jets, mixing layers, wakes and

boundary layers. However, there are some difficulties if we use is that they are completely incapable of describing flows with separation and recirculation and only calculates mean flow properties as well as turbulent shear stress.

b. The Spalart-Allmaras one-equation model

These models represent the easiest way to approximate the Reynolds stresses in the Reynolds averaged Navier-Stokes equations. They employ transport equation for an eddy-viscosity variable $\bar{\nu}$.

$$\frac{D\bar{\nu}}{Dt} = G_{\nu} + \frac{1}{\sigma_{\nu}} \left[\frac{\partial}{\partial x_j} \left\{ (\mu + \rho\bar{\nu}) \frac{\partial \bar{\nu}}{\partial x_j} \right\} + C_{2b\rho} \left(\frac{\partial \bar{\nu}}{\partial x_j} \right)^2 \right] - Y_{\nu} + S_{\nu} \quad \text{Eq. 2.19}$$

In which, eddy-viscosity is obtained from:

$$\mu_t = \rho \cdot \bar{\nu} \cdot f_{\nu1} \text{ with } f_{\nu1} \equiv \frac{(\bar{\nu}/\nu)^3}{(\bar{\nu}/\nu)^3 + C_{\nu1}^3} \quad \text{Eq. 2.20}$$

It was calibrated using results for 2-D mixing layers, wakes and flat-plate boundary layers. The Spalart-Allmaras (S-A hereafter) model also allows for reasonably accurate predictions of turbulent flows with adverse pressure gradients. Furthermore, it is capable of smooth transition from laminar to turbulent flow at user specified locations. The S-A model has several favorable numerical features. It is “local” which means that the equation at one point does not depend on the solution at other points. Therefore, it can be readily implemented on structured multi-block or on unstructured grids. It is also robust, converges fast to steady-state and requires only moderate grid resolution in the near-wall region.

c. The $k-\varepsilon$ models

The $k-\varepsilon$ turbulence models are the most widely employed two-equation eddy-viscosity model. It is based on the solution of equations for the turbulent kinetic energy k and the turbulent dissipation rate ε . The turbulent dissipation rate ε is written as,

$$\varepsilon = \frac{k^{3/2}}{L} \quad \text{Eq. 2.21}$$

where k is the kinetic energy of the flow and L is the length scale involved. This is then related to the turbulent viscosity μ_t based on the Prandtl mixing length model,

$$\mu_t = \rho \cdot C_{\mu} \frac{k^2}{\varepsilon} \quad \text{Eq. 2.22}$$

Where C_{μ} is an empirical constant and ρ is the density of the flow. Substituting Eq 2.22 into the equations governing fluid flow, the k equation of the k- model is written as,

$$\frac{\partial(\rho k)}{\partial t} + \underbrace{U_i \frac{\partial(\rho U_j k)}{\partial x_j}}_{\text{convection term}} = \underbrace{\frac{\partial}{\partial x_j} \left(\frac{\mu_t}{\sigma_\varepsilon} \frac{\partial k}{\partial x_j} \right)}_{\text{Diffusion term}} + \underbrace{\mu_t \cdot \frac{\partial U_i}{\partial x_j} \left(\frac{\partial U_i}{\partial x_j} + \frac{\partial U_j}{\partial x_i} \right)}_{\text{Production term}} \frac{\partial U_i}{\partial x_j} - \underbrace{\rho \varepsilon}_{\text{Destruction term}} \quad \text{Eq. 2.23}$$

and the equation,

$$\frac{\partial(\rho \varepsilon)}{\partial t} + \frac{\partial(\rho U_j \varepsilon)}{\partial x_j} = \frac{\partial}{\partial x_j} \left(\frac{\mu_t}{\sigma_\varepsilon} \frac{\partial \varepsilon}{\partial x_j} \right) + C_{\varepsilon 1} \frac{\varepsilon}{k} \mu_t \cdot \frac{\partial U_i}{\partial x_j} \left(\frac{\partial U_i}{\partial x_j} + \frac{\partial U_j}{\partial x_i} \right) - \rho C_{\varepsilon 2} \frac{\varepsilon^2}{k} \quad \text{Eq. 2.24}$$

Where $C_\mu = 0.09$; $C_{\varepsilon 1} = 1.44$; $C_{\varepsilon 2} = 1.44$; $\sigma_k = 1.0$ and $\sigma_\varepsilon = 1.3$ based on extensive examination of a wide range of turbulent flows.

The rate of change of kinetic energy is involved to the convection and diffusion of the mean motion of the flow. The production term, which is responsible for the transfer of energy from the mean flow to the turbulence, is counterbalanced by the interaction of the Reynolds stresses and mean velocity gradient. The destruction term deals with the dissipation of energy into heat due to viscous nature of the flow.

These are some following advantages which the k - models become the most popular method among RANS models:

- Simplest turbulence model for which only initial and boundary conditions need to be supplied.
- excellent performance for many industrially relevant flows,
- Well established, the most widely validated turbulence model,
- Lower computational overhead,
- Robust formulation

Nevertheless, the models also have some restrictions:

- Over prediction of turbulence near stagnation point
- Length scale is too large in adverse pressure gradient flow
- Fails to resolve flows with large strains such as swirling flows and curved boundary layers flow.
- more expensive to implement than the mixing length model

d. The k - ω models

The basic idea of the k - ω model was originated by Kolmogorov (1942) and was developed by Wilcox (1988) as an alternative to cope with the deficiencies of the k - ε model at the walls. The k - ω model is very similar in structure to the k - ε model but the variable ε is replaced by

the dissipation rate per unit kinetic energy, ω . The transport equations for k and ω [Wilcox, 1988] may be written as below:

$$\frac{\partial(\rho k)}{\partial t} + U_i \frac{\partial(\rho U_j k)}{\partial x_j} = \frac{\partial}{\partial x_j} \left(\frac{\mu_t}{\sigma_\varepsilon} \frac{\partial k}{\partial x_j} \right) + \mu_t \cdot \frac{\partial U_i}{\partial x_j} \left(\frac{\partial U_i}{\partial x_j} + \frac{\partial U_j}{\partial x_i} \right) \frac{\partial U_i}{\partial x_j} - \rho k \varepsilon \quad \text{Eq. 2.25}$$

$$\frac{\partial(\rho \omega)}{\partial t} + \frac{\partial(\rho U_j \omega)}{\partial x_j} = \frac{\partial}{\partial x_j} \left(\frac{\mu_t}{\sigma_\omega} \frac{\partial \omega}{\partial x_j} \right) + \alpha \frac{\omega}{k} \mu_t \cdot \frac{\partial U_i}{\partial x_j} \left(\frac{\partial U_i}{\partial x_j} + \frac{\partial U_j}{\partial x_i} \right) - \rho \beta \omega^2 \quad \text{Eq. 2.26}$$

Where the turbulence k is associated with vorticity, ω being proportional to k^2/ℓ ,

$$\omega = c \cdot \frac{k^2}{\ell} \quad \text{Eq. 2.27}$$

where c is a constant. Thus, the eddy viscosity may be written as:

$$\mu_t = \rho k / \omega \quad \text{Eq. 2.28}$$

The replacement with the variable ω allows solving the flow near wall. Near to the wall, the boundary layer is affected by viscous nature of the flow. Thus, a very refined mesh is necessary to appropriately resolve the flow. The k - ω model avoids using fine mesh near wall by employing empirical formula to predict the flow in order to save computational power.

Despite the k - ω model saves a vast amount of computer power for near wall treatment, it is not sufficient to represent complex flow accurately. The flow near wall is resolved directly through the integration of the ω equation in the k - ω formulation. The most advantage of the k - ω model is that the ω equation is more robust and easier to integrate compared to the ε equation without the need of additional damping functions.

e. Reynolds stress equation models

The k - ε turbulence model is based on the isotropic eddy-viscosity concept for closure of the Reynolds stresses. In some flow situations, such as when body forces or complex strain fields are present, this assumption is too simple. To overcome this restriction, RST models allow not only for both the transport and different development of the individual Reynolds stresses, but also have the advantage that terms accounting for anisotropic effects are introduced automatically into the stress transport equations. These non-isotropic characteristics of the turbulence play a very important role in flows with significant buoyancy, streamline curvature, swirl or strong recirculation.

Models employing transport equations for the turbulent stresses and fluxes are often called second-moment closures, and several research groups, most notably by Launder and his associates, have proposed such models (see for example Launder et al (1975)). The most complex models in common use today are Reynolds stress models which based on dynamic

equations for the Reynolds stress tensor $\tau_{ij} = \overline{\rho u_i' u_j'}$ itself. These equations can be derived from the Navier-Stokes equations.

A full RST model closure consists, in general, of 6 transport equations for the Reynolds stresses, 3 transport equations for the turbulent fluxes of each scalar property (for example energy) and one transport equation for the dissipation rate of turbulence energy. The solution of all these complex equations together with those of the mean flow is not a trivial task, and it is also computation- ally expensive.

In addition there is a considerable numerical disadvantage arising from the use of a RST model in that the stabilizing effects of an eddy- viscosity field are absent in the mean-flow equations. Thus, although RST models can provide a more realistic and rigorous approach for complex engineering flows, they may be too expensive in terms of storage and execution time for three-dimensional flows.

f. Algebraic stress equation models

The purpose of algebraic Reynolds stress models is to avoid the solution of differential equations, and to obtain the Reynolds stress components directly from algebraic relationships. If mean strain rates are ignored in the Reynolds stress transport equations, it follows from the strain-dependent generalization of nonlinear constitutive relation that the turbulent stress tensor may be written as Rodi (1976); Gatski and Speziale (1992).

$$\tau_{ij}^* = \frac{k}{\varepsilon} (D_{ij} + B_{ij}) \quad \text{Eq. 2.29}$$

With

$$\begin{aligned} D_{ij} &= c_1 \frac{\varepsilon}{k} \left(\tau_{ij}^* + \frac{2}{3} \rho k \delta_{ij} \right) \\ B_{ij} &= -\frac{2}{3} \rho \varepsilon \delta_{ij} \end{aligned} \quad \text{Eq. 2.30}$$

Thus, if the mean strain rate vanishes, we have,

$$\tau_{ij}^* = -\frac{2}{3} k \rho \delta_{ij} \quad \text{Eq. 2.31}$$

This suggests that the algebraic stress model is confined to isotropic turbulence. Thus, this model fails to properly account for sudden changes in the mean strain rate. However, it also have some advantages as below:

- cheap method to account for Reynolds stress anisotropy
- potentially combines the generality of approach of the RSM (good modeling of buoyancy and rotation effects possible) with the economy of the k - ε model

- successfully applied to isothermal and buoyant thin shear layers
- if convection and diffusion terms are negligible the ASM performs as well as the RSM

The restrictions of this model reduce its application.

- only slightly more expensive than the $k-\varepsilon$ model (two PDEs and a system of algebraic equations)
- not as widely validated as the mixing length and $k-\varepsilon$ models
- same disadvantages as RSM apply
- Model is severely restricted in flows where the transport assumptions for convective and diffusive effects do not apply - validation is necessary to define the performance limits.

2.2.3. Initial and boundary conditions

Regardless of the numerical methodology chosen to solve the governing equations (2.4), one has to specify suitable initial and boundary conditions. The boundary conditions may describe conditions along the boundary dealing with motion, external stresses, rate of mass, and momentum flux, boundary values of field variables, as well as relations among them. When the solution involves the time evolution of flow fields, in addition to boundary conditions, initial conditions are also required.

2.2.3.1. Free and no slip

a. No-slip condition: No fluid penetrates the boundary and the fluid is at rest there; i.e.,

$$\varphi_n(x, y) = 0, \varphi_t(x, y) = 0 \quad \text{Eq. 2.32}$$

b. Free-slip condition: No fluid penetrates the boundary. Contrary to the no-slip condition, however, there are no frictional losses at the boundary; i.e.,

$$\varphi_n(x, y) = 0, \partial\varphi_t(x, y)/\partial n = 0 \quad \text{Eq. 2.33}$$

The free-slip condition is often imposed along a line or plane of symmetry in the problem, thereby reducing the size of the domain where the flow needs to be computed by a half.

2.2.3.2. Neumann and Dirichlet conditions

a. Dirichlet boundary condition: the value of a dependent variable, u , is imposed along r_s ,

$$u(r_s, t) = f(r_s, t) \quad \text{Eq. 2.34}$$

where f is a known function. Typical Dirichlet boundary conditions are the no-slip boundary condition for the velocity (i.e., $u_s=0$) and the specification of inlet and/or outlet values for the velocity.

b. Neumann boundary condition: the normal derivative of the dependent variable is specified.

$$\frac{\partial u}{\partial n} = G(r_s, t) \quad \text{Eq. 2.35}$$

where G is a known function. Examples of Neumann boundary conditions are symmetry conditions and free-surface as well as interface stress conditions.

c. Robin boundary condition: it is a combination of the Dirichlet and the Neumann types. The dependent variable and its normal derivative are related by the general expression

$$au + b \cdot \frac{\partial u}{\partial n} = c \quad \text{Eq. 2.36}$$

where a , b , c are known functions. The slip boundary condition, the free-surface and interface stress conditions are typical Robin conditions.

2.3. Discretization

After selecting the mathematical model, one has to choose a suitable discretization method, e.g. a method of approximating the differential equations by a system of algebraic equations for the variables at some set of discrete locations in space and time. The main purpose of discretization is to simplify the fluid flow problems into discrete numerical data. Thus, they can be solved completely by the computer. Generally, there are two major discretizations in solving fluid flow:

- Spatial discretization
- Temporal discretization

2.3.1. Spatial discretization

As mentioned in 2.1.1, the mathematical model consists of partial differential equations. Solving the set of partial differential equation is usually very difficult and time-consuming. Thus, equation discretization is employed to translate the governing equations into a system of algebraic equations that can be solved by computer. There are many approaches of equation discretization, but the most important of which are the finite difference method (FDM), the finite element method (FEM) or the finite volume method (FVM). Other methods, like spectral schemes, boundary element methods are used in CFD but their use is limited to special classes of problems. All of FEM, FVM, and FDM rely on some kind of grid in order to discretize the governing equations. There exist three main types of grids commonly used in computational modeling are:

- Structured grid;
- Unstructured grid;
- Hybrid grid.

a. Structured mesh

The distinguishing feature of structured grids is that the grid points in the physical space are mapped in a unique way onto a continuous set of three integers i, j, k (one for each coordinate direction). Neighboring grid points can be connected to form cubes in the computational and hexahedra (quadrilaterals in 2D) in the physical space. Structured grid generation systems discretize the boundary surfaces of the flow domain using quadrilaterals -termed the surface grid - and fill the interior with hexahedra in figure 2.3.

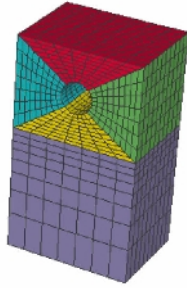


Figure 2.3: An example of structured mesh

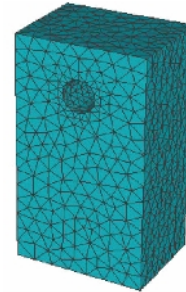


Figure 2.4: An example of unstructured mesh

Although the element topology is fixed, the grid can be shaped to be body fitted through stretching and twisting of the block. However, a structured grid performs badly when the geometry of problem domain is complex, which is quite common in engineering applications. In this case, the unstructured grid will be employed.

b. Unstructured mesh

In an unstructured mesh, the nodes can be placed accordingly within the computational domain depending on the shape of the body, such that different kinds of complex computational boundaries and geometries can be simulated. Since the arrangement of nodes has no particular order, neighboring points cannot be directly identified. A numerical approach has to be imposed to describe how each node is connected to the control volumes. An unstructured mesh works well around complex geometries but this requires more elements for refinement compared to a structured mesh on the same geometry, leading to higher computing cost.

In the case of unstructured grids, nodes and grid cells are quasi randomly ordered, i.e., neighboring cells or grid points can not be directly identified by their indices. Unstructured grids are typically composed of triangles in 2D and of tetrahedral in 3D shown in Figure 2.4. This results in tremendous geometric flexibility of unstructured grids, since the grid does not need to conform to any predetermined topology. Furthermore, adaptation of the grid to the physical solution - grid refinement or coarsening - is much easier to accomplish on unstructured than on structured grids.

An unstructured mesh works well around complex geometries but this requires more elements for refinement compared to a structured mesh on the same geometry, leading to higher computing cost. Another drawback of this grid is the lack of user control when laying out the mesh. To compensate between computing cost and flexibility, the hybrid mesh is introduced.

c. Hybrid mesh

Hybrid mesh is designed to take advantage of the positive aspects of the both structured and unstructured grid. The ability to control the shape and distribution of the grid locally is a powerful tool which can yield excellent meshes. Hybrid grids utilize some form of structured grid in local regions while using unstructured grid in the bulk of the domain. This mesh usually uses the most appropriate cell type in any combination, i.e. triangles and quadrilaterals in 2D, tetrahedral, prisms and pyramids in 3D (see in Figure 2.5). It can also be non-conformal. This meant that grids lines don't need to match at block boundaries.

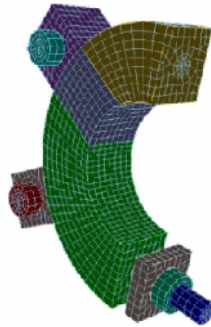


Figure 2.5: An example of hybrid mesh

The disadvantage of hybrid methods is that they can be difficult to use and require user expertise in laying out the various structured grid locations and properties to get the best results. Hybrid methods are typically less robust than unstructured grid. Furthermore, the time required for grid generation is usually measured in hours or days.

2.3.1.1. Finite difference method

One of the methods used to discretize the equations of flow for computational solution is the finite difference method. It was first used by Euler, probably in 1768, which obtained solutions to differential equations by hand calculation. At each nodal point of the grid used to describe the fluid-flow domain, the Taylor series expansions are used to generate finite-difference approximations to the partial derivatives of the governing equations. These derivatives, replaced by finite-difference approximations, yield an algebraic equation for the flow solution at each grid point.

The finite difference methodology is popular and famous because of its simplicity. Another advantage is the possibility to easily obtain high-order approximations, and hence to achieve

high-order accuracy of the spatial discretization. On the other hand, because the method requires a structured grid, the range of application is clearly restricted. Furthermore, the finite difference method cannot be directly applied in body-fitted (curvilinear) coordinates, but the governing equations have to be first transformed into a Cartesian coordinate system.

2.3.1.2. Finite element method

The finite element method was originally employed for structural analysis only. It was first introduced by Turner et al. (1956). Unlike FDM, FEM used unstructured mesh. The domain is broken into a set of discrete volumes or finite elements that are generally unstructured; in 2D, they are usually triangles or quadrilaterals, while in 3D tetrahedral or hexahedra are most often used. Within each element, a certain number of nodes are defined where numerical values of the unknowns will be computed. The distinguishing feature of FE methods is that the equations are multiplied by a weight function before they are integrated over the entire domain.

The most important advantage of finite element methods is its integral formulation and the use of unstructured grids, which are both preferable for flows in or around complex geometries. The method is also particularly suitable for the treatment of non-Newtonian fluids.

In addition the advantage, it also exist the drawbacks. The principal drawback is that the matrices of the linearized equations are not as well structured as those for regular grids making it more difficult to find efficient solution methods.

2.3.1.3. Finite volume method

The finite-volume method discretizes the integral form of the conservation equations directly in the physical space. It was initially introduced by researchers such as McDonald (1971) and MacCormack and Paullay (1972) for the solution of two-dimensional time-dependent Euler equations, and was later extended to three-dimensional flows by Rizzi and Inouye (1973). The computational domain is subdivided into a finite number of control volumes. The governing equations of fluid flow problem are integrated and solved iteratively based on the conservation laws on each control volume. The discretization process leads to a set of algebraic equations that resolve the variables at a specified finite number of points within the control volumes, usually the centroid of each of the control volumes. By using an integration method, the flow around the domain can be completely modeled and computed.

The main advantage of the finite volume method is that the spatial discretization is carried out directly in the physical space. Thus, there are no problems with any transformation between coordinate systems, like in the case of FDM. Compared to the finite differences, one further advantage of the finite volume method is that it is very flexible - it can be rather easily implemented on structured as well as on unstructured grids. Therefore, FVM is the most popular and common in recent CFD applications.

2.3.2. Temporal discretization

The last discretization is the temporal discretization. The main idea is that it will divide the time in the continuous flow into discrete time steps. Hence, we add an additional time variable t in the governing equations to compare to the steady state analysis. This results in a system of partial differential equations in time that consists of unknowns at a given time as a function of the variables of the previous time step. Therefore, unsteady simulation often requires longer computational time than a steady case. There are two types of temporal discretization. That is explicit and implicit method. Both explicit and implicit method can be used for unsteady time-dependent calculation.

2.3.2.1. Explicit method

In an explicit method, each difference equation contains only one unknown and thus can be solved explicitly for this unknown in a straight forward. That means that a forward difference in time is taken when calculating the time t^{n+1} by using the previous time step value (Figure 2.6) where n dedicates state at time t and $n + 1$ at time $t + \Delta t$.

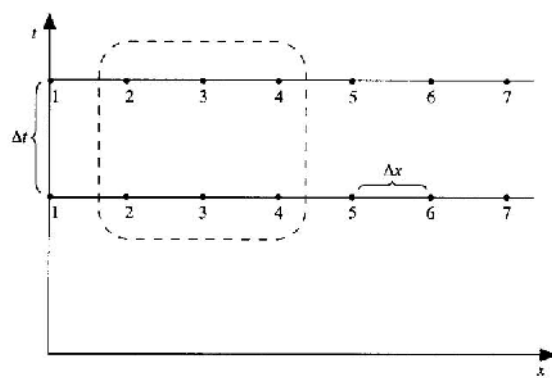
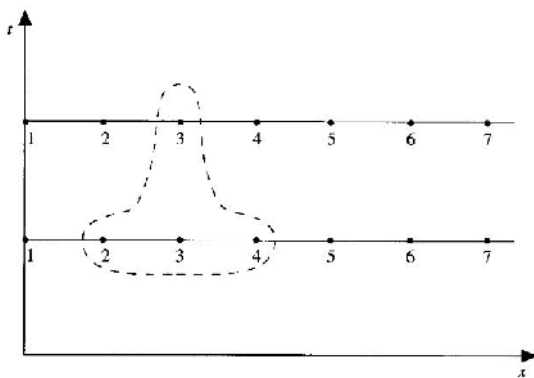


Figure 2.6. An explicit finite difference module [6] Figure 2.7. An implicit finite difference module [6]

The main advantage of explicit method is relatively simple to set up and program. However, it requires a smaller time step Δt and a smaller grid step Δx to maintain stability. This can leads to long computer running times to make calculations over a given interval of t .

2.3.2.2. *Implicit method*

An implicit method is one where the unknowns must be obtained by means of a simultaneous solution of the difference equations applied at all the grid points arranged at a given time level. That means this method calculates values of time step t^{n+1} at the same time level in a simulation at different grid points based on a backward difference (figure 2.7). This leads to a larger system of linear equations in which unknowns at time step t^{n+1} must be solved simultaneously.

The main advantage of implicit scheme compared to explicit one is that much larger values of Δt can be used, while maintaining the stability of the time integration process. Hence, the computation uses considerable fewer time steps to make calculations over a given interval of t . This results in less computer time. Nevertheless, this can result in the large truncation error and may not be as accurate as an explicit approach. Another drawback is more complicated to set up and program.

2.3.3. *Quality of discretization*

There is a certain spatial discretization error because of the approximation of the fluxes across the boundaries of the control volume. This means that the discretized equations differ from the exact equations by the discretization error, which results from the numerical scheme applied. Therefore, some following properties need to estimate how fast the solution of the discretized equations converges to the exact solution of the governing equations with increasingly finer grid. These properties interact as in figure 2.8.

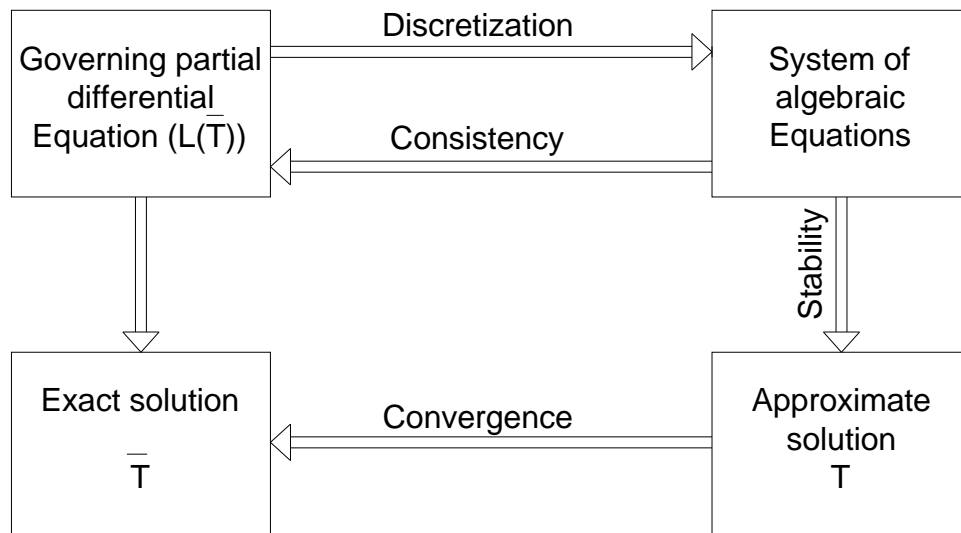


Figure 2.8. Relationship between qualities of discretization

2.3.3.1. Consistency

A discretization scheme is called consistent, if the discretized equations converge to the given differential equations for both the time step and grid size tending to zero. A consistent scheme gives us the security that we really solve the governing equations and nothing else.

The consistency of a numerical scheme can be checked by expanding the function values into Taylor series. The developments are then inserted back into the discretized equations. If we subtract the differential equations, we obtain terms which represent the numerical error - the so-called truncation error. For a consistent scheme, the truncation error should go to zero with decreasing time step and grid size.

2.3.3.2. Stability

A numerical solution method is said to be stable if it does not magnify the errors that appear in the course of numerical solution process. For temporal problems, stability guarantees that the method produces a bounded solution whenever the solution of the exact equation is bounded. Stability can be difficult to investigate, especially when boundary conditions and non-linearities are present.

2.3.3.3. Convergence

A numerical method is said to be convergent if the solution of the discretized equations tends to the exact solution of the differential equation as the grid spacing tends to zero. Besides, if the method is stable and if all approximations used in the discretization process are consistent, the solution also converges to a grid-independent solution.

2.3.3.4. Accuracy

The accuracy of a discretization scheme is connected to its truncation error. If, for instance, the leading term of the truncation error is proportional to Δx , we speak of first-order accurate spatial scheme. If the leading term behaves like $(\Delta x)^2$, the scheme is second-order accurate, and so on. This leads to the condition that the numerical scheme must be at least 1st-order accurate in order to be consistent. Otherwise, the truncation error cannot be reduced by decreasing the values of Δt and Δx .

Besides, the estimation of the truncation error, varying the grid resolution is also used to obtain what is called grid converged solution. This is achieved if the solution does not change with further grid refinement. Although the grid convergence studies can be very time consuming, thus, it is always checked if the solution is grid converged.

2.4. Summary

This chapter discussed the background of CFD and the mathematical characteristics of numerical simulation which will be the basic knowledge for studying and understanding the results of simulation in the next chapters. Besides, a series of turbulence models also described with the advantages and shortcomings. However, choosing the appropriate turbulence model will be very difficult and hesitant if we only based on the theoretical comments, because it depends on the specific problem as well as other boundary conditions. The most suitable turbulence model will be selected in next chapter.

3. GRID GENERATION

Grid generation is often considered as the most important and most time-consuming part of CFD simulation. The quality of the grid plays a key role on the quality of the analysis, even the flow solved used. In addition, the solver will be more efficient and robust when using a well constructed mesh.

This chapter will described how the mesh was generated and how to impose the boundary conditions on the mesh domain by using some specialist tools. At present, there are many tools, which can be used such as GAMBIT, TGRID, GRIDGEN, etc. However, in this master thesis, GAMBIT is employed to do that because of its remarkable advantages such as: user-friendly, easy to implement and popularity.

3.1. Overview of grid

As aforementioned in Section 2.2.1.3, there are three fundamental classes of grid popular in the numerical solution of boundary value problems in multidimensional regions: structured, unstructured and hybrid. Each type of mesh has both advantages and disadvantages. The application of these types depends on the specific problem as well as computational requirements. In this project, the geometry is not complex, thus, the structured grid is applied to discretize the computational domain because it can easily allow for controlling and improving the grid quality. Moreover, it will help to easily control when laying out the mesh, especially, useful for the computation of turbulence model.

3.1.1. Grid topology

Before we start to generate any grid, its topology must be considered. This means how many grid blocks are necessary and how the blocks should be ordered with respect to each other must be decided. For each grid block, the boundaries in the computational domain will be assigned to particular boundaries in the physical space. The appearance of the grid in the physical space will depend strongly on this assignment. In practice, three standard single block grid topologies are established. These are the C-, H-, and O-grid topology because in a plane view the grid lines resemble the corresponding capital letter. In the case of the C-topology the hydrodynamic body is enclosed by one family of grid lines ($\eta=\text{const.}$), which also form the wake region. The other family of grid lines ($\xi=\text{const.}$) emanates in normal direction from the body and the wake. The H-topology is quite often employed in turbomachinery for grid generation in the bladed flow-path. On contrary to the C-grid, one family of grid lines ($\eta=\text{const.}$) closely follows the streamlines. Related to O-topology, one family of grid lines ($\eta=\text{const.}$) forms closed curves around the hydrodynamic body. The second family

of grid lines ($\xi=\text{const.}$) is spanned in radial direction between the body and the outer boundary.

To be suitable for the computational domain of this project, the combination of two H- and O-grid topologies is employed. The O-grid topology is used inside the inner circle around the cylinder. A remarkable advantage of the O-topology is the good grid quality around the circular body. The main purpose is to be fit with the change of the shape of cylinder and remove the highly skewed cells for the circular cylinder. Then, the H-grid topology can be applied for surrounding domain. The grid topology of the computational domain is described in Figure 3.1.

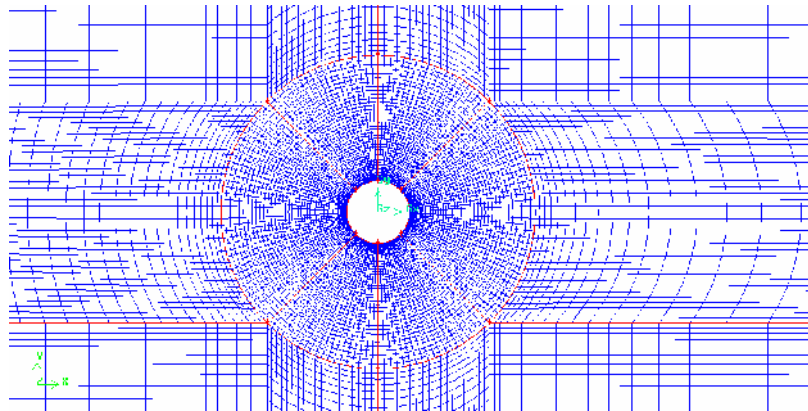


Figure 3.1. Grid topology around the cylinder

3.1.2. *Input parameter of grid generation*

Successful computations of turbulent flows require some consideration during the mesh generation. Since turbulence plays a dominant role in the transport of mean momentum and other parameters, It needs to determine that turbulence quantities in complex turbulent flows are properly resolved if high accuracy is required. Due to the strong interaction of the mean flow and turbulence, the numerical results for turbulent flows tend to be more susceptible to grid dependency than those for laminar flows. Moreover, before generating the mesh, a problem that must be considered it that how walls affect a turbulent flow. In this case, the wall is the cylinder.

Experiments and mathematical analysis have shown that the near-wall region can be subdivided into three layers. In the innermost layer, the so-called “viscous sub-layer”, the flow is almost laminar-like, and the viscosity plays a dominant role in momentum and heat transfer. Further away from the wall, in the “logarithmic layer”, turbulence dominates the mixing process. Finally, there is a region between the viscous sub-layer and the logarithmic layer called the “buffer layer”, where the effects of molecular viscosity and turbulence are of equal importance. The Figure 3.2 illustrates these subdivisions of the near-wall region.

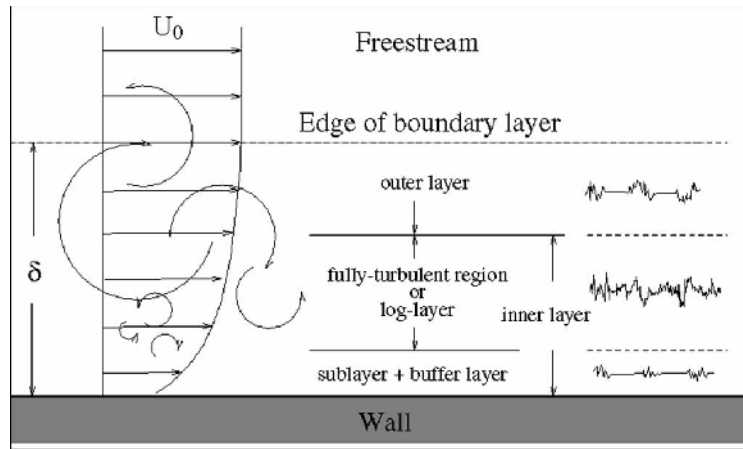


Figure 3.2. Structure of near-wall layers

There are two approaches to the near-the-wall problem. Firstly, wall function approach, where the flow near the wall is not solved, but given by a semi-empirical function called “wall function”. Secondly, near-wall model approach, where the mesh is very fine close to the wall, and the conditions are solved all the way to the wall. To solve the turbulence problem in this project, the S-A model is employed (why this model is employed will be described in next part). This model in its complete implementation is near-wall model. This means that it is designed to be used with meshes that properly resolve the viscous-affected region. Therefore, to obtain the full benefit of the S-A model, the size of wall-adjacent cells y_1 should be defined. In order to find y_1 , a dimensionless parameter y^+ which is the wall distance is used. Thus,

$$y_1 = \frac{y^+ \cdot \nu}{u_\tau} \quad \text{with} \quad u_\tau = u_\infty \sqrt{\frac{C_f}{2}} \quad \text{Eq. 3.1}$$

Where

y^+ is the wall coordinate: the distance y to the wall, made dimensionless with the friction velocity u_τ and kinematic viscosity ν ,

u_∞ is the velocity of free stream flow,

C_f is skin friction coefficient

$$\text{With plate: } C_f = 0.058 \cdot \text{Re}_l^{-0.2}$$

$$\text{With duct: } C_f = 0.079 \cdot \text{Re}_d^{-0.25}$$

According to numerical experiments, when S-A model is employed with the intention of resolving the laminar sub-layer, y^+ is well inside the viscous sub-layer ($y^+ < 5$). In this thesis, we choose $y^+ = 4$.

After computing y_1 , the number of interval count of an edge can be determined by using the regression analysis as follow:

$$S = y_1 \cdot \frac{r^n - 1}{r - 1} \quad \text{Eq. 3.2}$$

Where

S is the length of the edge,

n is the number of interval count,

r is the growth ratio, $r = \frac{\Delta y}{\Delta x}$.

$\Delta y, \Delta x$ are the grid spacing in y and x axis, respectively.

To ensure the quality of mesh, the growth ratio should be less than 1.2.

3.1.3. The process of grid generation

3.1.3.1. Definition of geometry-Step 1

The first step in any CFD analyses is the definition and creation of geometry of the computational domain for the CFD calculations. With regard to the flow around a circular cylinder, there are maybe two flow cases: a fluid flow past a cylinder between two stationary parallel plates and a fluid flow past a cylinder in a open surrounding. In this work, the second case is chosen to ensure that the calculation domain is similar to the practice.

One important aspect that should be considered in the creation of the geometry for CFD calculations is to allow the flow dynamics to be sufficiently developed across the length L of these computational domains. It meant that we require contain the occurrence of complex wake-making development that exists behind the cylinder because the flow passes over this cylinder. The cylinder is simulated with a radius (R) of 0.1m. The distances of $25R$ and $35R$ to the side boundaries and to the downstream boundaries are allowed respectively to prevent blockage ratio and free end effects on the flow.

Moreover, we should also focus on the area in which the vortex shedding appears, develop and decay. This area plays an important role on simulation as well as affects the solution of turbulent problem very much. As usual, the vortices are created in a domain around the cylinder which the perimeter is approximately five times of cylinder diameter or larger than. They will grow and decay behind this domain. Therefore, we have the geometry of calculation domain as Fig. 3.3.

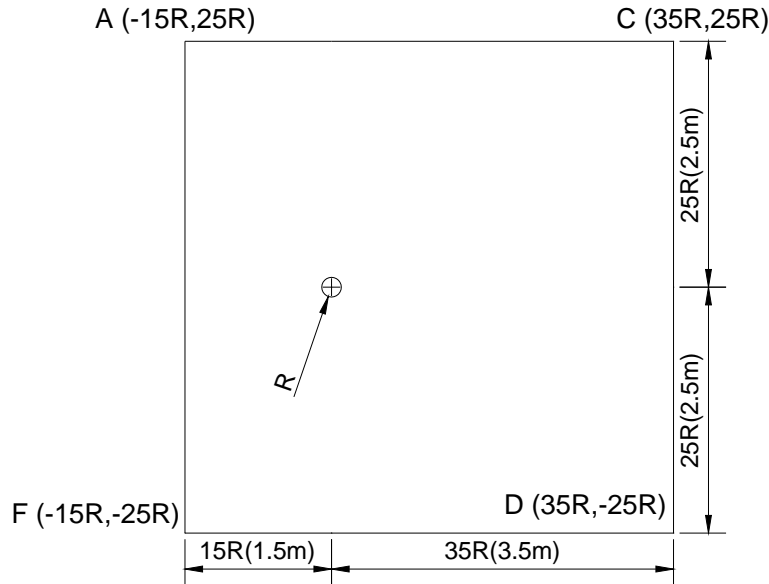


Figure 3.3. The computational domain

3.1.3.2. Mesh generation-step 2

The second step-mesh generation constitutes one of the most important steps during the pre-process stage after the domain geometry is created. CFD computation requires the subdivision of the domain into a number of smaller and non-overlapping sub-domains in order to solve the flow physics within this domain geometry; this leads to the generation of a mesh of cells (elements or control volumes) overlaying the whole domain geometry. The necessary fluid flows that are described in each of these cells are normally solved numerically so that the discrete values of the flow properties such as velocity, pressure, temperature, and the other transport parameters are also determined. The accuracy of a CFD solution depends on the number of cells. This means that the provision of a large number of cells results in the attainment of an accurate solution. However, it also requires the higher capability of computers. Herein, we must choose a number of cells based on the computer capacity and the accuracy can be accepted. Current simulation using the RANS models is based on a single Pentium Dual Core inside (1.8GHz processor) desktop PC with 1.96 GB of physical RAM. To be suitable for this computer, the number of cells that is generated is 1.52676 million elements as illustrated in Fig 3.4. Furthermore, the type of mesh or grid such as hybrid, structured or unstructured grids also affect the computational time and the precision so much. With the purpose of computing the turbulence in the boundary layer around cylinder as well as the simple shape of domain, we select the structured mesh for the domain geometry.

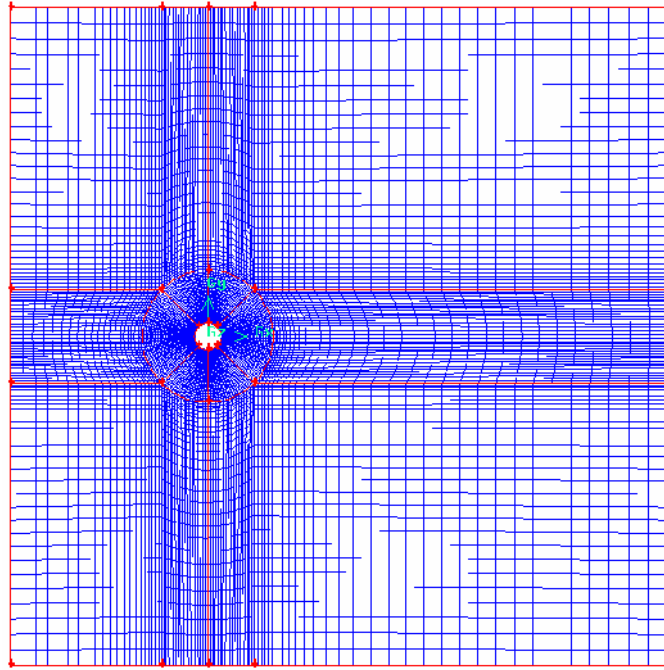


Figure 3.4. One kind of the meshes of computational domain

3.1.3.3. Imposition of boundary conditions on the computational domain-step 3

Final step of grid generation is to define appropriate conditions that model the real physical representation of the fluid flow into a solvable CFD problem. Obviously, where there exist inflow and outflow boundaries within the flow domain, suitable fluid flow boundary conditions are required to accommodate the fluid behavior entering and leaving the flow domain. In addition, appropriate boundary conditions are also required to be assigned for external stationary solid wall boundaries that bound the flow geometry and the surrounding walls of possible internal obstacles within the flow domain.

For the inflow boundary conditions, the inlet fluid velocity is required to set the fluid entering into both of these flow domains. Longitudinal uniform velocities of 0.0196m/s and 5.019m/s are introduced at the inlet correspond to the sub-critical Reynolds number of 3,900 and the super-critical Reynolds number of 1,000,000 respectively. In addition to the values of velocity, turbulence parameters are also required. These parameters will clearly be described in next section. At the outflow boundaries showing the fluid leave, only one outlet condition, typically a specified relative pressure is assigned. The use of a pressure outlet boundary condition instead of an outflow condition often results in a better rate of convergence when backflow occurs during iteration.

For the side and top boundaries are symmetry conditions. Symmetry boundaries are used to reduce the extended of computational model to a symmetric subsection of the overall physical

system. Moreover, they can be used to model zero-shear slip walls in viscous flows. The cylinder wall and the bottom wall are imposed a normal no slip boundary condition with a Neumann pressure extrapolation where velocity increases from zero at the wall surface to the free stream velocity away from the surface.

The applications of boundary conditions are illustrated in Fig.3.5.

3.2. Models of the problem

Based on the aforementioned basic steps, we perform modeling the computational domain. There are some models which can be used to simulate the problem. However, we can not be sure that which the model is the best. In order to find the best model, the computation of each model and comparison with the experimental data are very necessary and believable.

3.2.1. Turbulence parameters of simulation

With regard to the computation of each model, turbulence parameters are used to model as well as simulate the flow around a circular cylinder. Determining these initial parameters will help us save the computational time and easily approach the reasonable results of the problem. In some situations, it is appropriate to specify a uniform value of the turbulence quantity at the boundary where inflow occurs. The turbulence quantities in terms of more convenient quantities such as turbulence intensity, hydraulic diameter and turbulence length scale are specified as the following sections.

3.2.1.1. Turbulence intensity

The turbulence intensity, I , is defined as the ratio of the root-mean-square of the velocity fluctuations, u' , to the mean flow velocity, u_{avg} . For internal flows, the turbulence intensity at the inlets is totally dependent on the upstream history of the flow. If the flow upstream is under-developed and undisturbed, we can use a low turbulence intensity ($I = 1\%$). If the flow is fully developed, the turbulence may be as high as a few percent. The turbulence intensity at the core of a fully-developed duct flow can be estimated from the following derived from an empirical correlation for pipe flows:

$$I = \frac{u'}{u_{avg}} = 0.16(\text{Re}_{D_H})^{-1/8} \text{ with } \text{Re}_{D_H} = \frac{\rho \cdot u \cdot D_H}{\mu} \quad \text{Eq. 3.3}$$

Where: D_h is the hydraulic diameter.

3.2.1.2 The hydraulic diameter

The hydraulic diameter, D_h , is a commonly used term when handling flow in noncircular tubes and channels. It is defined as the following formula.

$$D_H = \frac{4A}{P} \quad \text{Eq. 3.4}$$

Where A is the cross sectional area:

With rectangular shape: $A = L.H$ with L and H is respectively the width and the height.

With circular shape: $A = \frac{\pi D^2}{4}$ with D is the diameter

P is the wetted perimeter of cross section with rectangular shape: $P = 2(L+H)$

With circular shape: $P = \pi D$

3.2.1.3. Turbulence length scale

The turbulence length scale, l , is a physical quantity related to the size of the large eddies that contain the energy in turbulent flows. In fully-developed duct flows, l is restricted by the size of the duct, since the turbulent eddies cannot be larger than the duct. An approximate relationship between l and the physical size of the duct is:

$$l = 0.07L \quad \text{Eq. 3.5}$$

where L is the relevant dimension of the duct.

With the channel of non-circular cross section, $L = D_H$,

With the pipe, $L = D$.

3.2.2. Choosing the turbulence models and the mesh

As aforementioned in Section 2.1.2, there are many turbulence models to compute the 3D flow. Choosing the model depends on the specific problem. Each model has both advantages and disadvantages. By comparison with the experimental data, the most suitable model will be used in the next study. In the current work, RANS models such as the S-A, k - models and the k - ω SST model have been first chosen to test the suitability and the applicability of the models on the flow around a circular cylinder between Reynolds number of 3,900 and 1,000,000. These Reynolds numbers in the sub-critical and super-critical regions of flow have been chosen mainly because experimental data such as the pressure distribution and drag coefficient are widely available within these Reynolds numbers for comparative study. The finite volume method with a structured hexahedral mesh is employed in the RANS models.

3.2.2.1. Computational domains

Based on the comment and advice of the previous researchers, three following domains for the simulation of the flow around a circular cylinder are built as in Figure 3.5. In all domains, the cylinder is simulated with a diameter (D) of 0.2m. The computational domain 1 and 2 is quite the same. Distances of $15R$ and $35R$ to the side boundaries and to the downstream boundaries are allowed respectively to prevent blockage ratio and end effects on the flow,

these have been chosen based on some similar cases study for initial comparison. There is only a small difference. That is the circular area of $5R$ around the cylinder where the vortices usually appear is divided into small parts in the domain 1. With the computational domain 3, this circular area is increased up to $20R$ and the distances from the upstream boundary to the cylinder also lengthened to $35R$.

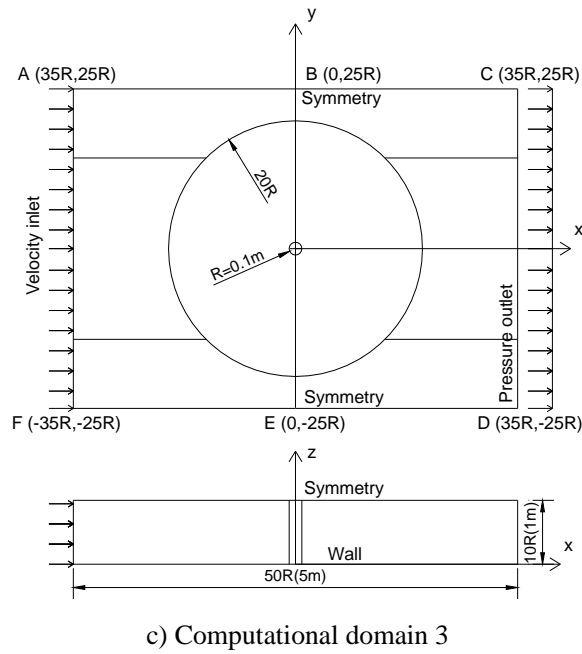
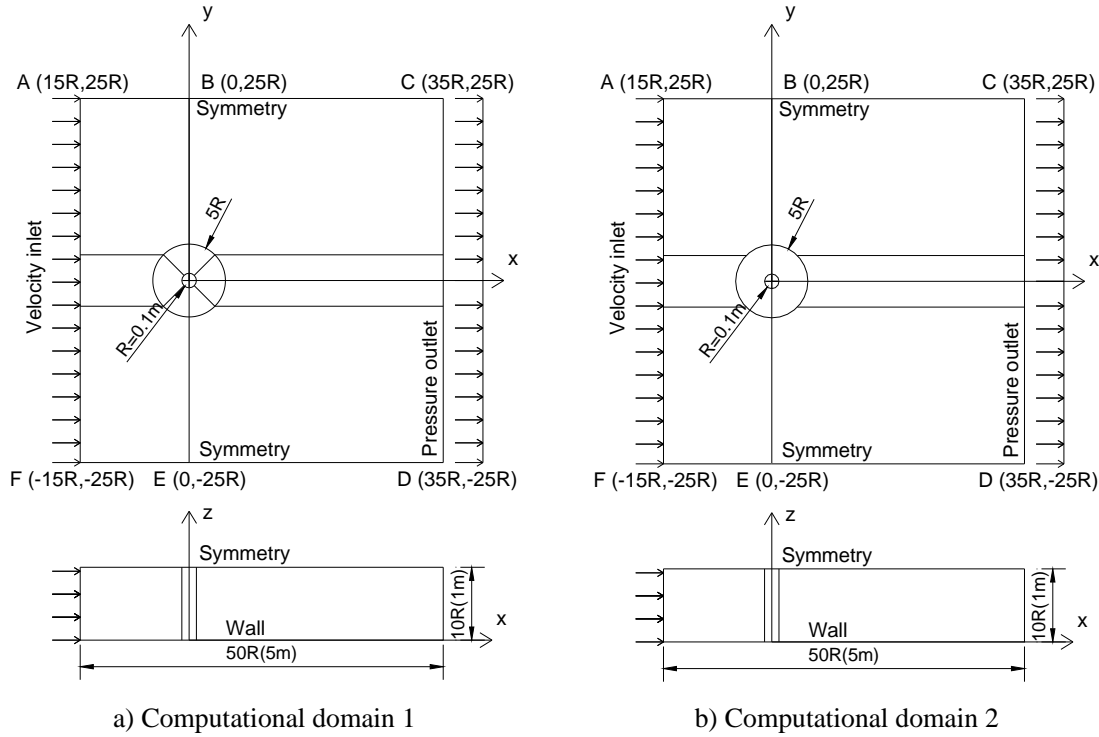


Figure 3.5. Domains to model the flow around a circular cylinder

3.2.2.2. *Boundary conditions*

Boundary conditions are imposed to the computational domains as Figure 3.5. Longitudinal uniform velocities of 0.0196m/s and 5.019m/s are introduced at the inlet correspond to the Reynolds number of 3,900 and 1 million, respectively. The outlet boundary is defined with an average static reference pressure of 0Pa. The rest of the boundaries (side and top) are symmetry, in which velocity near the wall is not retarded by frictional effects. The cylinder wall and the bottom boundary have a normal no slip boundary condition where velocity increases from zero at the wall surface to the free stream velocity away from the surface. Besides, some initial turbulent parameter such as the turbulence intensity and length scale also imposed. With the Reynolds number of 3900, the turbulence intensity is 4.3658% and the length scale is 0.1167m. On the other hand, with the Reynolds number of 1 million, the turbulence intensity is 2.1828% and the same length scale is 0.1167m.

3.2.2.3. *Modeling near wall flow*

In the Reynolds number of 3900 within sub-critical flow region, the flow near the cylinder surface is laminar and thus viscosity plays an important role. This is known as the boundary layer region of the flow. The flow has zero velocity at the surface of the wall and starts to increase radically following a ‘law of wall’ profile until free stream velocity is achieved. Therefore, a very fine mesh is needed to resolve the flow within the boundary layer. However, the finer, the mesh can be built, the higher the computer power is required to solve the flow, and the computational time will also increase.

To satisfy this requirement, the refinement of the mesh in the boundary region is determined by the dimensionless parameter y^+ . Physically, y^+ represents the normal distance of the grid points from the cylinder wall. In FLUENT software, the near wall problem can be treated by two methods. First of all, the S-A and $k-\omega$ models require the fine mesh, hence, the y^+ value needs to be smaller than 5 to maintain mesh consistency and to represent the boundary layer correctly. Second of all, the $k-\epsilon$ models and other turbulence models use empirical formulas to represent the “law of wall” region. These models employ the wall function method to model the flow near to the wall. In the wall function method, the viscosity sub-layer is represented mathematically by formulas to account for the effect of shear stress.

To find the mechanics of 3D flow within sub-critical region as well as the super-critical region, y^+ which is smaller than 5 applied in this work to model and mesh the domain.

3.2.2.4. Meshing

A structured hexahedral mesh is employed in this simulation. The structured nature of the mesh provides the easy availability to control the boundary layer. This is very important for computing the juncture flow. Near to the cylinder wall, a very fine mesh is required to resolve the flow parameters in the boundary layer. The mesh becomes increasingly coarse in the radial direction to maintain computational efficiency. This can be achieved by setting up the desired growth factor for the coarsening of the mesh away from the wall. In all cases, the growth factor is 1.1.

The process of meshing domains is performed by using GAMBIT. From three above-mentioned domains, three kinds of mesh are generated as Figure 3.6.

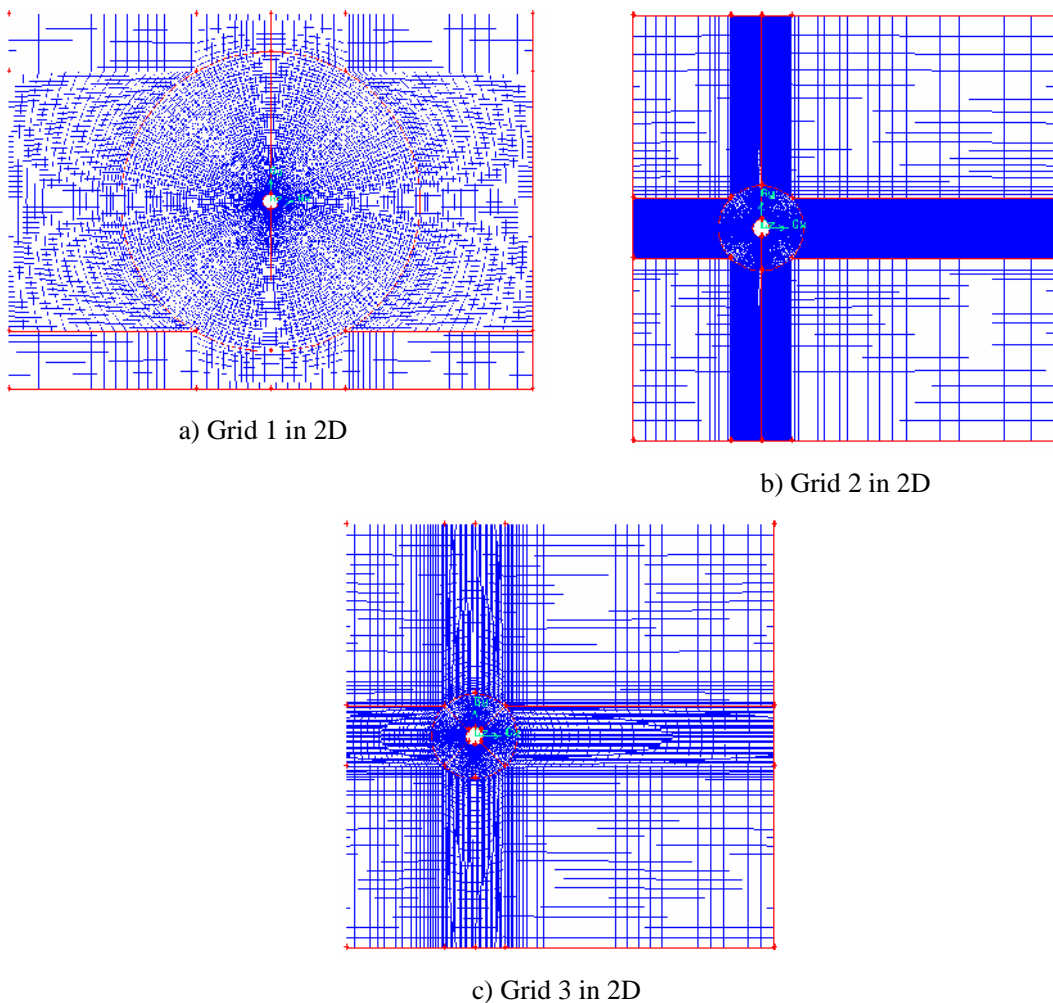


Figure 3.6. Some types of mesh used to calculate the flow around a circular cylinder

Table 3.1. The number of cells in each Grid

Type of grid	Number of cells		First length
	2D	3D	y_l
Grid 1	15,068	1,356,120	0.0001
Grid 2	21,492	1,934,280	0.0005
Grid 3	16,964	1,526,760	0.0001

3.2.2.5. Discretization

Equation discretization (Section 2.2.1.4) of the RANS models is achieved by using the upwind differencing scheme. Advection scheme with level of second order accuracy has been tested and compared for the simulations on the flow around a circular cylinder. Euler implicit time-stepping scheme is used for the time marching procedure.

3.2.2.6. Computer power

The availability of computer power affects the accuracy of CFD solution so much. The stronger computer power is, the higher the accuracy is. However, with current condition, the simulations using the RANS models are based on a single Pentium Dual Core inside (1.8GHz processor) desktop PC with 1.96GB of physical RAM. Besides, the computing time also depends very much on the availability of computer power. If the computer power is strong, the computing time is short. To provide a basic idea on the computing time for the simulation, current RANS models require approximately 1 or 2 days simulation time for a mesh size of 1.5 to 1.9 million elements of $Re = 1,000,000$. On the other hand, with $Re = 3900$, the computing time will reduce half a day or even less than.

3.2.2.7. Number of iterations and convergence

The residuals of convergence of the solution are always maintained at 10^{-5} to ensure that the errors can be acceptable. The number of iterations in the simulation is 8000 iterations, which has been found to be enough for the flow to develop completely.

3.2.2.8. Results and discussion

The simulations are performed in both 2D and 3D models. The table 3.2, 3.3 and table 3.4 show the changes of the drag coefficient estimated by the RANS models with simulations of different meshes and second order of accuracy. Results for Reynolds numbers of 3,900 and 1,000,000 are shown. The table 3.1 shows the values of the drag coefficient (C_d) from the estimation of the RANS models with $Re = 3,900$ and 2D computational domains. The changes of drag coefficient against Reynolds number with the refinement of mesh are then compared with the experimental data from Norberg (1987). Based on this table, it is obvious that the S-

A model with Grid 3 predicted the drag coefficient very well because the minimum error is 1.77%.

Table 3.2. Drag coefficient of the flow around a circular cylinder using the RANS turbulence models with 2D computational domain and $Re = 3900$

Mesh	Turbulence models	C_d in Simulation	C_d in Experiment [46]	Error (%)
Grid 1	S-A	1.3266154	0.99	34.00156
	k-epsilon standard	1.2593802		27.21012
	k-epsilon RNG	0.86013162		13.11802
	k-epsilon Realizable	0.90806706		8.276055
	k-omega SST	1.2533483		26.60084
Grid 2	S-A	1.1225342		13.38729
	k-epsilon standard	1.1080558		11.92483
	k-epsilon RNG	0.8054877		18.63761
	k-epsilon Realizable	0.80758737		18.42552
	k-omega SST	1.0967027		10.77805
Grid 3	S-A	1.0078985		1.807929
	k-epsilon standard	0.93309421		5.74806
	k-epsilon RNG	0.75415646		23.82258
	k-epsilon Realizable	0.73152946		26.10814
	k-omega SST	0.83614964		15.54044

RANS turbulence models with $Re = 1,000,000$ in 2D computational domain. These results are also compared with experimental data from Zdravkovich (1997). According to Table 3.3, the best result of drag coefficient is 3.96671. This means that the error is approximately 4%, as well as is the minimum error which the simulations obtained.

Table 3.3 Drag coefficient of the flow around a circular cylinder using the RANS turbulence models with 2D computational domain and $Re = 1,000,000$

Mesh	Turbulence models	C_d in Simulation	C_d in Experiment [75]	Error (%)
Grid 1	S-A	0.47658184	0.4	19.14546
	k-epsilon standard	0.64576515		61.44129
	k-epsilon RNG	0.32909509		17.72623
	k-epsilon Realiable	0.39254457		1.863858
	k-omega SST	0.57850181		44.62545
Grid 2	S-A	0.508414		27.1035
	k-epsilon standard	0.61138035		52.84509
	k-epsilon RNG	0.36979109		7.552228
	k-epsilon Realiable	0.37590202		6.024495
	k-omega SST	0.65419354		63.54839
Grid 3	S-A	0.38413316		3.96671
	k-epsilon standard	0.55247034		38.11759
	k-epsilon RNG	0.32587821		18.53045
	k-epsilon Realiable	0.34463013		13.84247
	k-omega SST	0.46161484		15.40371

To find the most suitable grid and turbulence model, the 3D computational domains have been tested with $Re = 1,000,000$. The results of these simulations are shown in the table 3.4. Once more time, they are compared with experimental data which obtained from Zdravkovich (1997). In 3D, the drag coefficient in most simulations is changed completely. In particular, with the same S-A model, the drag coefficient in 3D is smaller than that in 2D about 1.7%. However, the result in 3D is close to experimental data more than that in 2D (the errors are 3.97% and 2.35%, respectively). This is also the best result.

Table 3.4. Drag coefficient of the flow around a circular cylinder using the RANS turbulence models with 3D computational domain and $Re = 1,000,000$

Mesh	Turbulence models	C_d in Simulation	C_d in Experiment [75]	Error (%)
Grid 1	S-A	0.3759	0.4	6.025
	k-epsilon RNG	0.35183991		12.04002
	k-epsilon Realizable	0.34843775		12.89056
	k-omega SST	0.45771024		14.42756
Grid 2	S-A	0.48268798		20.672
	k-epsilon RNG	0.41781923		4.454807
	k-epsilon Realizable	0.36106899		9.732753
	k-omega SST	0.55113265		37.78316
Grid 3	S-A	0.39060602		2.348495
	k-epsilon RNG	0.35844481		10.3888
	k-epsilon Realizable	0.36469221		8.826948
	k-omega SST	0.46612037		16.53009

3.3. Conclusion

The grid generation was viewed as one of the key important considerations during the pre-process stage following the definition of computational domain geometry. As a result, it makes up more than 60% effort of simulation. Obviously, it can determine the success or failure in attaining a computational solution. Next, choosing the turbulence model is also very important. Among the RANS models tested on the flow around a circular cylinder, the S-A model demonstrated the ability to predict the drag coefficient similar to experimental data. In addition, the effect of grid resolution was tested and the Grid 3 predicted the drag coefficient close to experimental result at both lower Reynolds number of 3,900 and higher Reynolds number of 1,000,000. Two recirculation bubbles were captured in the near wake. From the above results, the S-A model and the Grid 3 are respectively the most suitable and appropriate model and mesh which will be used to simulate the complex cases in next chapter.

4. FLOW AROUND A CIRCULAR CYLINDER

Flow around a circular cylinder is a basic fluid mechanics problem of practical importance. It has been applied to many fields such as ship structures, off shore structures, bridge piers, pipelines, etc. That is why it has been the subject of numerous investigations, of theoretical, experimental, and more recently numerical variety for the past century. Extensive reviews of the knowledge accumulated on this flow appear every decade as Morkovin (1964), Berger & Wille (1972), Norberg (1987), yet our understanding of the subjacent physics is incomplete. The relevant non-dimensional parameter in the flow is the Reynolds number, but because of sensitivity to experimental conditions, global statistics such as drag, pressure coefficient, and Strouhal frequency vary by as much as 25% from one experiment to the next at a fixed Reynolds number, see Cantwell & Coles (1983). These variations indicate that in addition to the Reynolds number, several parameters arising from experimental set-ups are important in the cylinder flow. These include the blockage ratio, the free-stream turbulence intensity, the cylinder aspect ratio, and the end boundary conditions, each of which has been the subject of numerous studies. Braza et al. (1986), Countanceau and Defaye (1991), L. Ong and J. Wallace (1996), E.A. Anderson and A. A. Szewczyk (1997) and recently, Meng Wang et al. (2001) and Besir Sahin et al. (2006) have investigated the pressure and velocity fields in the near wake of a circular cylinder. The common points of interest of these works are the development of the primary unsteady wake behind the circular cylinder and the evaluation of the drag, lift coefficients, and the separation angle with time.

Most of the experimental studies investigated the steady and unsteady behaviors of vortices in the wake area. Besides these theoretical and numerical investigations, some experimental visualization has been done. The work of Tritton (1959) was carried out with the range of low Reynolds numbers from 0.5 to 100. Later, Roshko (1960) tested with very high Reynolds number from 10^6 to 10^7 . Until now, many researchers continue carrying out the experiments to understand the nature of the flow around the circular cylinder deeply and fully.

This chapter focuses on validating and determining suitable turbulence models in the application of the flow around a circular cylinder. Afterwards, the validated turbulence model will be applied to the simulation of flow around the circular cylinder with different inclined angles. The first step of the validation process relates to the simulation of flow around a circular cylinder using different turbulence models at some Reynolds number to obtain some basic parameters of flow and the vortex shedding phenomenon in the wake region. Next, the comparison between the simulation data and experimental data is conducted to find the most

appropriate turbulence model at the Reynolds number of 3900. Finally, this model will be applied to simulate the flow around a circular cylinder mounted the flat plate or curved plate with various inclined angles.

To do that, the overview of the flow around a circular cylinder and the basic parameters of the flow such as the drag, lift and pressure coefficients, the Strouhal number and the vortex shedding are presented.

4.1. Conceptual overview of flow around a circular cylinder

According to Patrick Beaudan and Parviz Moin's research (1995), the flow field past the circular cylinder is symmetric at low values of low Reynolds number. This is known as laminar flow. When the Reynolds number increases, flow begins to separate behind the cylinder. The flow separation tends to roll up the flow into swirling eddies, resulting in vortex shedding in the wake region of the flow known as the Von Karman vortex. This is an unsteady phenomenon.

4.1.1. Reynolds number

The flow over a circular cylinder is very sensitive to the changes of Reynolds number because the non-dimensional quantities describing the flow around a circular cylinder depend on the Reynolds number. At low Reynolds number, inertial forces are smaller than viscous forces. The naturally occurring disturbances are dissipated away and the flow remains laminar. At high Reynolds number, the inertial forces are sufficiently large to amplify the disturbances, and a transition to turbulence occurs. Reynolds number of the flow around a circular cylinder can be defined as follows:

$$\text{Re} = \frac{u \cdot D}{\nu} \quad \text{Eq. 4.1}$$

where D is the diameter of the cylinder, u is the inlet velocity of the flow, and ν is the kinematic viscosity of the flow.

From the studies of the flow around a circular cylinder, Tritton (1959) and Roshko's (1960) were pointed out regions where significant patterns of flow occur as the Reynolds number changes, especially when the flow changes from laminar to turbulent state. A broad classification of the cylinder flow behavior in different regimes of Reynolds number is presented in table (4.1), which also lists some representative experiments for each flow regime.

Table 4.1. Summary of cylinder flow regimes

Regime	Reynolds number	Flow characteristics	Experiments
Steady	0 → ~ 5	Attached boundary layer	Kovaszny (1949) Coutanceau & Bouard (1977) Tritton (1959), (1971)
	~ 5	Flow convectively unstable	
	5 → ~ 40	Symmetric, attached twin vortices	
	~ 25	Flow absolutely unstable (Parallel stability theory)	
Unsteady Laminar	40 → 150	Stable vortex street, decaying downstream	Williamson (1989)
	~ 90	Oblique vortex shedding	
Transitional	150 → 300	Transition to turbulence in the wake. Fully turbulent wake in 40~50D downstream	Cantwell & Coles (1983) Roshko (1954a)
Sub-critical	300 → 2×10^5	Transition in the free shear layers	Achenbach (1968) Norberg (1987) Delaney & Sorensen (1953)
	$\geq 10^4$	Most of the shear layers is turbulent Base pressure insensitive to Re	
Critical	$2 \times 10^5 \rightarrow 7 \times 10^5$	Lower transition in C_d from ~1.2 to ~0.3 Near wake width decreases to less than 1D Separation moves to rear of cylinder Laminar separation, transition, reattachment and turbulent separation of boundary layer	Roshko (1961) Shih et al. (1992)
	$7 \times 10^5 \rightarrow 4.5 \times 10^6$	Upper transition in C_d from ~0.3 to ~0.7 Near wake width increases (stay less than 1D) Separation point moves forward	
Post-Critical	$\geq 4.5 \times 10^6$	Turbulent cylinder boundary layer Regular vortex shedding ($St \approx 0.27$), $C_d \approx 0.7$ Transition precedes separation, no reattachment	

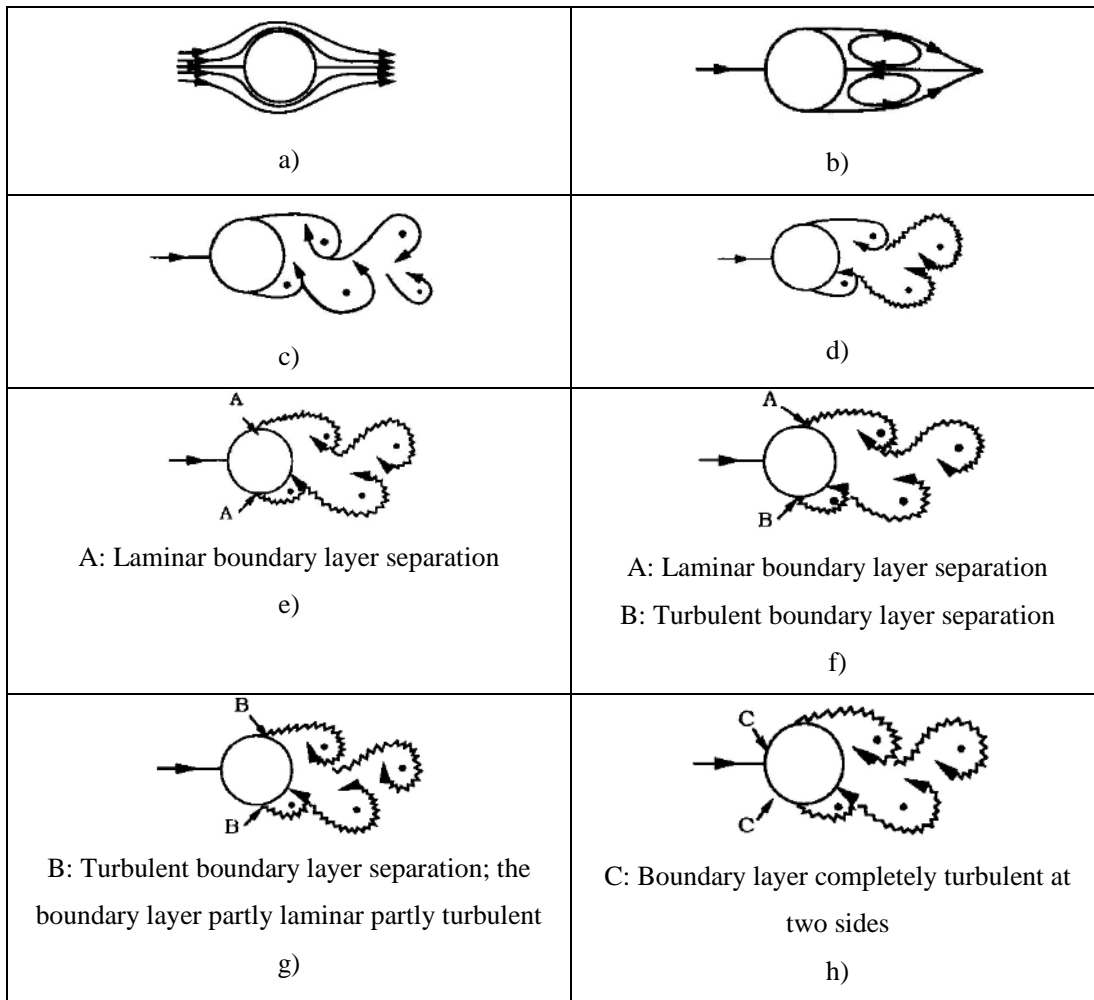


Figure 4.1. Regimes of flow around a smooth, circular cylinder in steady current

At Reynolds numbers less than approximately 40, the flow is laminar and steady. For the small values $Re < 3.2$, no separation occurs (Figs. 4.1a). The boundary layer on the cylinder surface separates at a Reynolds number of 3.2 (see Nisi & Porter (1923)) to 5 (see Taneda (1956)), and a pair of steady symmetric vortices (Figs. 4.1b) form behind the cylinder. A large body of early experimental work has documented that range of Reynolds numbers, detailing the main features of the boundary layer and near wake region, e.g. Tritton (1959), Coutanceau & Bouard (1977), Thom (1933), Taneda (1956), and Acrivos et al. (1965). Between Reynolds numbers 10 and 40, the velocity profiles in the wake are self-similar past 10 diameters downstream of the cylinder; the length of the recirculation zone behind the cylinder grows linearly with Reynolds number, and the velocity distributions on the rear symmetry axis in the recirculation zone at different Reynolds numbers exhibit similarity, see Nishioka & Sato (1974).

For Reynolds numbers higher than approximately 40, a characteristic frequency expressed in non-dimensional form as the Strouhal number is associated with the wake. Taneda (1956) puts the critical Reynolds number at which shedding first occurs at which shedding first occurs at 30, whereas Homman (1936), Kovasznay (1949) and Roshko (1945b) find that shedding starts at Reynolds number 40. Local linear parallel stability theory applied to the cylinder wake (see Monkewitz (1988)) indicates that the flow becomes absolutely unstable at Reynolds number 25, approximately two-thirds the value at which a instability cannot by itself predict a precise Strouhal frequency even at the onset of vortex shedding.

For the range of the Reynolds number $40 < Re < 150$, the vortex street is laminar (Figs. 4.1c). The shedding is essentially two-dimensional, i.e., it does not vary in the span wise direction. For Reynolds numbers up to 150, the flow remains laminar, see Bloor (1964) and Roshko (1954a), the shed vorticity decays as it convects downstream, and the Strouhal number increases with Reynolds number. A least-square curve-fit of the Strouhal curve for Reynolds number between 50 and 180 is given by:

$$St = A/Re + B + CRe$$

Where $A = -3.3265$, $B = 0.1816$ and $C = 1.6 \cdot 10^{-4}$ (Williamson 1991).

Transition to three-dimensionality in the near wake occurs around $Re = 180$ (Figs. 4.1d), and is signaled by two discontinuities in the Strouhal-Reynolds number relation. The first, around $Re=180$, arises from the generation of vortex loops evolving into pairs of counter-rotation streamwise vortices in the wake, the second comes from a transition to fine-scale streamwise vorticity at $Re = 230-260$.

At Reynolds numbers between 300 and 2×10^5 , the sub-critical range, the flow around the entire periphery of the cylinder is laminar (Figs. 4.1e), and transition to turbulence occurs in the separated free shear layers, see Cardell (1993). At the lowest Reynolds numbers in this range, the wake becomes fully turbulent in 40 to 50 cylinder diameters downstream; see Uberoi (1969), after which distance the regular vortices have completely decayed. At the higher end of the Reynolds number range, transition occurs very near the wall surface and the wake is fully turbulent close downstream of the cylinder, seeing Cantwell & Coles (1983). For Reynolds numbers larger than 10^4 , transition in the shear layers occurs very close to the separation points, and the base-pressure coefficient, drag coefficient and Strouhal number are approximately constant at values of -1.1 , 1.2 and 0.2 respectively as Roshko and Fiszdon (1969).

The critical range of Reynolds numbers, between 2×10^5 and 4.5×10^6 , displays two transitions in the drag coefficient, labeled the lower and upper transitions by Roshko (1961). In the lower

transition range ($2 \times 10^5 < Re < 7 \times 10^5$), the drag coefficient drops abruptly from 1.2 to about 0.3 due to an increase in base pressure at a Reynolds number of approximately 3.6×10^5 . A laminar separation of the boundary layer is followed by transition to turbulence, reattachment and a final turbulent separation (Figs. 4.1f). The separation point moves from the front to the downstream side of the cylinder, and the width of the near-wake decreases to less than 1 diameter. In the upper transition region ($7 \times 10^5 < Re < 4.5 \times 10^6$), the base-pressure coefficient decreases monotonically from approximately -0.2 to -0.5, while the drag coefficient increases from 0.3 to 0.7, and remains at that value for Reynolds numbers of up to 10^7 . The boundary layer is completely turbulent on one side of the cylinder and partly laminar and partly turbulent on the other side (Figs. 4.1g). With increasing Reynolds number the separation point moves forward, but it remains on the downstream side of the cylinder, and the wake width increases but stays smaller than 1 diameter. The sensitivity of the flow to disturbances in the critical regime, in particular the non-zero mean lift which can develop around the cylinder, has been experimentally investigated by Schewe (1986).

In the post-critical regime, past Reynolds number 4.5×10^6 , the boundary layer over the cylinder surface is virtually turbulent everywhere (Figs. 4.1h). The separation-reattachment bubble present in the critical region disappears. The base-pressure coefficient pursues its monotonic decrease started at Reynolds number 5×10^5 , reaching -0.6 at Reynolds number 8×10^6 ; the drag coefficient is constant at around 0.7, and vortices are shed regularly at an approximately constant Strouhal frequency of 0.27, see Roshko (1961)).

4.1.2. Vortex shedding

The most important feature of the flow regimes described in Section 4.1.1 is the vortex shedding phenomenon, which is common to all the flow regimes for $Re > 40$ (Fig 4.1). When the Reynolds number is increased, the boundary layer over the cylinder surface will separate due to the adverse pressure gradient imposed by the divergent geometry of the flow at the rear side of the cylinder. As a result of this, a shear layer is formed. This shear layer contains a significant amount of vorticity. This vorticity is fed into the shear layer formed downstream of the separation point and causes the shear layer to roll up into a vortex with a sign identical to that of the incoming vorticity (Vortex A in Fig. 4.2). Likewise, a vortex, rotating in the opposite direction, is formed at the other side of the cylinder (Vortex B). This meant that pairs of eddies form alternatively on the top and bottom part of the cylinder and move into the wake region resulting in vortex shedding.

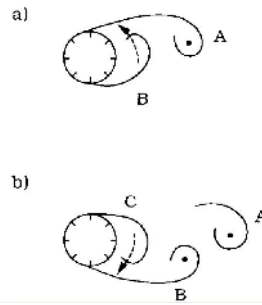


Figure 4.2 Formation and development of vortex shedding in the wake region of the flow around a circular cylinder

a) Prior to shedding of Vortex A, Vortex B is being drawn across the wake.

b) Prior to shedding of Vortex B, Vortex C is being drawn across the wake.

The larger vortex (Vortex A in Fig. 4.2a) presumably becomes strong enough to draw the opposing vortex (Vortex B) across the wake, as depicted in Fig. 4.2a. The vorticity in Vortex A is in the clockwise direction (Fig. 4.2b), while that in Vortex B is in the anti-clockwise direction. The approach of vorticity of the opposite sign will then cut off further supply of vorticity to Vortex A from its boundary layer. This is the instant where Vortex A is shed. Being the free vortex, Vortex A is then convected downstream by the flow.

Following the shedding of Vortex A, a new vortex will be formed at the same side of the cylinder, namely Vortex C (Fig. 4.2b). This will lead to the shedding of Vortex B. Now, Vortex B will play the same role as Vortex A, namely it will grow in size and strength so that it will draw Vortex C across the wake (Fig. 4.2b). This will cause the shedding of Vortex B. The process will continue each time a new vortex is shed at one side of the cylinder where the shedding will continue to appear in an alternate manner between the sides of the cylinder.

4.1.3. Strouhal number

The characteristic of vortex shedding is vortex-shedding frequency. It can on dimensional grounds be seen to be a function of the Reynolds number:

$$St = St(Re) \quad \text{Eq. 4.2}$$

In which

$$St = \frac{f_s D}{u} \quad \text{Eq. 4.3}$$

where D is the diameter of the cylinder, f_s is the shedding frequency of vortices and u is the incident velocity. The normalized vortex shedding frequency, namely St , is called the Strouhal number. In Fig. 4.3, Williamson et al. (1989) showed that how the Strouhal number varies with the Reynolds number. The vortex shedding first appears at $Re = 40$. From Fig. 4.3, the shedding frequency St is approximately 0.1 at this Re . It then gradually increases as Re is

increased and attains a value of about 0.2 at Re 300, the lower end of the sub-critical flow regime. From this Re number onwards throughout the sub-critical range ($300 < Re < 10^4$), the vortex shedding frequency at which vortices are shed in the flow around a circular cylinder tends to remain almost constant.

As seen from Fig. 4.3, the Strouhal frequency experiences a sudden jump at $Re=3-3.5 \times 10^5$, namely in the critical Re number range, where St increases from 0.2 to a value of about 4.5. This high value of St is maintained over a rather large part of the supercritical Re range, subsequently it decreases slightly with increasing Reynolds number.

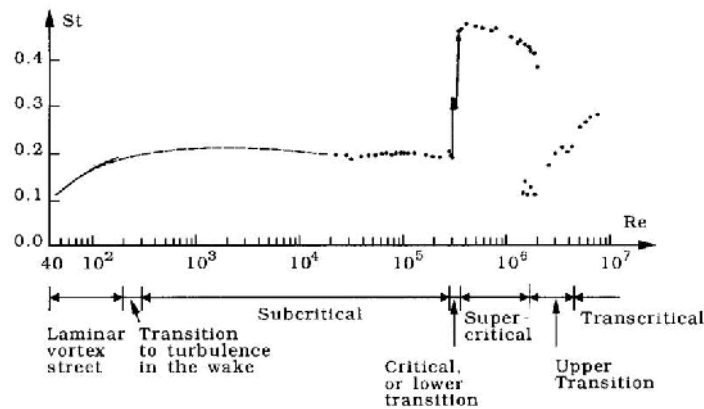


Figure 4.3 Strouhal number for a smooth circular cylinder. Experimental data from: Solid curve: William (1989). Dashed curve: Roshko (1961). Dots: Schewe (1983).

The large increase in St in the supercritical-flow range is explained as follows: in the supercritical flow regime, the boundary layer on both sides of the cylinder is turbulent at the separation points. This results in a delay in the boundary layer separation where the separation points move downstream, as sketched in Fig. 4.4. This means that the vortices (now being closer to each other) would interact at a faster rate than in the subcritical flow regime, which would obviously lead to higher values of the Strouhal number.

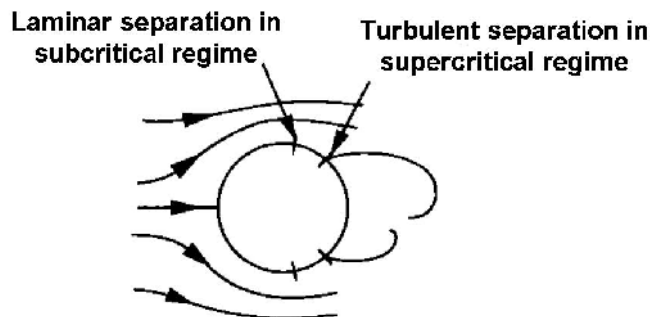


Figure 4.4. Sketch showing positions of separation points at different separation regimes
From the experimental data, Williamson built a new formulation for the relationship between Strouhal number versus the Reynolds number for the cylinder wake as:

$$St = 0.266 - \frac{1.018}{\sqrt{Re}} \text{ for the range of the Reynolds number } Re < 190 \quad \text{Eq. 4.4}$$

$$St = 0.2234 - \frac{0.349}{\sqrt{Re}} \text{ for the range of the Reynolds number } 190 < Re < 1200 \quad \text{Eq. 4.5}$$

For the range of the Reynolds number $2000 < Re < 10^5$, one might then expect that the Strouhal number will reach a saturation value equal to the constant of 0.2234.

This relationship is very important for simulating and solving the unsteady flow problem because we can determine the initial value of time step size Δt based on the Reynolds number throughout the Strouhal number.

4.1.4. Drag and lift coefficients

According to Roshko (1994), the Strouhal number is related to the drag coefficient of the flow. A decrease of the drag coefficient will accompany an increase of the Strouhal number in the range of Reynolds number ($100 < Re < 10,000$).

Drag coefficient is a dimensionless factor of proportionality between overall hydrodynamic force vector \vec{F} on a body in a liquid or gas flow and the product of reference area A of the body and velocity. Drag coefficient is computed as below:

$$C_d = \frac{F}{\frac{1}{2} \rho u^2 A} \quad \text{Eq. 4.6}$$

where the drag force F is the sum of the pressure drag force and the friction drag force components on the cylinder surface acting in the flow direction (Figure 4.5) and A is the reference area.

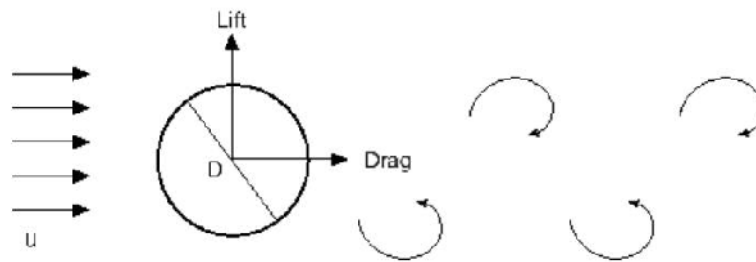


Figure 4.5. Forces acting on the cylinder

Defining the reference area A is very important for calculating the drag coefficient. This area depends on what type of drag coefficient is being measured. The frontal area of the object projected on a plane normal to the flow is the most common reference area. Others include the wetted area, the plan form area, and the two-thirds power of volume. A reference area is often

selected arbitrarily but can significantly influence the calculated drag coefficient. Vogel (1984) suggested that:

- Frontal area is most appropriate for streamlined objects at high Re values when drag is essentially the dynamic pressure times the frontal area of the object.
- Wetted area is most relevant for streamlined objects for which the drag is due to viscosity and shear;
- Plan area is preferred for objects with significant lift, such as airfoils;
- And the two-thirds volume would be appropriate for objects with lift proportional to volume, such as airships.

Lift coefficient is calculated similarly but vertical force is considered rather than the flow-direction force.

In practice, the drag coefficient is calculated in most cases using empirical relations generalizing experimental data. Figure 4.6 shows the dependence of drag coefficient for a cylinder and sphere on the Reynolds number. The drag coefficient decreases drastically from extremely high values at small Reynolds numbers, to unity and lower at $Re > 10^3$. With increasing Reynolds number, inertial forces begin to predominate over viscosity forces and a laminar boundary layer is originated. Flow beyond the boundary layer is virtually not affected by viscosity. Flow separation in the stern (point S in Figure 4.6) also occurs. Because Reynolds number grows, the area of separation increases and attains the highest values at $Re \sim 10^3$; the drag coefficient in this case no longer diminishes and even slightly increases, remaining close to 0.4 for the range $2 \cdot 10^3 < Re < 2 \cdot 10^5$.

If Reynolds number continues to increase, the situation arises when the laminar boundary layer becomes partially turbulent in the non-separating flow region of the cylinder. The velocity profile in the turbulent boundary layer is fuller and better resists a positive pressure gradient. The separation is sharply displaced toward the stern, thereby drastically decreasing the drag coefficient. With further enhancement of the Reynolds number, drag coefficient remains unchanged.

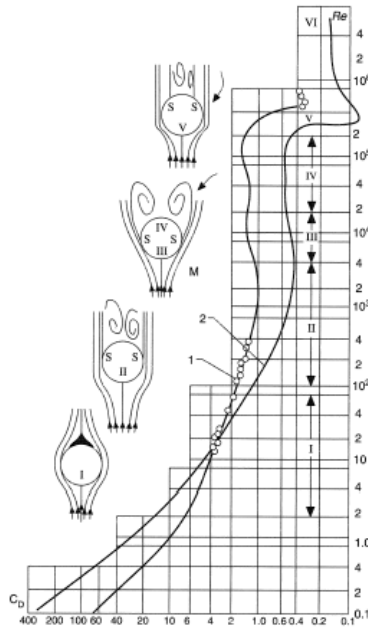


Figure 4.6. Drag coefficient for cylinders (1) and spheres (2) as a function of Reynolds number (Re), Polezhaev et al. (2003)

For general flow relating to separation, the drag force is changing at twice the frequency of the lift force for the flow around a circular cylinder. A suction area is created when a vortex is shed from the top of the cylinder. This results in that the cylinder experiences lift. An alternate vortex is created at the bottom part of the cylinder in half a cycle later. Throughout this process, the lift force changes alternately in a complete cycle of vortex shedding but the cylinder experiences drag constantly.

4.1.5. Pressure coefficient

Like the drag and lift coefficient, the pressure coefficient is also important to study the flow around a circular cylinder mounted on a plate. Near to the surface of the cylinder, flow momentum is quite low due to friction effects and thus is sensitive to the changes of the pressure gradient. The pressure acting on each differential element on the surface of the cylinder maybe normalized by the dynamic free stream pressure to obtain the pressure coefficient. In order to compare the variation of pressure around a cylinder for a variety of flow conditions, it is conventional to use a dimensionless ratio-the pressure coefficient C_p , which compares the pressure on the surface of the cylinder, P_c , to that at infinity, P_∞ . It is defined by:

$$C_p = \frac{P_c - P_\infty}{\frac{1}{2} \rho U^2} \quad \text{Eq. 4.7}$$

A typical pressure distribution plot of the flow around a circular cylinder starting from the stagnation point is showed in Figure 4.7. Then, the pressure coefficient drops to a negative value when the flow velocity starts to increase. In this case, decreasing of pressure in the direction of flow assists the fluid movement and there is no retardation of flow.

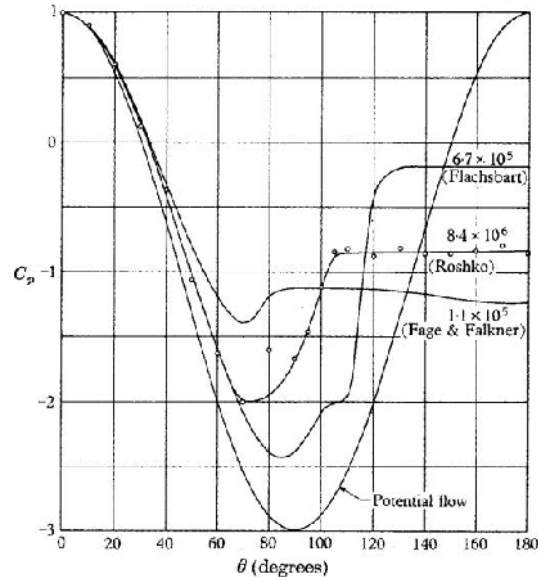


Figure 4.7. Experimental pressure coefficient distributions on cylinder surface compared to theoretical result, Roshko (1960)

When the velocity of the flow reduce to $\theta = 80^\circ$, the pressure in the direction of the flow increases. This results in the adverse pressure gradient situation. Thus, the flow has to move to against the pressure force in addition to the viscous force. Separation of the flow occurs when shear stress cannot overcome the adverse pressure gradient, this happens at $80^\circ < \theta < 120^\circ$ for sub-critical flow. After the separation point, pressure remains constant in the wake. The accurate prediction of pressure coefficient distribution around a cylinder is up to how the turbulence model simulates.

4.2. Flow around a circular cylinder mounted on the flat plate

The simulation of the flow around a circular cylinder mounted on the flat plate based on the RANS method will be discussed in this section. In addition, numerical studies of the flow around a circular cylinder from other researchers are also briefly discussed and compared, followed by the current work employing S-A turbulence model for the computation of the drag coefficient and pressure distribution around the circular cylinder.

4.2.1. CFD simulation

Based on the results of the previous chapter, S-A turbulence model have been chosen to test the suitability and the applicability of the models on the flow around a circular cylinder at

Reynolds number of 3,900, as well as the flow at Reynolds number of 1,000,000. The low Reynolds number of 3,900 in the sub-critical region of flow and the high Reynolds number of 1,000,000 in the super-critical region have been chosen mainly due to the experimental data such as the pressure distribution and drag coefficient are widely available within these Reynolds numbers for comparative study. The RANS model used here employ a finite volume method (FVM) with a structured hexahedral mesh.

4.2.1.1. Computational domain and boundary condition

The domain geometry and the boundary conditions for the simulation of the flow at Reynolds numbers of 3,900 and 1,000,000 are depicted in Figure 3.6.a. The cylinder has the diameter (D) of 0.2m and a depth of 5D to incorporate the span-wise effects. The domain is tested with the longitudinal uniform velocities of 0.0196m/s and 5.019m/s correspond to the Reynolds number of 3,900 and 1,000,000 respectively. In addition, the initial turbulence parameters are also imposed by the turbulence intensity of 4.3658% and 2.1828% with regard to Reynolds number of 3,900 and 1,000,000. With both of these Reynolds numbers, only one length scale of 0.1167m is applied.

4.2.1.2. Meshing

A structured hexahedral mesh is employed in these simulations (Figure 3.7c). The y^+ value of 4 around the surface of the cylinder is chosen. With this value, the thickness of boundary layer can be available for S-A turbulence model to simulate the problem correctly.

4.2.1.3. Discretization

In the RANS model of flow around a circular cylinder, the Navier-Stokes equations are discretized using the upwind differencing scheme. The time discretization is carried out by using a second order accuracy scheme.

4.2.1.4. Computer power

The simulation of flow over a circular cylinder at Reynolds numbers of 3,900 and 1,000,000 are performed on the Pentium Dual Core inside PC. Normally, the simulation at Reynolds number of 3,900 takes 0.5-1 days of computational time (1.5 million elements) compared to 1-2 days for the simulation at Reynolds number of 1,000,000. The residual of the simulation is set up to the fifth order of the actual values for convergence consideration.

4.2.2. Results and Discussion

4.2.2.1. Reynolds number of 3,900

The application of S-A model on the flow around a circular cylinder at Reynolds number of 3,900 is simulated. This flow is characterized by laminar separation region in which transition to turbulence happens in the shear layer, producing large-scale vortices and complex flow in

the near wake region. Counter rotating streamwise vortices which are highly three-dimensional have been observed in the wake region of flow at this Reynolds number.

The choice of this Reynolds number of simulation depends mainly on the experimental data available. For the flow around a circular cylinder at Reynolds number of 3,900, two sets of experimental data provide more details of the time average velocity profiles and Reynolds stress distributions in the wake region of the flow. Lourenco and Shih (1993) used the particle image velocimetry (PIV) technique to measure the velocity profiles within three diameters downstream of the cylinder while Ong and Wallace (1996) documented the distribution further downstream. These data provide useful information for comparative study with numerical solutions.

a. The vertical circular cylinder

The flow in the low vicinity of the juncture has a complex structure caused by the interaction between the plate boundary layer and the horseshoe vortex developed around cylinder. There are some vortices accompanied by separations and reattachments generated around the cylinder. Nevertheless, the particle lines in the plane of symmetry depicts the existence of a large-scale vortex whose kernel is located close to the flat plate at a station of about two third of the cylinder radius, as shown in Fig. 4.8. Hung and Kordullar (1984) when computing the flow around a blunt fin mounted on a flat plate mentioned its appearance. Moreover, instantaneous velocity and pressure fields can provide some features of the vortices generated around the juncture.

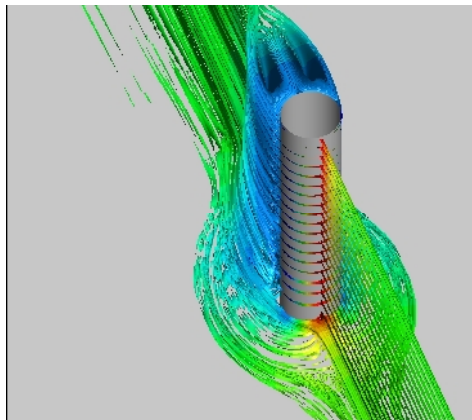


Figure 4.8 Front view of the horseshoe vortex at $Re=3,900$

When the flow along the flat plate approaches the juncture surface, the boundary layer will separate and an array of horseshoe vortices formed due to the large adverse pressure gradient imposed by the divergent geometry of the flow environment at the rear side of the cylinder. The horseshoe vortices wrap around the cylinder. This array maybe formed by one or more

primary horseshoe vortices accompanied by secondary counter-rotating vortex structures is up to the oscillating flow conditions. The trailing structures degrade gradually and interact with the downstream flow of the juncture, as Figure 4.9 shows.

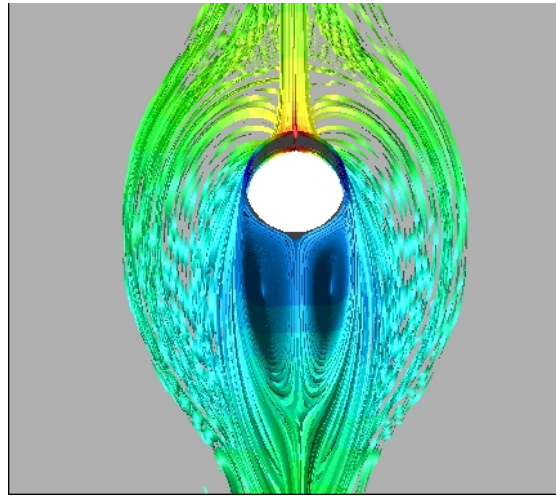
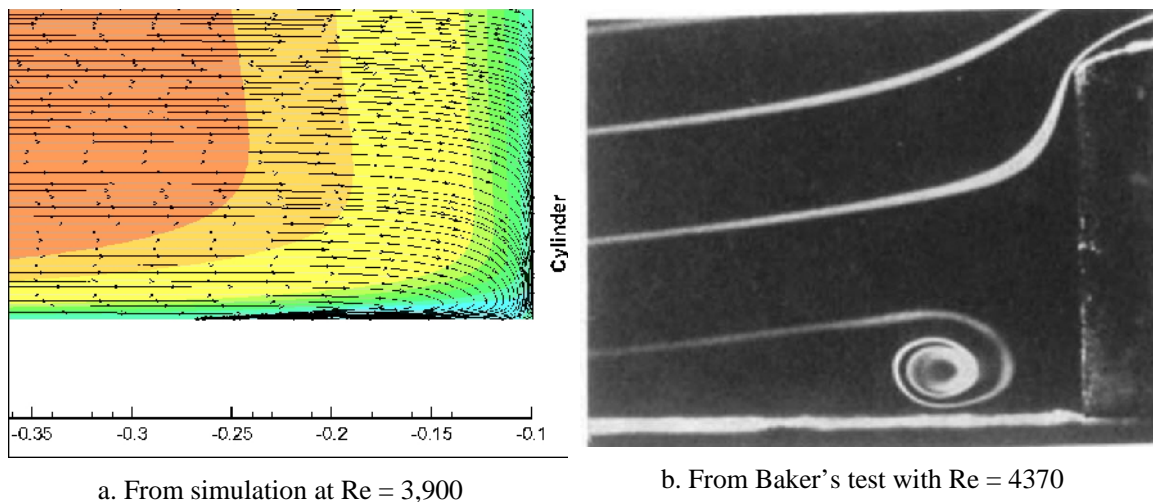


Figure 4.9. Rear view of the horseshoe vortex at $Re=3,900$

A symmetrical configuration was chosen for the numerical simulations in order to isolate, as much as possible the process of the cyclic horseshoe vortex from the Karman vortex street in the wake of the cylinder. The computed flow-field structure on the symmetry plane for $Re=3,900$ is shown in Fig. 4.10a. A primary horseshoe vortex generated in the upstream of the cylinder. The existence of this horseshoe vortex is compared with Baker's experiment (Fig. 4.10b) which was performed at Reynolds number of 4370. The position in which the vortex formed is $0.8D$ from the cylinder. Thus, this distance is quite similar to that reported by Baker (1980). This means that the simulation of the flow around the circular cylinder at $Re=3,900$ describes the practical phenomena correctly.



a. From simulation at $Re = 3,900$

b. From Baker's test with $Re = 4370$

Figure 4.10. The vortex structure in front of the cylinder

The flow structure on the flat plate behind the cylinder reveals a rather symmetrical topology as indicated by Fig.4.11a, which describes the flow topology on the plate surface downstream of the cylinder. The structure here is slightly different from that reported by Visbal (1991) who could describe on a much finer grid the same point as being a half saddle point and a half node of attachment. By analyzing the horseshoe generating mechanism, there are obviously two coexisting structures. The first structure reveals the flow separation from, or attachment to, the solid wall at one point, which can be a half saddle point in the x - z plane and a half-nodal point in the y - z plane. Herein, fluid must flow away from the surface of the plate and the singular point must be a saddle point of separation. The second structure shows a half-nodal point in the x - z plane and a half saddle point in the y - z plane. In this case, fluid enters the singular point; therefore, this point is a saddle point of attachment. The saddle separation point is so-called point S , on the wall from which streamlines appear towards the nodal separation points N_1 and N_2 located on each side of the symmetry plane. There is also a nodal point of separation denoted by N , which lies on the same plane of $y = 0$ as S . Otherwise, this nodal separation point is located at the distance of about four diameters from the cylinder. Moreover, near to the cylinder surface, there are two saddle separation points S_1 and S_2 , which are located symmetrically on the each side.

On the other hand, limiting streamline patterns on the plate showed in Fig. 4.11b present a line of conflation l_c with the saddle point by S_s and a line of divergence l_d associated a node N_A right in front of the cylinder. The surface flow topology shown in Fig.4.11b is of one classical type reported in the literature except for the second horseshoe vortex mentioned only Visbal. This second vortex is weaker than the primary one. It is less available than that it has much effect on the magnitude of the pressures exerted on the cylinder.

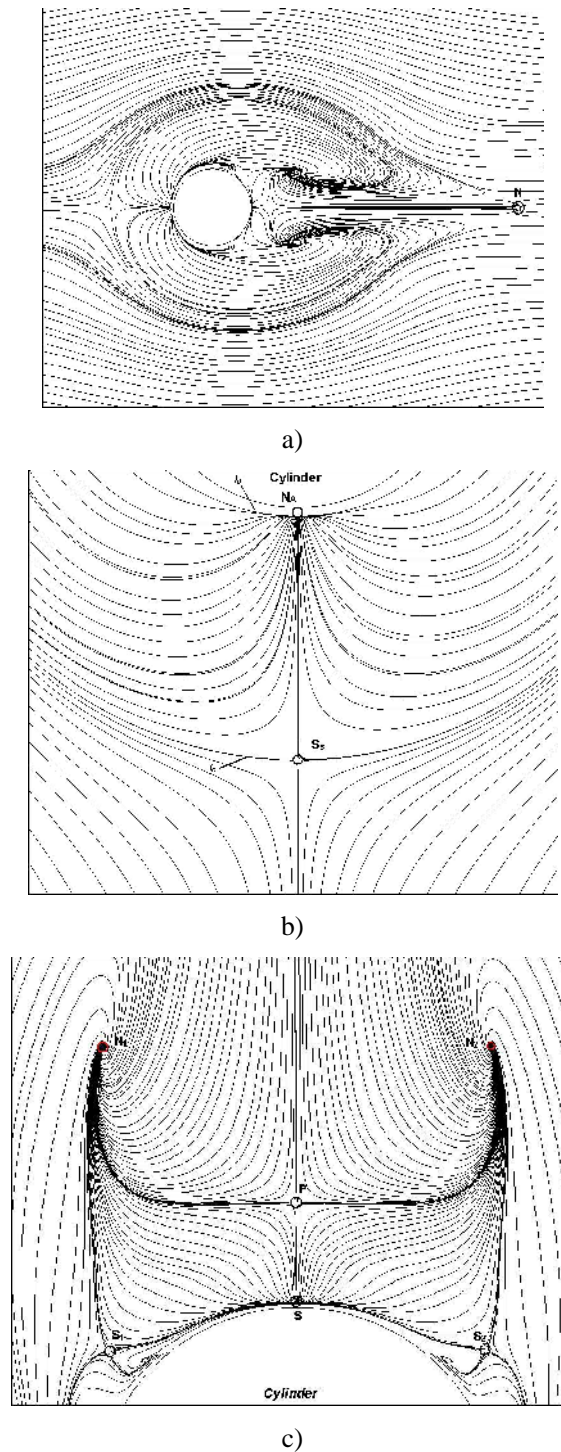


Figure 4.11. Flow topology around the cylinder at $Re = 3,900$

b. The inclined circular cylinder

When the circular cylinder is inclined, the mechanism of flow around juncture in the wake region as well as the pressure and velocity distribution also changes. According to Ishima T. et al. (2008), the inclined angle affects the length of the recirculation zone. Besides, there is a velocity component in perpendicular to the mainstream direction has large difference by the

inclined angle. The numerical simulation in this part has been performed at the Reynolds number of 3,900 aimed not only at clarifying the flow mechanism, but also at providing a complete description on the forces acting on the juncture. Firstly, a comparative analysis of the influence of the stream-wise inclination on the pressure distribution on the cylinder is showed in Figure 4.12. Fig. 4.12a depicts the solution computed on the vertical cylinder, i.e. the inclined angle is zero. Fig. 4.12b shows the solution computed on the circular cylinder inclined at 20° upstream, whereas Fig. 4.12c relates to the solution computed on the cylinder inclined at 20° downstream. The comparison reveals stronger pressure gradients at the root of the cylinder inclined towards the upstream, a fact that maybe caused by the compression of flow and the blockage effect. Figure 4.13 shows a comparison between the solutions computed on the circular cylinder inclined laterally on the flat plate. Fig. 4.13a shows the cylinder inclined by 10° , Fig. 4.13b depicts the cylinder inclined by 20° while Fig. 4.13c presents the solution computed on the cylinder inclined by 30° . The lateral inclination modifies the pressure distribution not only on the cylinder but also on plate. The symmetry of the solution vanishes when the stagnation point moves on the side, which the cylinder inclined. In addition, the stronger pressure gradients are observed in the same side.

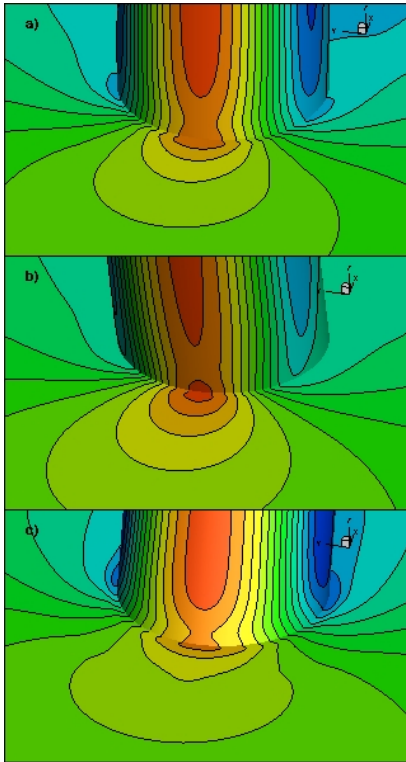


Figure 4.12. Pressure fields around a circular cylinder mounted inclined longitudinally on a flat plate

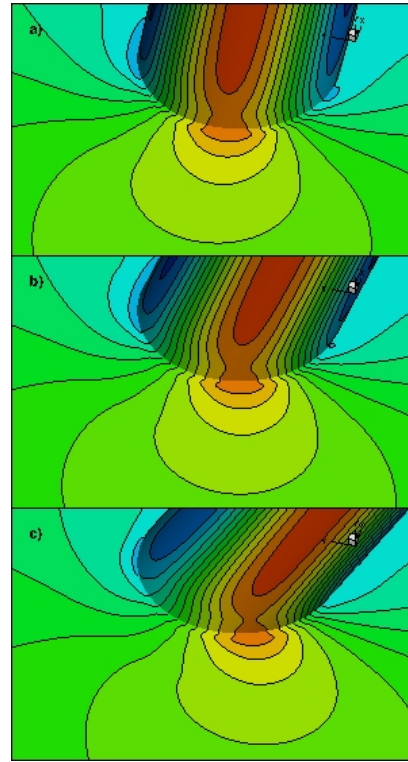


Figure 4.13. Pressure fields around a circular cylinder mounted inclined laterally on a flat plate

4.2.2.2. Reynolds number of 1,000,000

a. The vertical circular cylinder

The increase of the Reynolds number at a value 10^6 leads to a more complicated flow topology. The flow in the immediate vicinity of the juncture has a more complex structure than that in Reynolds number 3,900 see Fig. 4.14. The dimension of the primary vortex decrease compared with $Re=3,900$ because effect of viscosity reduce, as well. The horseshoe vortices in this case fluctuate stronger than those in $Re = 3,900$, as Fig. 4.15 shows. This is caused by the augmentation of the adverse pressure gradients. The trailing structures will decay slowly due to the interaction of the downstream flow.

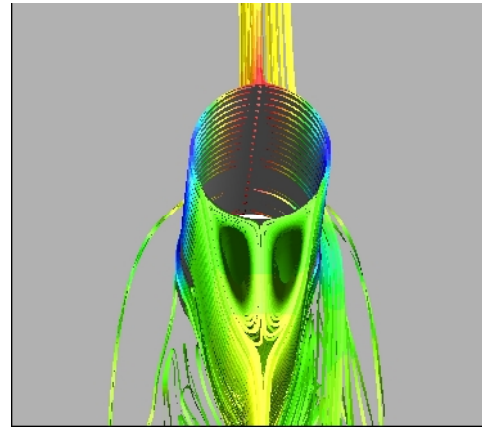
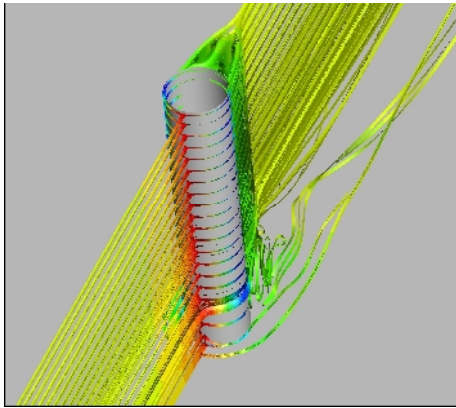
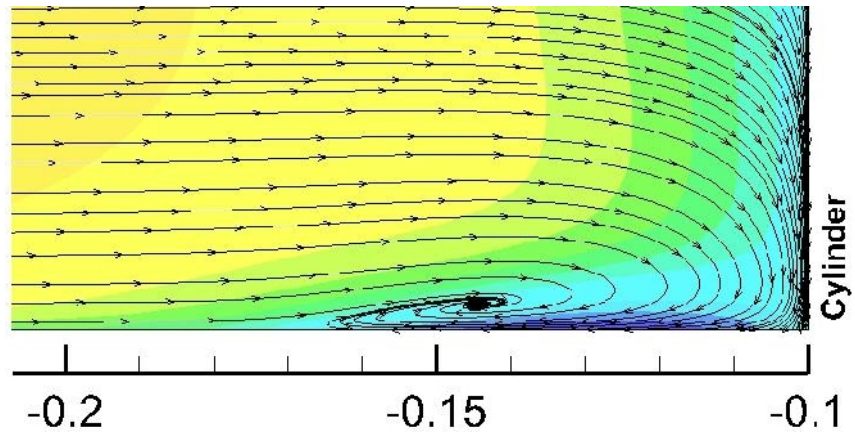
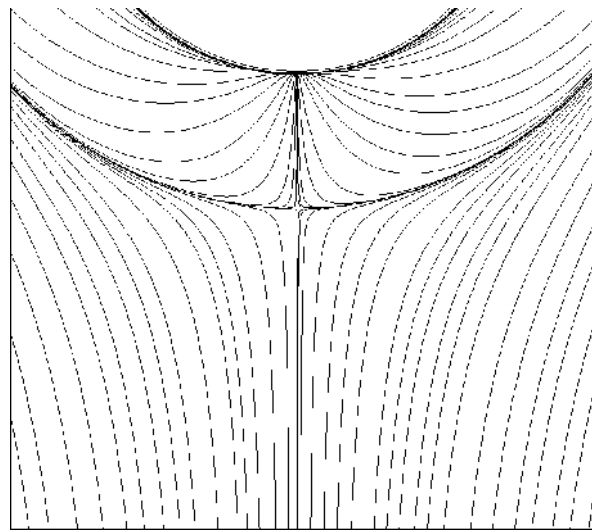


Figure 4.14. Front view of the horseshoe vortex at $Re=10^6$ Figure 4.15. Rear view of the horseshoe vortex at $Re=10^6$

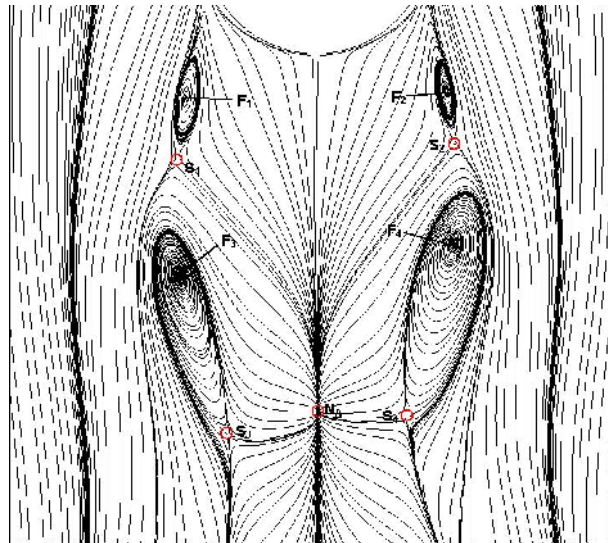
Figure 4.16 presents the computed flow-field structure on the symmetry plane for $Re=10^6$. There is a primary horseshoe vortex forms in front of the cylinder. It is seen easily that the primary horseshoe vortex is larger than that in $Re = 3,900$ case. The streamlines show a reversed flow as well as a spiraling horseshoe with a point of separation that is far from the cylinder. The limiting streamline patterns on the plate depicted in Fig 4.16b is similar to that in $Re = 3,900$. Nonetheless, the flow structure on the flat plate behind the cylinder, as shown in Fig. 4.16c, is different from the case of $Re = 3,900$. The horseshoe vortex system travels downstream of the cylinder and mixes with the fluid of the wake flow region. There are four saddle separation points that are S_1 , S_2 , S_3 and S_4 , respectively. In addition to the saddle points, four vortices unveil with the different dimension. F3 and F4 are the main vortices occupying most of wake flow region. Two smaller scale vortices coalesce to form larger-scale vortices. The existence of four vortex systems is supported by the works of Baker (1980) and Hunt et al. (1978).



a)



b)



c)

Figure 4.16. Streamtraces pattern upstream the cylinder for $Re = 10^6$

b. The inclined circular cylinder

As mentioned in section 4.2.2.1, the stream-wise inclination affects the flow mechanism around the cylinder very much, especially, the pressure and velocity distribution. To find this influence, a comparative analysis is firstly proposed in Figure 4.17. Fig. 4.17a shows the solution computed on the cylinder inclined at 20° upstream, Fig. 4.17b presents the solution computed on the vertical cylinder; on the contrary Fig. 4.17c refers to the solution computed on the cylinder inclined at 20° downstream. Like the case of $Re = 3,900$, the stronger pressure gradients appears at the root of the cylinder inclined towards. It is resulted in the phenomena of flow compression. Figure 4.18 shows a comparison between the solutions computed on the cylinder inclined laterally on the flat plate. Fig. 4.18a shows the cylinder inclined by 10° , Fig. 4.18b depicts the cylinder inclined by 20° while Fig. 4.18c bears the solution computed on the cylinder inclined by 30° . When the cylinder is inclined laterally, both the pressures on the cylinder and on the plate change. The symmetrical characteristic of pressure distribution disappears. Furthermore, the stagnation point also moves on the side that the cylinder is inclined towards. The stronger pressure gradients are observed on the same side, as well.

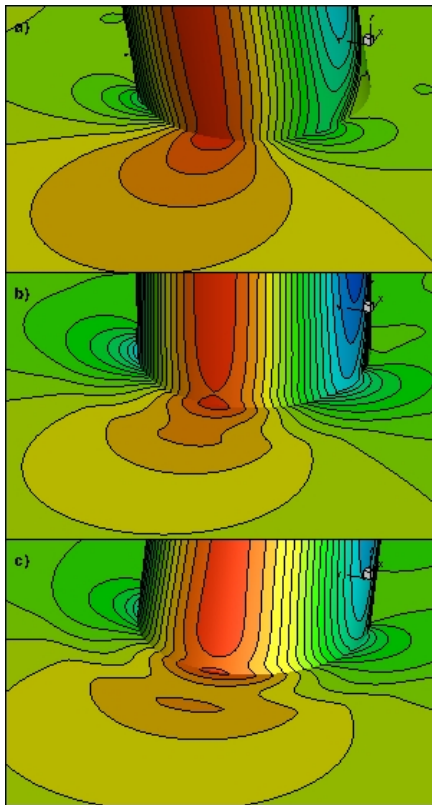


Figure 4.17. Pressure fields around a circular cylinder mounted inclined longitudinally on a flat plate

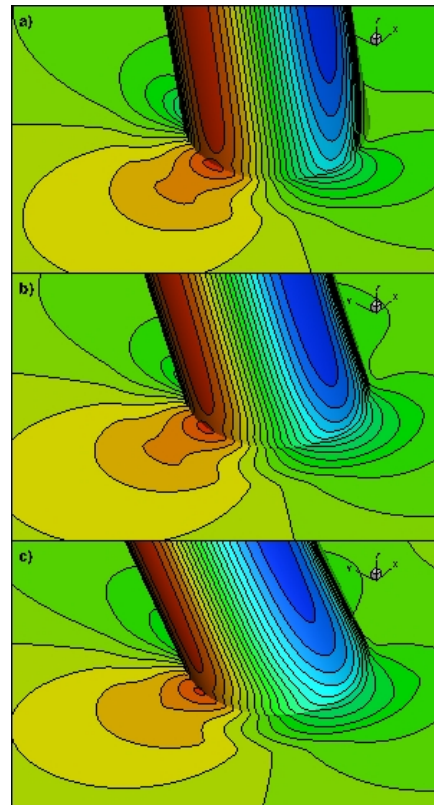


Figure 4.18. Pressure fields around a circular cylinder mounted inclined laterally on a flat plate

4.3. Flow around a circular cylinder mounted on the curved plate

In the previous part, the simulation of flow around a circular cylinder mounted on the flat plate has been discussed and investigated. This part investigates the influence of curved plate on the pressure distribution as well as the forces acting on the cylinder. The results of simulation will be plotted and presented. However, a comparison can not be performed because lack of experimental data. As aforementioned, although, the flow past the cylinder has been subjected to research and study from many recently decades, the effect of curved plate on the juncture flow is not yet fully understood. There is no established method for estimating the wake characteristics behind the cylinder which the shape change of plate is taken into account. Most of experimental studies as well as numerical studies focus on the inclination of cylinder mounted on the flat plate. Ishima T. et al. (2008) performed and investigated flow characteristics around an inclined circular cylinder with fin. They use PIV (Particle image velocimetry) and LDA (Laser Doppler anemometer) to evaluate the flow characteristics. Nevertheless, the tests were only carried out on the circular cylinder mounted on the flat plate. With the help of rapid advances in computing technology, this project strongly propose the road to simulate the flow by solving the RANS equations.

4.3.1. CFD simulation

RANS equations are employed to compute the solution around the juncture. Closure to the turbulence is done by continually using the S-A one equation model. A FVM technique is employed to solve the problem numerically. Simulation is performed at two Reynolds numbers of 3,900 and 1,000,000. A great deal of computed data for the 140 flow configurations was computed to cover all the geometric combinations. Moreover, one unsteady simulation is also carried out to depict Karman vortex shedding.

4.3.1.1. Computational domain and boundary condition

The dimensions of the computational domain are similar to the case of the flat plate. The cylinder has the diameter (D) of 0.2m and a depth of $5D$ to incorporate the span-wise effects. Besides, the cylinder is inclined at every 10 degrees, from 0° to 30° laterally, upstream, and downstream. The plate is changed by the different curvatures, includes the concave and convex. The different curvature radii (R) of the plate were considered: $30D$, $40D$, and $50D$ respectively.

The each flow configuration is tested with the longitudinal uniform velocities of 0.0196m/s and 5.019m/s correspond to the Reynolds number of 3,900 and 1,000,000 respectively. In addition, the initial turbulence parameters are also imposed by the turbulence intensity of

4.3658% and 2.1828% with regard to Reynolds number of 3,900 and 1,000,000. With both of these Reynolds numbers, only one length scale of 0.1167m is applied.

4.3.1.2. Meshing

Some techniques of Gambit is used to bend the plate and generate the mesh. A structured hexahedral mesh is employed in these simulations to ensure that the number of cells is still 1,526,760 cells. The y^+ value of 4 around the surface of the cylinder is still chosen. H-O type grids are used for the PDE discretization, i.e. a boundary fitted O-grid around the cylinder and an H-type grid for the surrounding domain.

4.3.1.3. Discretization

In the RANS model of flow around a circular cylinder mounted on the curved plate, the Navier-Stokes equations are discretized using the upwind differencing scheme. The time discretization is carried out by using a second order accuracy scheme.

4.3.1.4. Time step and convergence

In the steady case, at least 8000 iterations are required to ensure the convergence condition and the flow over the cylinder can develop fully. The residuals of convergence of the solutions are maintained at 10^{-5} to keep errors at an acceptable level.

4.3.2. The results and discussions

4.3.2.1. Reynolds number of 3,900

a. The vertical circular cylinder

From the simulation results, a comparative analysis of the influence of the plate curvature on the pressure distribution on the vertical cylinder is suggested. Figure 4.19 shows a comparison between the solutions computed on the vertical circular cylinder mounted on the concave plate. Fig. 4.19a depicts the solution computed on the plate with the curvature radius of 30D, Fig 4.19b presents the solution computed on the plate with the curvature radius of 40D, and on the other hand, Fig. 4.19c refers to the solution computed on the plate with the curvature radius of 50D. The pressure distribution on Fig 4.19 proves that smaller curvatures determine larger pressure, as expected. However, the difference is very small if the pressure in small curvature is compared with that in larger curvature.

Similarly, Figure 4.20 depicts the pressure fields computed on the convex plate case, which is curved at the same radii as the concave plate. Fig. 4.20a bears out the solution computed on the convex plate with the curvature radius of 30D, Fig. 4.20b relates to the solution computed on the convex plate with the curvature radius of 40D, whereas Fig. 4.20c describes the solution computed on the convex plate with the curvature radius of 50D. Once again, the

pressure distribution reveals that smaller curvatures determine larger pressure, a fact that will lead to an increase of the total drag coefficient.

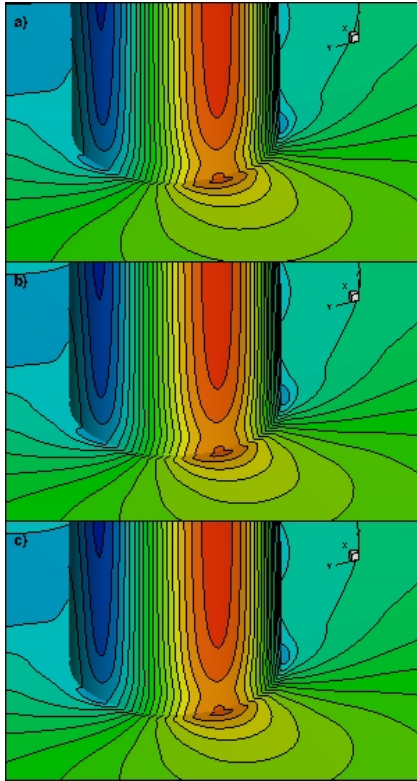


Figure 4.19. Curvature influence on the pressure distribution on a juncture flow in concave plate case

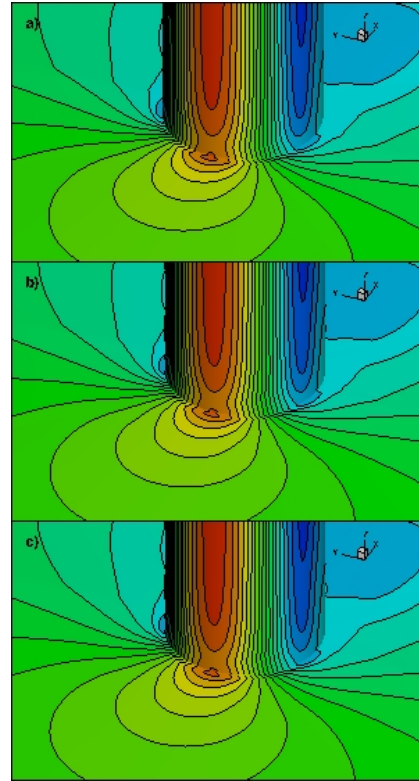


Figure 4.20. Curvature influence on the pressure distribution on a juncture flow in convex plate case

b. The inclined circular cylinder

As above-mentioned, the large adverse pressure gradients induced by the cylinder produce boundary layer separation as well as the horseshoe vortices formation implies an analysis of the flow topology in the immediate proximity of the juncture between the cylinder and plate is necessary. In this respect, Figure 4.21 depicts the transversal streamlines drawn around the juncture. Fig. 4.21a shows the cylinder mounted on a flat plate, whereas Figs. 4.21b and 4.21c describe the paths for the concave and convex plates, respectively. In all cases, the cylinder is inclined by 20° laterally. The cylinder inclination determines a significant change of the particle paths. On the contrary, the plate curvature does not determine a significant change of the transversal streamlines. It is seen that though the plate curvature changes, the configuration of particle lines among flat, concave, and convex plate cases is not different at all. In all cases, there are the occurrence of a weak vortex that develops on the flat and convex plates.

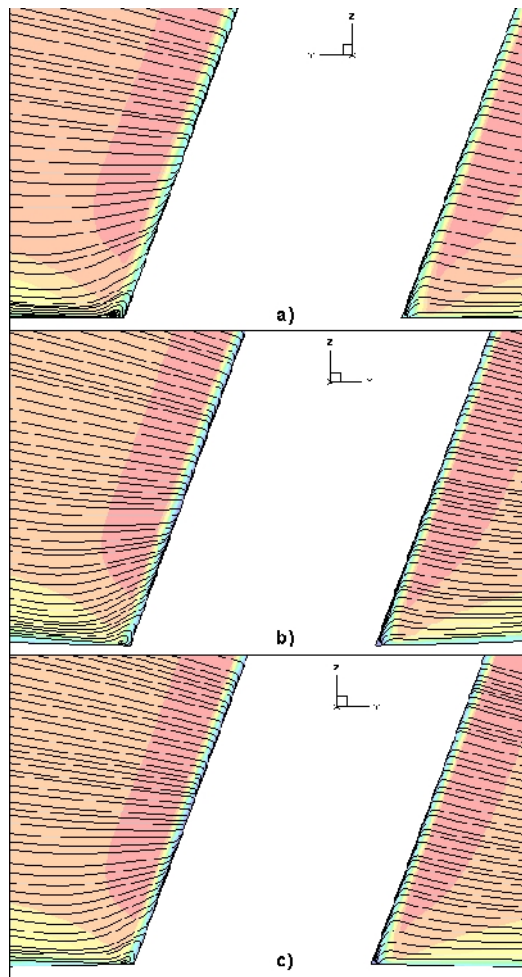


Figure 4.21. Transversal streamlines around the juncture

Figure 4.22 shows the influence of the plate curvature on the total drag coefficient of the cylinder mounted on the concave plate and inclined upstream drawn against the relative inclination angle. All numerical solutions is drawn for the four curvature radii. Figure 4.22 unveils that an about 67% increase of the curvature determines the increase of the total drag coefficient of about 1.2%, mostly caused by the augmentation of the drag on the plate. This conclusion is valid for all the angles between the cylinder and the plate, regardless the direction of the relative inclination. In addition, Fig. 4.22 also reveals that the increase of inclination angle results in a reduction of total drag coefficient. The total drag coefficient is decreased slowly. This comment is correct for all curvature radii, regardless the direction of the relative inclination. The reduction of total drag coefficient may be caused by the decrease of pressure gradients behind the cylinder.

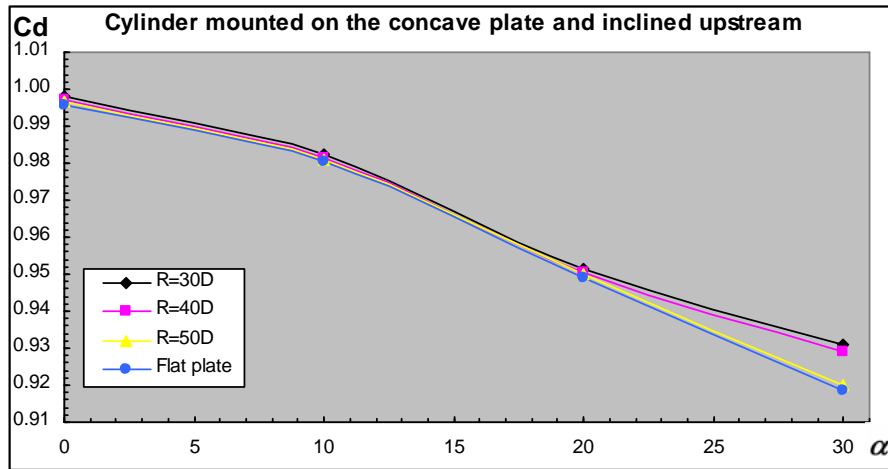


Figure 4.22. Curvature influence on the drag coefficient of the cylinder mounted on the concave plate and inclined upstream

Figure 4.23 describes the modification of the drag coefficient when the plate curvature changes along with the inclination angle. In all simulation cases, the cylinder is mounted on the concave plate and inclined downstream. The total drag coefficient reduces sharply when the inclination angle increases.

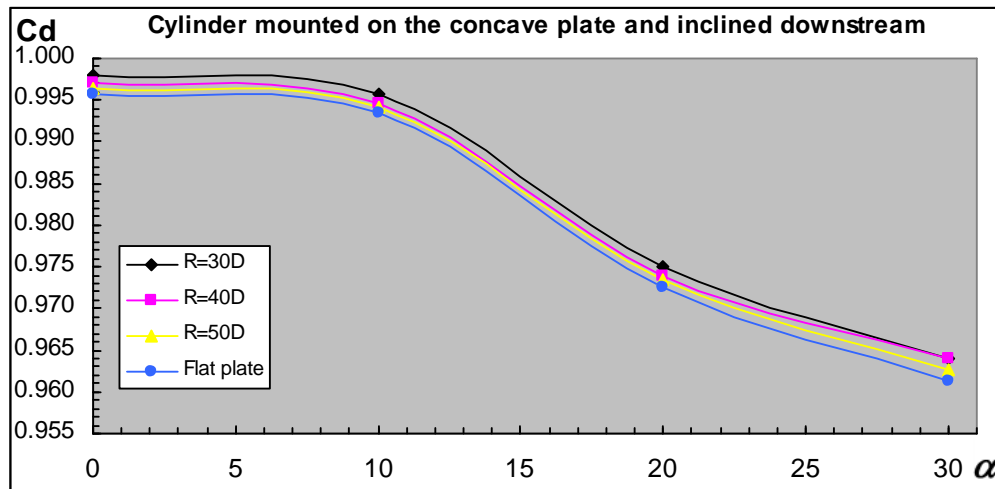


Figure 4.23. Curvature influence on the drag coefficient of the cylinder mounted on the concave plate and inclined downstream

Considering the lateral inclination case, figure 4.24 depicts the influence of plate curvature on the drag coefficient mounted on the concave plate with different inclination angles of 10°, 20°, and 30°, respectively. In these cases, the drag coefficient is reduced when the inclination angle increases. This reduction caused by the augmentation of lift force.

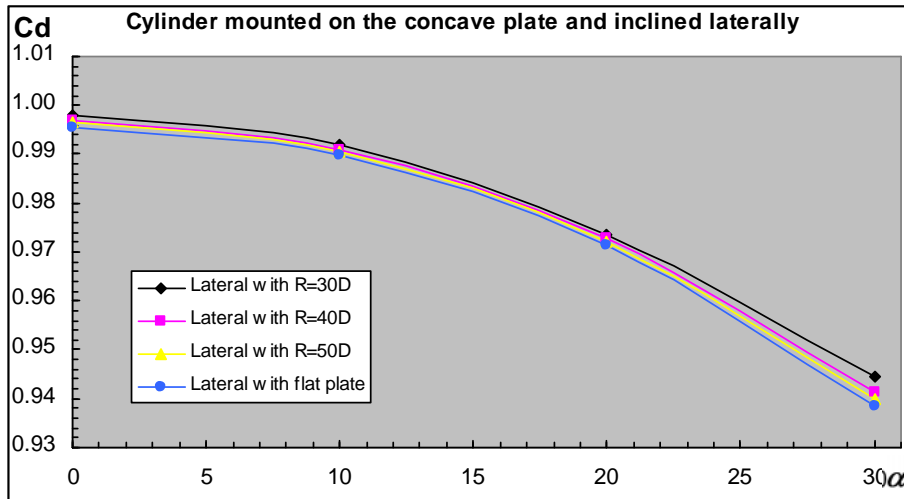


Figure 4.24. Curvature influence on the drag coefficient of the cylinder mounted on the concave plate and inclined laterally

For the convex plate, the influence of plate curvature is presented in Figs. 4.25, 4.26, and 4.27. Fig. 4.15 shows the results computed on the cylinder inclined upstream, Fig. 4.26 expresses the results computed on the cylinder inclined downstream, while Fig. 4.27 plots the results computed on the cylinder inclined laterally.

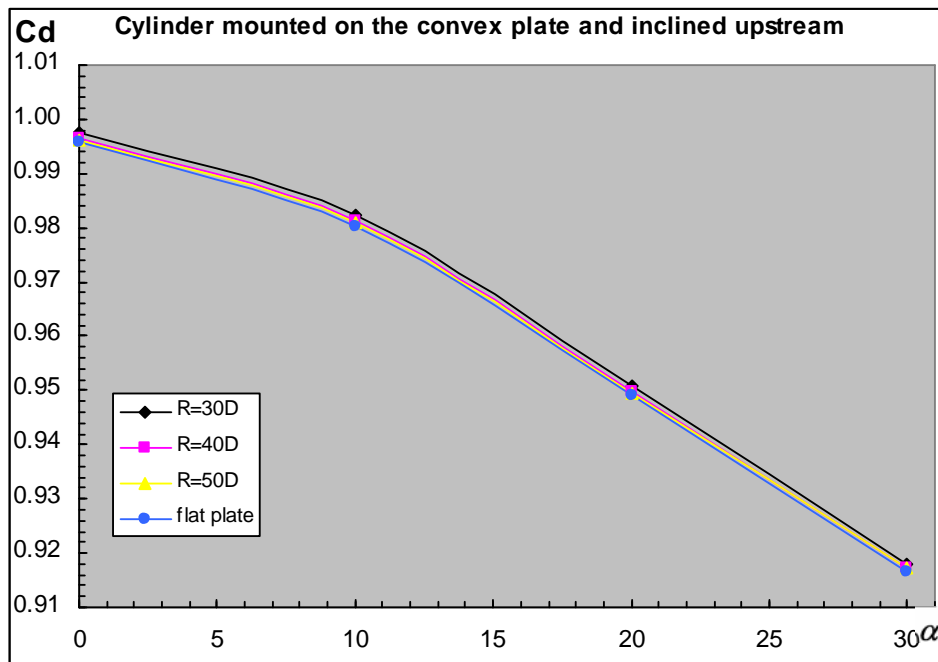


Figure 4.25. Curvature influence on the drag coefficient of the cylinder mounted on the convex plate and inclined upstream

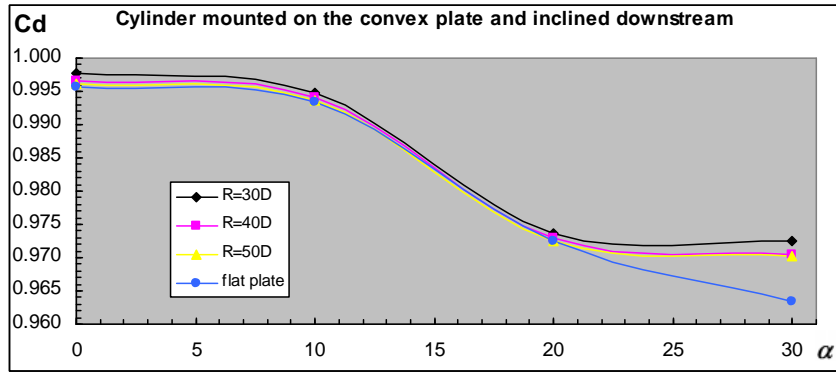


Figure 4.26. Curvature influence on the drag coefficient of the cylinder mounted on the convex plate and inclined downstream

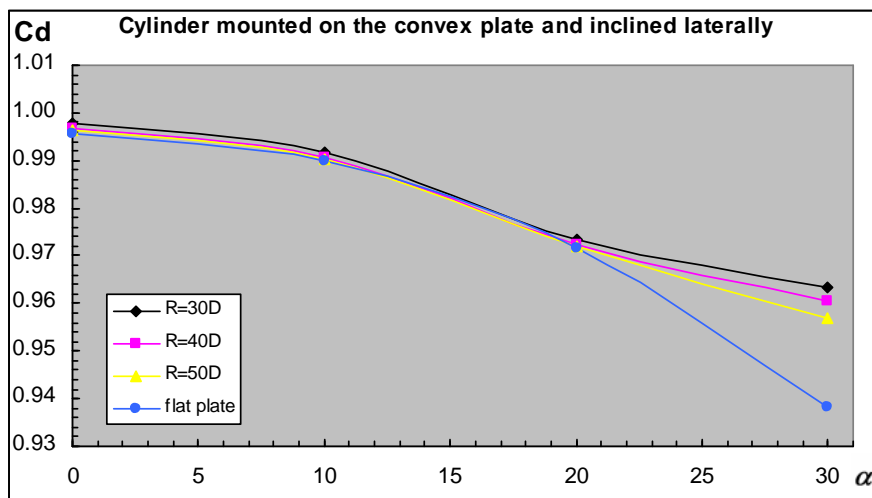


Figure 4.27. Curvature influence on the drag coefficient of the cylinder mounted on the convex plate and inclined laterally

Figure 4.28 shows a comparison between the drag coefficients on the cylinder mounted on the flat plate drawn at four inclination angles. The graphs depict the variation of the total drag coefficient (C_d) as well as of its components produced by pressure (C_{dp}) and by viscosity (C_{dv}) for each angle. It is worth mentioning that the increase of the inclination angle determines the quasi-linear decrease of C_d and C_{dp} regardless the direction of the cylinder inclination. On the contrary, the viscosity components of the drag C_{dv} increase with the angle. The possible reason resulted in this increase is that when the cylinder is inclined, the wetted area of the cylinder will also enlarge; thus, the viscosity fore increase appropriately. Similar comments are valid for the case of the cylinder mounted on a curved plate either concave (Fig. 4.29) or convex (Fig. 4.30).

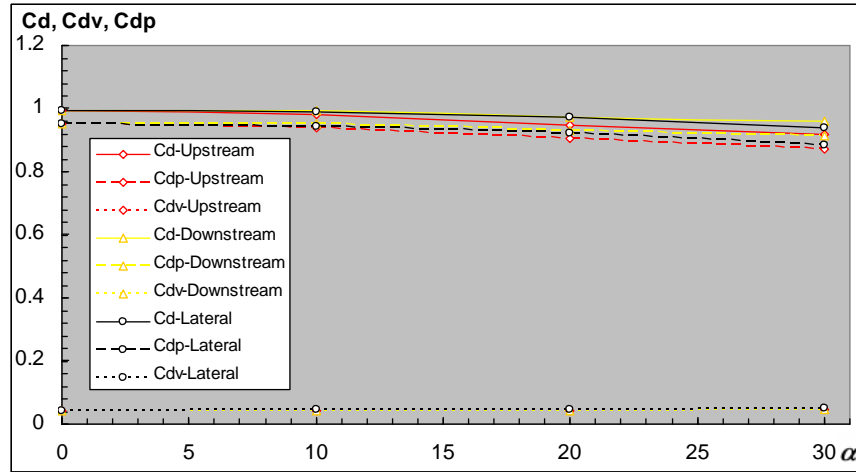


Figure 4.28. Inclination angle influence on the drag coefficient of the cylinder in flat plate case

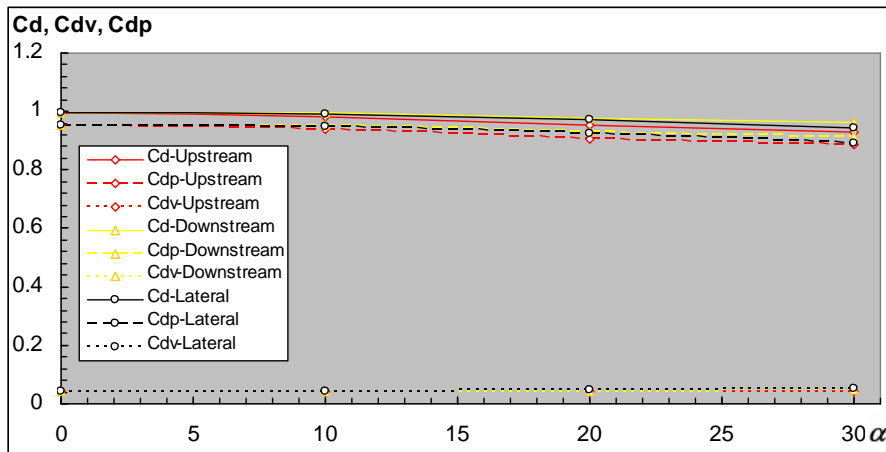


Figure 4.29. Inclination angle influence on the drag coefficient of the cylinder in concave plate case

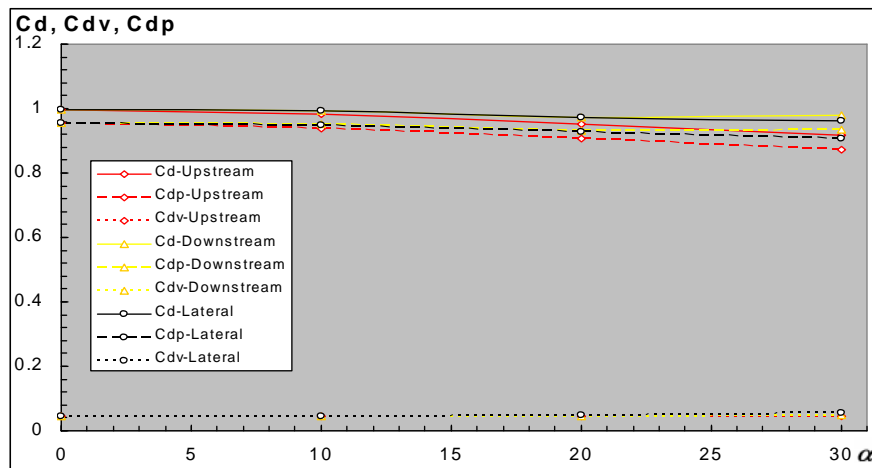


Figure 4.30. Inclination angle influence on the drag coefficient of the cylinder in convex plate case

In terms of the drag computed on the plate only, Figure 4.31 drawn for the flat plate proves that the viscous drag (C_{dv}) decreases almost linearly until the 30° angle in upstream direction. On the other hand, the viscous drag increases almost linearly in downstream direction whereas it keeps constant in lateral direction. Hence, the lateral inclination does not affect the viscous drag of flat plate, but impact so much in upstream and downstream cases. The increase or decrease of viscous drag is probably caused by the horseshoe vortex around the juncture. The coefficient of drag produced by pressure (C_{dp}) is equal to zero in all the computational cases, regardless the cylinder inclination. Although not shown graphically, the behavior is similar for the curved plates as the computations have proven.

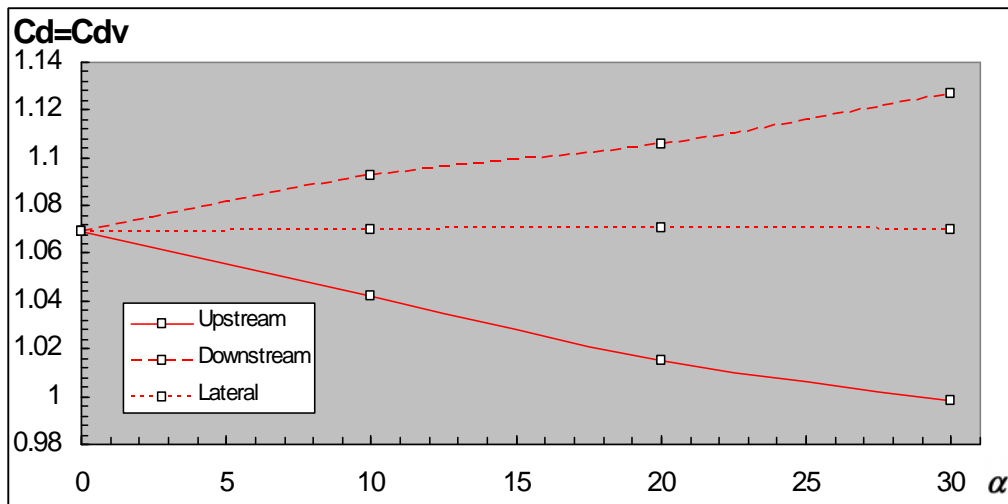


Figure 4.31. Viscous drag coefficient variation with the inclination angle in flat plate case

4.3.1.2. Reynolds number of 1,000,000

a. The vertical circular cylinder

When the Reynolds number increases, the mechanism of flow around the juncture becomes more complicated. All the flow characteristics modify so much, especially, the pressure distribution. Figure 4.32 shows the pressure fields computed on the vertical circular cylinder mounted on the concave plate. The solution computed on the plate with the curvature radius of $30D$ is presented in Fig. 4.32a, the solution computed on the plate with the curvature radius of $40D$ is described in Fig 4.32b, and on the other hand, Fig. 4.32c refers to the solution computed on the plate with the curvature radius of $50D$. The pressure distribution on Fig 4.32 also proves that smaller curvatures determine larger pressure, as the case of $Re=3,900$.

Similarly, Figure 4.33 depicts the pressure fields computed on the convex plate case, which is curved at the same radii as the concave plate. Fig. 4.33a shows the solution computed on the convex plate with the curvature radius of $30D$, Fig. 4.33b relates to the solution computed on

the convex plate with the curvature radius of $40D$, whereas Fig. 4.33c describes the solution computed on the convex plate with the curvature radius of $50D$. Once again, the pressure distribution reveals that smaller curvatures determine larger pressure, a fact that will lead to an increase of the total drag coefficient.

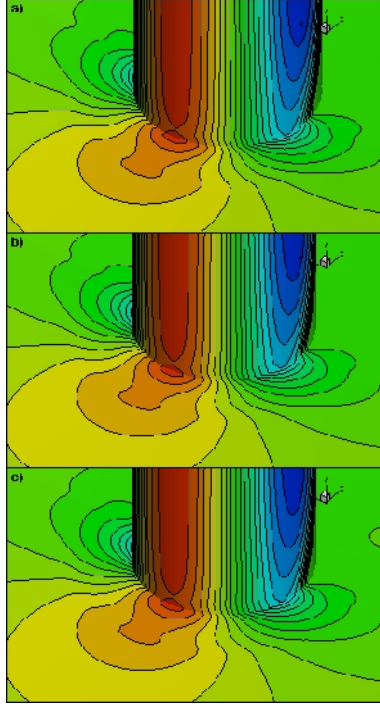


Figure 4.32. Curvature influence on the pressure distribution on a junction flow in concave plate case

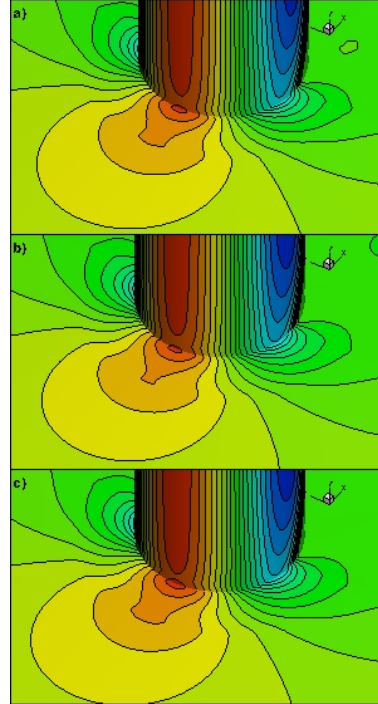


Figure 4.33. Curvature influence on the pressure distribution on a junction flow in convex plate case

b. The inclined circular cylinder

Because of the modification of pressure fields around the juncture, an analysis of the flow topology in the immediate proximity is very necessary. Figure 4.34 depicts the transversal streamlines drawn around the juncture. Fig. 4.34a shows the cylinder mounted on a flat plate, whereas Figs. 4.34b and 4.34c describe the paths for the concave and convex plates, respectively. In all cases, the cylinder is inclined by 20° laterally. Similar to the $Re = 3,900$ cases, Fig. 4.34 proves that the plate curvature does not determine a significant change of the transversal streamlines. It is seen that though the plate curvature changes, the configuration of particle lines among flat, concave, and convex plate cases is not different at all. In all cases, there are the occurrence of a weak vortex that develops on the flat and convex plates. However, there is still the difference compared with Reynolds number of $3,900$. That is that the shape of vortex in front of cylinder becomes larger and more complex. There is one thin boundary layer along the cylinder.

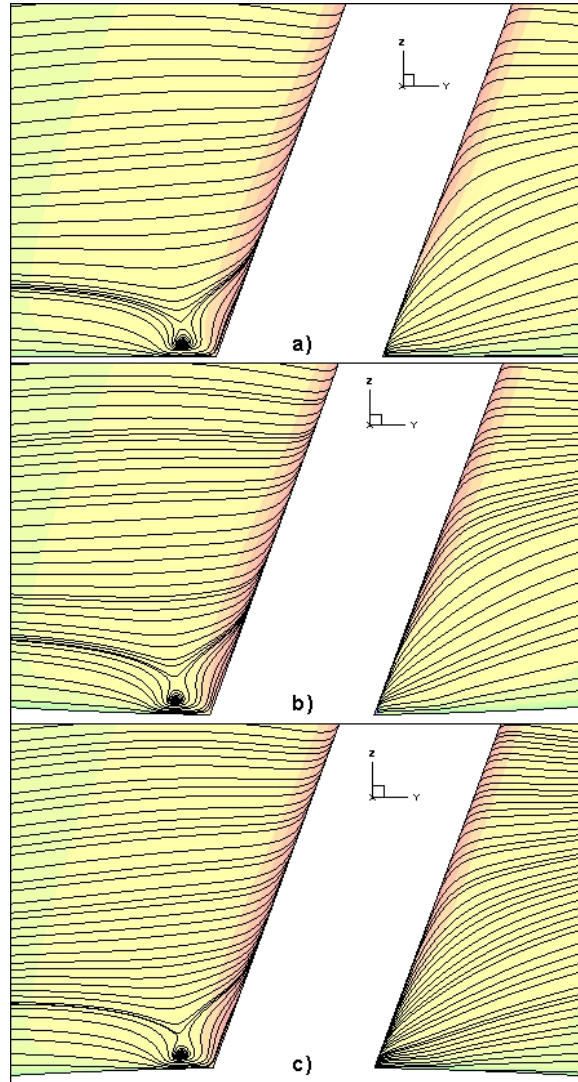


Figure 4.34. Transversal streamlines around the juncture

Figure 4.35 shows the influence of the plate curvature on the total drag coefficient of the cylinder mounted on the concave plate and inclined upstream drawn against the relative inclination angle. All numerical solutions is drawn for the four curvature radii. Figure 4.35 reveals that a 67% increase of the curvature determines the increase of the total drag coefficient of about 0.7%, mostly caused by the augmentation of the drag on the plate. This conclusion is valid for all the angles between the cylinder and the plate, regardless the direction of the relative inclination. In addition, Fig. 4.35 also shows that the increase of inclination angle results in a correspond increase of total drag coefficient. This comment is correct for all curvature radii as well as the convex plate case (Fig. 4.39), regardless the direction of the relative inclination. According to Baban et al. (1989), an increase in drag force fluctuations due to highly recirculation flow in the wake region.

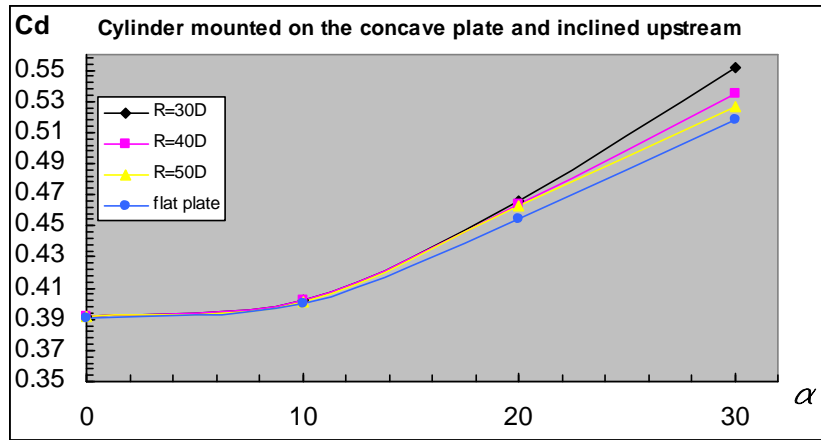


Figure 4.35. Curvature influence on the drag coefficient of the cylinder mounted on the concave plate and inclined upstream

Unlike the upstream case, the influence of plate curvature on the cylinder inclined downstream is slightly different (Fig. 4.36). The total drag coefficient reduces at the 10° angle in each curvature radii then it increases. This comment is valid for the convex plate case (Fig. 4.40). Besides, this difference also reported by Ishima T. et al. (2008). It comes from the modification of the recirculation zone and the separation-reattachment processes. The recirculation zone of the 10° angle is larger than that of 0° angle (Fig. 4.37), thus, its effect is also much more. The existence of adverse velocities acting on the cylinder leads to the reduction of drag coefficient. Otherwise, the large recirculation zone also exists in the 20° and 30° cases. However, the recirculation zone is further from the cylinder and smaller than that in the 10° case. Herein, the influence of this zone in 20° and 30° cases is not as strong as that in 10° case.

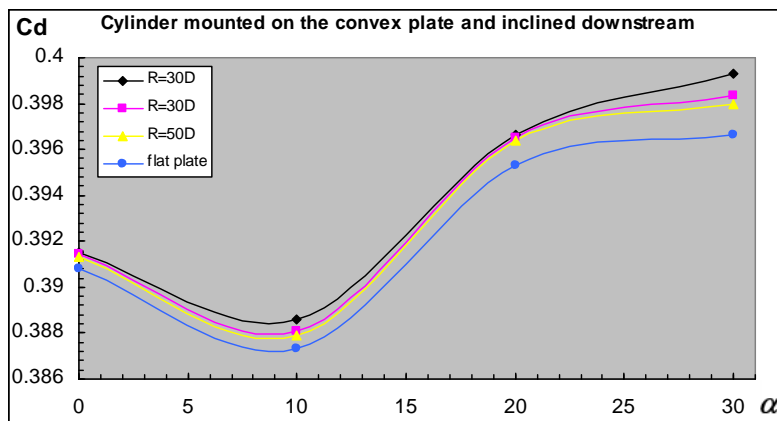


Figure 4.36. Curvature influence on the drag coefficient of the cylinder mounted on the concave plate and inclined downstream

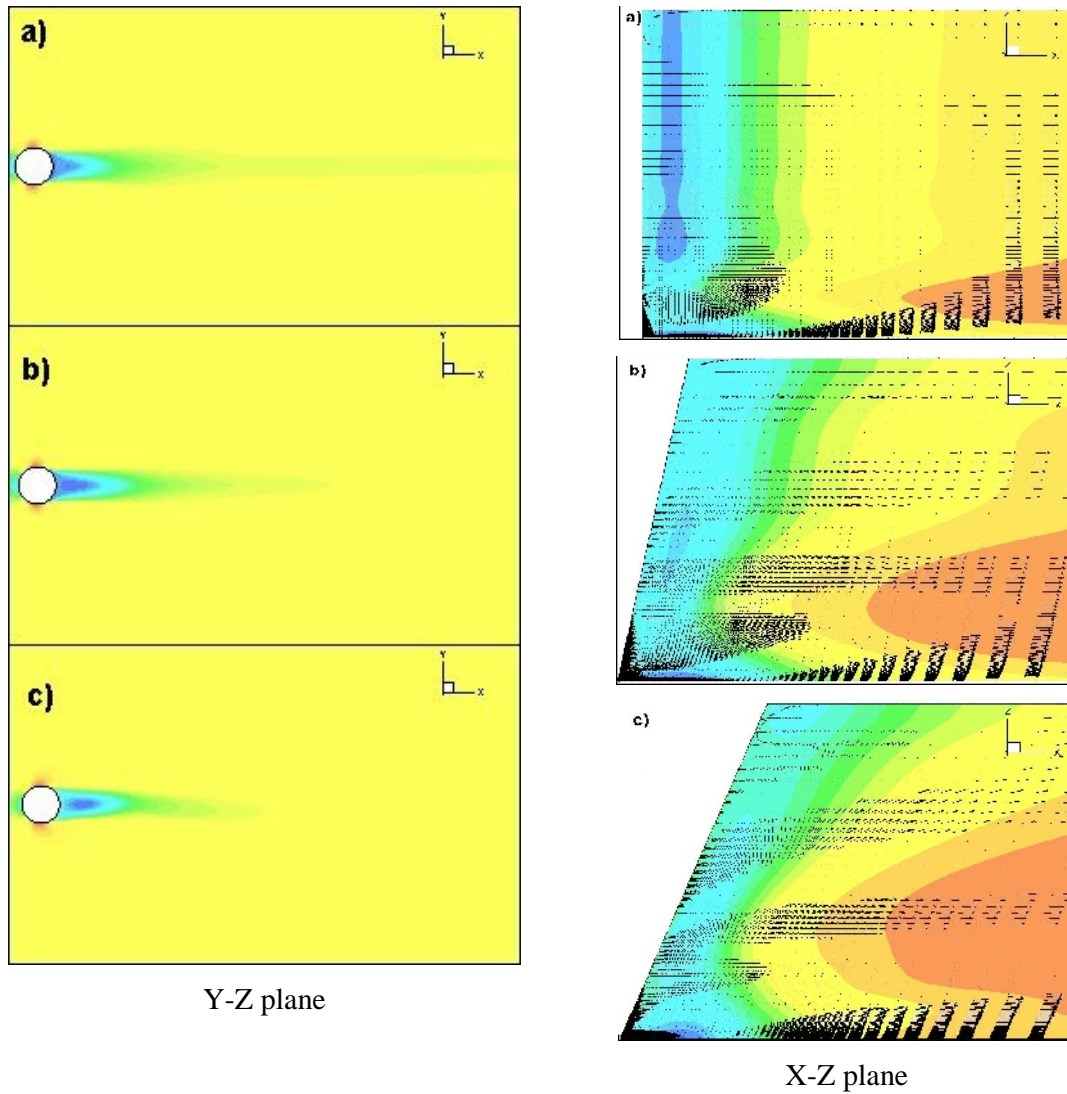


Figure 4.37. Velocity fields

- a) the case of 0° angle
- b) the case of 10° angle
- c) the case of 20° angle

Figure 4.38 depicts the influence of plate curvature on the cylinder inclined laterally in the concave case. The drag slightly increases from 0° angle from 10° then it decreases. This change also appears in the convex plate case (Fig. 4.40). It is seemingly due to the modification of the recirculation zone behind the cylinder.

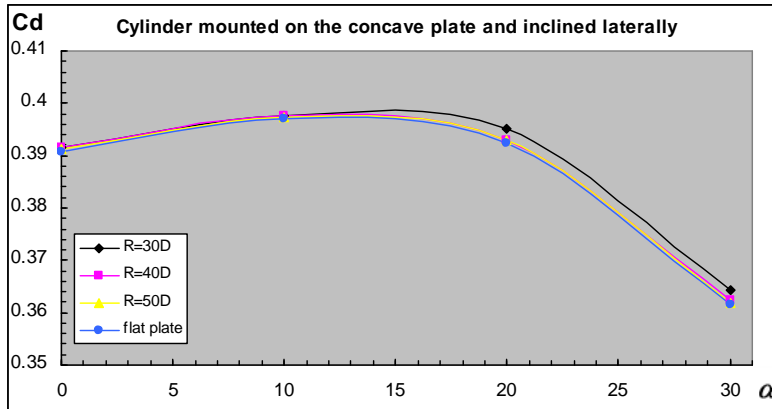


Figure 4.38. Curvature influence on the drag coefficient of the cylinder mounted on the concave plate and inclined laterally

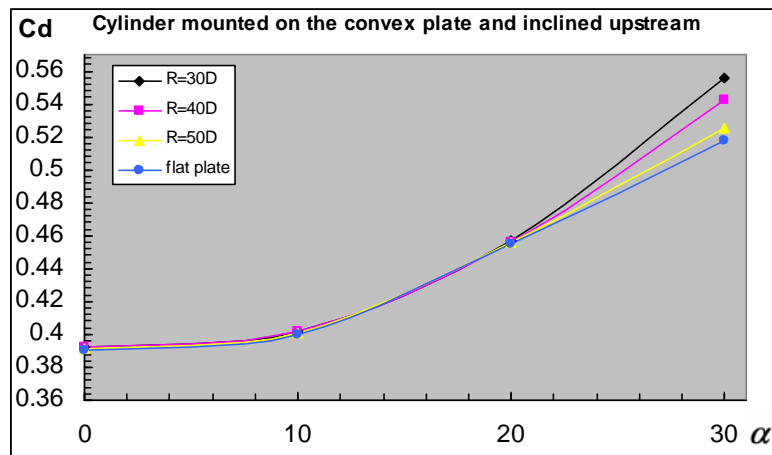


Figure 4.39. Curvature influence on the drag coefficient of the cylinder mounted on the convex plate and inclined upstream

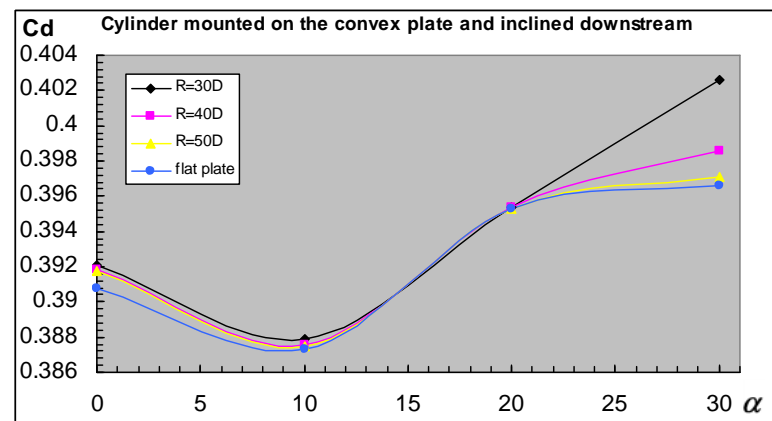


Figure 4.40. Curvature influence on the drag coefficient of the cylinder mounted on the convex plate and inclined downstream

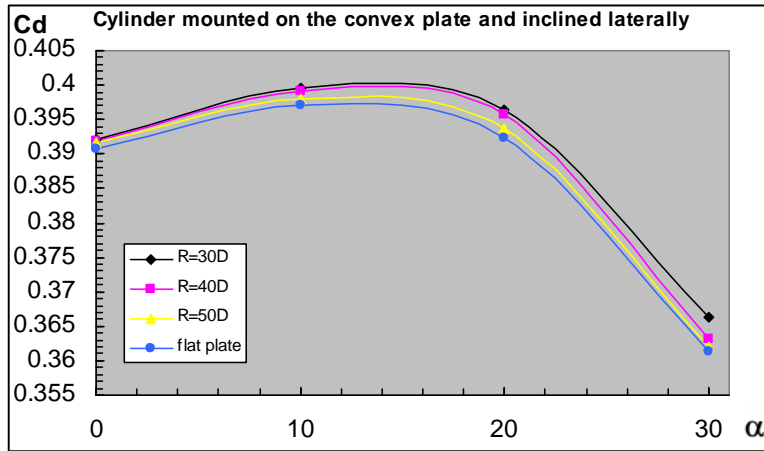


Figure 4.41. Curvature influence on the drag coefficient of the cylinder mounted on the convex plate and inclined laterally

Figure 4.42 shows a comparison between the drag coefficients on the cylinder mounted on the flat plate drawn at four inclination angles. The graphs depict the variation of the total drag coefficient (C_d) as well as of its components produced by pressure (C_{dp}) and by viscosity (C_{dv}) for each angle. It also reveals that the increase of the inclination angle determines the quasi-linear decrease of C_d and C_{dp} in upstream case regardless the direction of the cylinder inclination, whereas the viscosity component of the drag C_{dv} seems constantly with the every angle. On the other hand, the C_d and C_{dp} in lateral and downstream cases slightly decrease when the inclination angle increases. Similar comments are valid for the case of the cylinder mounted on a curved plate either concave (Fig. 4.43) or convex (Fig. 4.44).

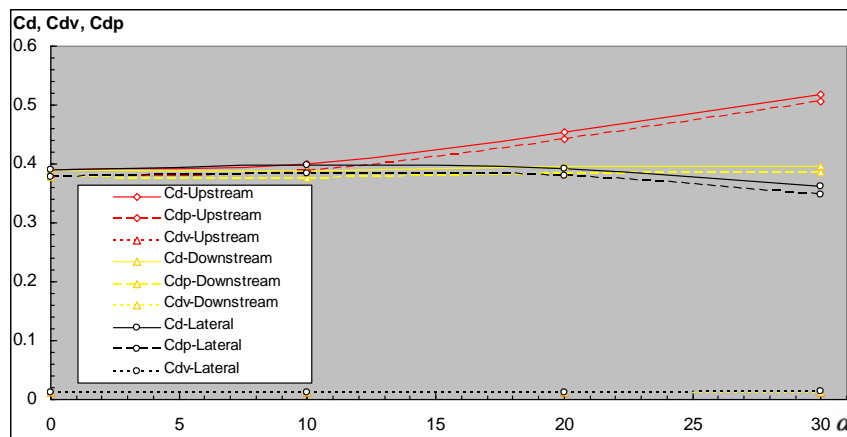


Figure 4.42. Inclination angle influence on the drag coefficient of the cylinder in flat plate case

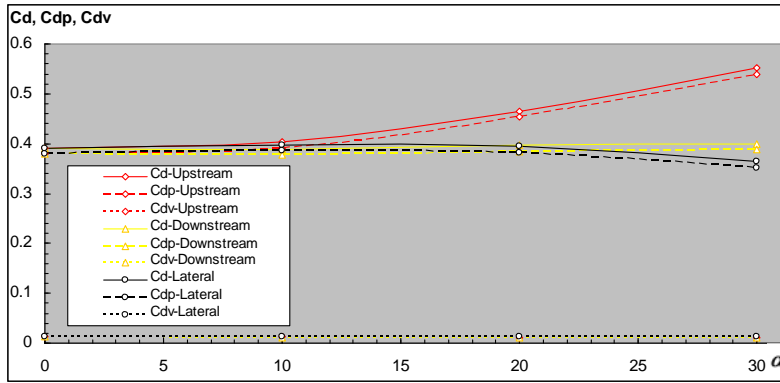


Figure 4.43. Inclination angle influence on the drag coefficient of the cylinder in concave plate case

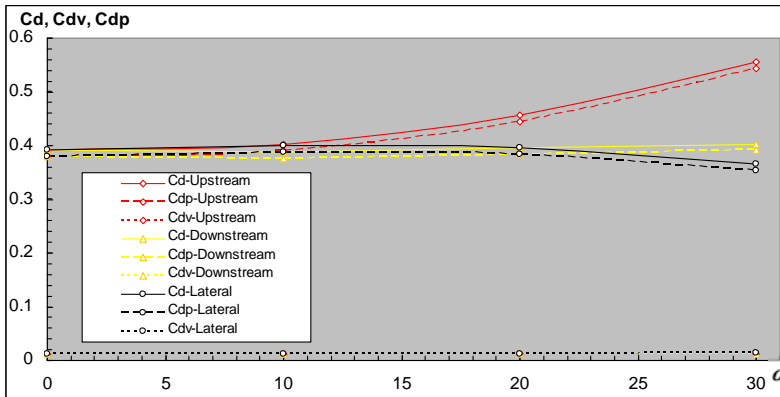


Figure 4.44. Inclination angle influence on the drag coefficient of the cylinder in convex plate case

Figure 4.45 depicts the drag computed on the flat plate only. It is easily seen that the viscous drag coefficient (C_{dv}) decreases in upstream case and increases in downstream and lateral cases. The coefficient of drag produced by pressure (C_{dp}) is equal to zero in all the computational cases, regardless the cylinder inclination.

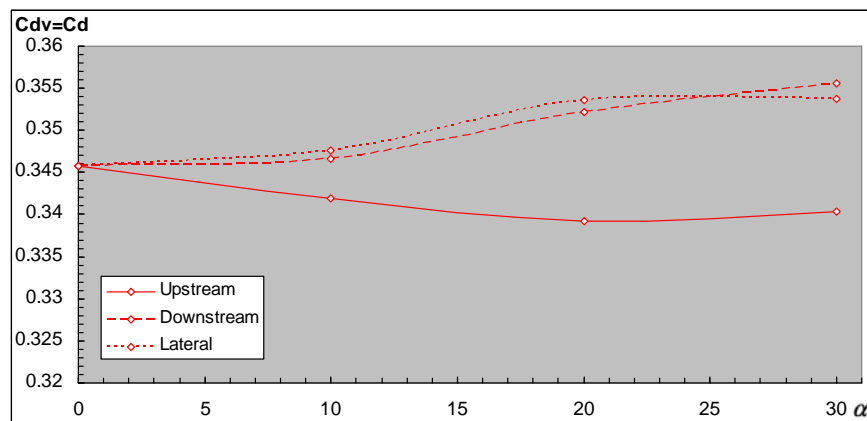


Figure 4.45. Viscous drag coefficient variation with the inclination angle in flat plate case

4.4. Conclusion

Investigation of the flow around the circular cylinder began with the comparisons of the drag coefficient of the vertical cylinder mounted flat plate with relative inclination angle. Details on the streamlines have been compared with experimental data in the vicinity around the cylinder at Reynolds number of 3,900.

Next, all the simulated results from the curved plate at both Reynolds numbers of 3,900 and 1,000,000 are presented, compared, and plotted. The change of drag coefficients at $Re = 3,900$ is different from that at $Re = 1,000,000$. At $Re = 3,900$ in sub-critical region, all drag coefficients decrease, whereas at $Re = 1,000,000$ in critical region, most of drag coefficients increases, apart from the case of 10° in downstream. It maybe caused by the separation and attachment processes. In addition, the detailed modification of flow characteristics that takes into account the cylinder inclination and plate curvature is described. Hence, the nature as well as the juncture flow around the cylinder mounted on the curved plate also reveals.

5. UNSTEADY NUMERICAL SIMULATION

5.1. Introduction

This chapter presents 3-D numerical solutions of unsteady incompressible turbulent flow around the circular cylinder inclined laterally with an angle of 30° and mounted on the curved plate. The curved plate has the convex curvature of $50D$. This simulation is performed by using the FLUENT simulation package to solve the unsteady Navier-Stokes equations. The Reynolds number used is 3,900.

5.2. 3-D computational domain and boundary conditions

The downstream domain extended $35R$ behind the model to capture vortex shedding in the wake region, and for upstream boundary is located at $15R$. The lateral boundaries determined far from the centerline through the cylinder is $25R$. The cylinder has the depth of $10R$ to incorporate the span-wise effect.

The boundaries of the computational domain were set at sufficiently remote distance from the model to ensure satisfaction of inlet and outlet conditions. The inlet boundary condition on the computational domain is *Velocity-Inlet*, and in all cases, the speed is set at $0.0196m/s$. The outlet boundary condition is *Pressure-Outlet*, and in all cases, this is set at a pressure of 101325 kPa. The top and lateral faces of the computational domain are set to be symmetric, since the simulated model is symmetric. Finally, the bottom face and the cylinder are set up to wall boundary conditions.

5.3. 3-D mesh

In this work, a structural hexahedral mesh is employed. The grid used for this simulation is shown in Figure 5.1. In the boundary layer around the cylinder, the first cell height is 0.0001m and growth factor does not exceed 1.1.

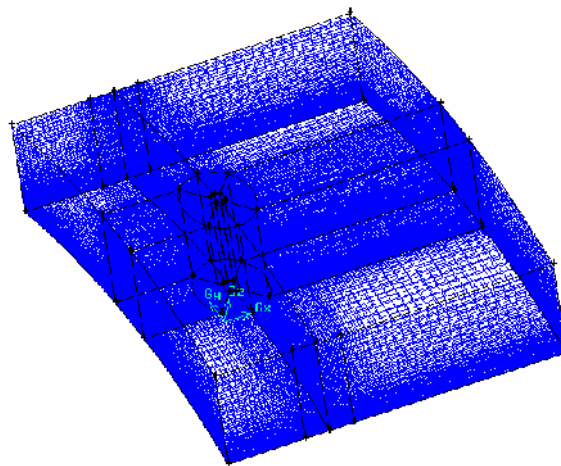


Figure 5.1. Mesh domain

5.4. Modeling turbulent flow

After meshing the geometry in GAMBIT the meshed file was exported to FLUENT and ready to be simulated. FLUENT is implicitly simulating the phenomenon by giving an option for transitional flows correcting when S-A is used as a turbulent flow model. Recent research on a circular cylinder simulation showed different approached different turbulence models. In the S-A model, the Turbulence kinetic intensity I is given by the equation of 3.3 and the length scale l is given by the equation of 3.5. By the calculation, the value of I is 4.3658% and of l is 0.1167m.

According to Huner B. et al. (1977), the time step (Δt) was chose to be small enough to account for the smallest cell in the computational domain as follows:

$$\Delta t = \frac{\text{Typical cell size}}{\text{velocity}} = 0,005\text{s}$$

The residuum of convergence of the solution is always maintained at 10^{-6} to ensure that the errors can be acceptable. The number of time steps in the simulation is 50,000 time steps, which has been found to be enough for the flow to develop completely.

5.5. Simulation results and discussions

5.5.1. Flow field

Figure 5.2 shows comparisons of the flows at different relative times: 5s, 50s, 100s, 150s, 200s and 500s. It is seen that the high velocities appears two sides of cylinder, but, the highest velocity reveals on the side which the cylinder inclined. The symmetry of velocity disappears due to the movement of the stagnation point. The lower velocity region is behind the cylinder. The vortices spread in downstream and interact with the downstream flow. After $t = 200\text{s}$, the shape of vortex shedding is stable, the change of velocity is not so much.

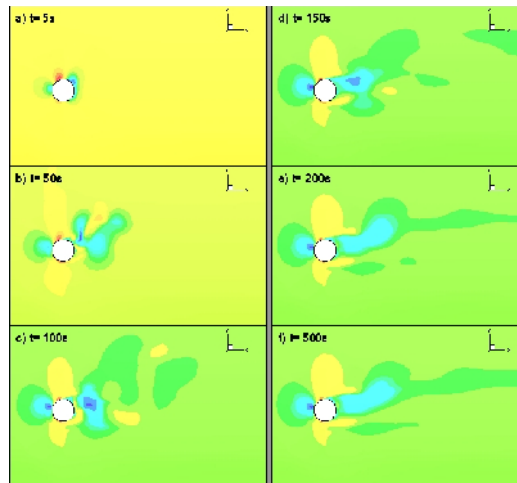


Figure 5.2. Comparison of velocity contours at different flow time

In addition to the modification of velocity field, the pressure field is also changed due to the inclination of the cylinder, as shown in Figure 5.3. The symmetry of the solution vanishes when the stagnation point moves in the side, which the cylinder inclined. In addition, the stronger pressure gradients are observed in the same side.

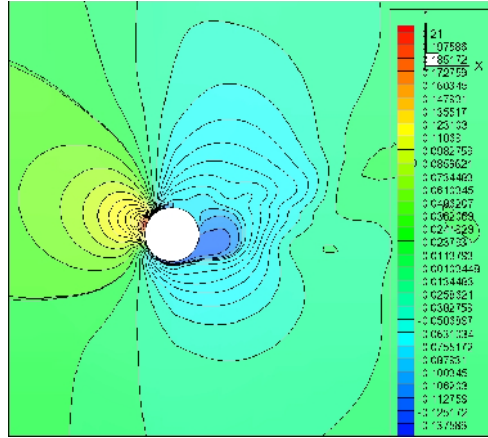


Figure 5.3. The pressure field around the cylinder

Figure 5.4 presents the flow topology around the cylinder. There are two main vortices that generates the vortex shedding behind the cylinder. The first smaller vortex is located near to the cylinder. This vortex will moves towards the downstream and coalesce to form larger-scale vortex right behind of the first vortex. Then, the larger-scale vortex interact with the downstream flow and vanishes. This process repeated following the time results in the vortex shedding.

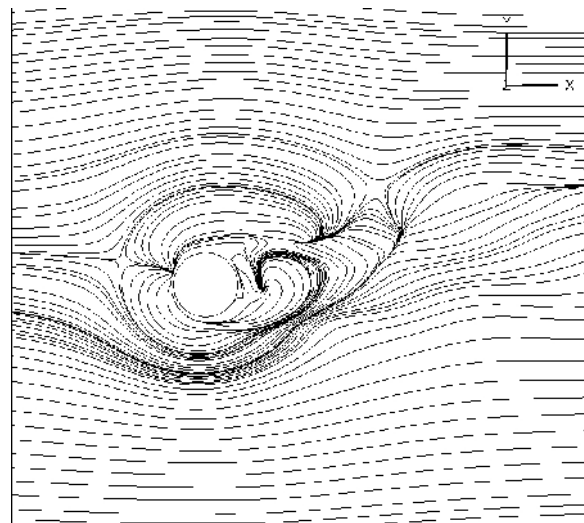


Figure 5.4. The flow topology around the cylinder at $Re = 3,900$

Figure 5.5 depicts close-up of the flow around the cylinder. It also reveals the movement direction of the flow past the cylinder.

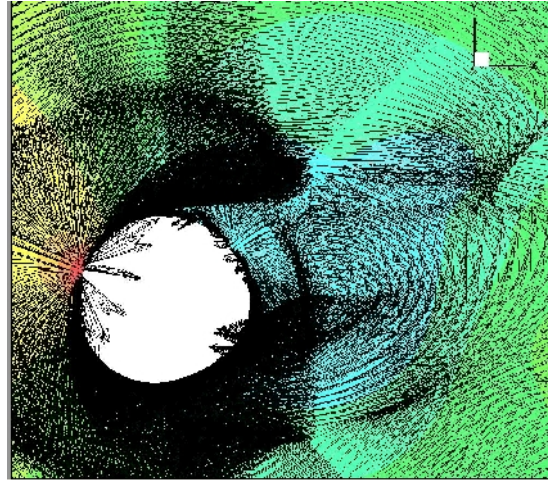


Figure 5.5. The velocity vectors existing near the cylinder

5.5.2. Drag coefficients

Throughout the numerical simulation, different parameters of interest were monitored and recorded, the result of drag coefficients are tabulated in Table 5.1. The unsteady simulation shows that the total drag coefficient of the cylinder is reduced comparing with the steady simulation.

Table 5.1. The total drag coefficients

	Unsteady	Steady
Drag coefficient of the cylinder	0.95035344	0.956929
Drag coefficient of the plate	1.0544992	1.115424

Figure 5.6 and 5.7 show respectively the drag and lift as a function of time. With the drag coefficient plot, additional to reduction of the mean value, fluctuation in the drag is slightly reduced. On the other hand, the mean value does not change, but the fluctuation in the lift is sharply increased. The variation becomes large.

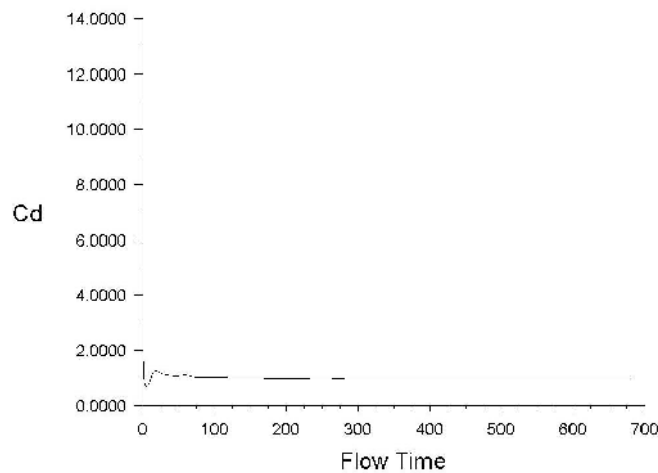


Figure 5.6. Drag coefficient

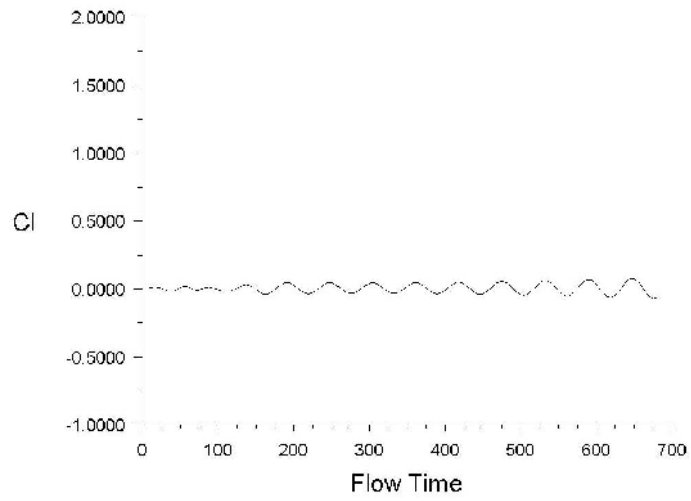


Figure 5.7. Lift coefficient

6. FINAL CONCLUSIONS AND FUTURE WORK

This work done in this thesis has validated the application of S-A turbulence model on the flow around a circular cylinder through comparison study with experimental results. The study equips the author with proper modeling skills for the simulation of flow around the inclined cylinder mounted on the curved plate. The following concludes the findings and achievements on the study of the flow around the circular cylinder, with some suggestions and recommendations on the future work upon the completion of the thesis.

6.1. Final conclusions and remarks

The work conducted in this research in very subject orientated in achieving the aim and objectives of the thesis. By the effort in studying some CFD solvers, modeling the problem, analyzing the results and doing post-processing, some main conclusions have been drawn as follows:

- Generation of a suitable mesh is the most time-consuming stage of the numerical simulation. From the study of physical phenomena of the problem, the computational domain is discretized by using GAMBIT. Depending on the each problem, there are many ways generating the grid. Before meshing, the aspect ratio and the thickness of boundary layer must be paid attention carefully. They are main factors which affect the quality of mesh very much. However, the most difficult is that how to choose the best and the most appropriate mesh. To do that, only comparison with the experimental data is reliable. The simple simulation should be chosen to compare. From modeling the juncture flow, the time spent for mesh generation may go to approximately 60%-70% of the total simulation time.
- Along with choosing the grid, the turbulence model can be chosen at the same time to save computational time and effort. Even though, there are a lot of comments as well as suggestions about selecting the model, they are not correct for all cases. For this work, the S-A turbulence model is the most appropriate model. Thus, it is used to investigate and simulate all cases from the flat plate case to the curved plate case.
- The direction of cylinder inclination affects the juncture flow so much. It causes the modification of flow mechanism such as the change of vortex structure including the horseshoe vortex and Karman vortex, of pressure velocity distribution and the hydrodynamic force magnitude. The stronger pressure gradients at the root of the cylinder inclined longitudinally towards to upstream. For lateral inclination, the symmetry of pressure field vanishes when the stagnation point moves on the side, which the cylinder

inclined. Additionally, the stronger pressure gradients are observed in the same side. These comments are valid for both of Reynolds numbers of 3,900 and 1,000,000.

- If taking into account the plate curvature accompanied with the cylinder inclination, the pressure fields and the forces acting on the cylinder change strongly. The smaller curvatures determine the larger pressure. This leads to an increase of the total drag coefficient. An about 67% increase of the curvature determines the increase of the total drag coefficient of about 1.2% at Reynolds number of 3,900 and 0.7% at Reynolds number of 1,000,000.
- Furthermore, at Reynolds number of 3,900, the total drag coefficients decrease when the inclination angle of cylinder increases, regardless the direction of the cylinder inclination as well as the plate curvature. On the contrary, at Reynolds number of 1,000,000, the total drag coefficient mostly increases along with the increase of cylinder inclination angle in upstream and downstream cases, except for the case of 10° angle in downstream for all convex and concave cases. It seemingly caused by the modification of recirculation zone behind the cylinder.
- The pressure fluctuations on the appendage are the result of several mechanisms, including normal turbulent fluctuations, interactions between horseshoe vortices, and upstream and downstream separations and reattachments.

6.2. Future work

In this section, some recommendations for further research on the work performed on this thesis are listed as follows.

- i. Carrying out the experiments with the circular cylinder mounted on the curved plate
 - The experiments are necessarily performed not only to validate the results of numerical simulation, but also to apply many cases in practice. Until now, there are many experiments carried out with the flat plate and the vertical cylinder or the inclined cylinder. However, no test has been performed so far for the curved plate. Although these experiments may require much time and special experimental devices, they are very significant to understand the juncture flow completely.
- ii. The simulation of free surface
 - All the simulation cases in this work are done without taking into account the effect of free surface. There are some remain questions. How does the juncture flow behave under the free surface condition? How do the characteristics of juncture flow change due to free surface? To answer those questions, the simulation of free surface is very

useful and necessary. Sadathosseini S. H. et al. (2008) was successful in the simulation of free surface waves and wave induced separation. The main goal of his simulation is to investigate the shape effects on the wave-induced separation when compared with the hydrofoil. However, only vertical circular cylinder in fluid was simulated, but not taking into account the effect of juncture. The Volume of Fluid method will be used to simulate the influence of free surface. That means this method will solve RANS equations simultaneously for both fluid and air. The circular cylinder mounted the different shape of plate is also used to make the wave induced separation and vortices.

7. ACKNOWLEDGEMENTS

This thesis was developed in the frame of the European Master Course in “Integrated Advanced Ship Design” named “EMSHIP” for “European Education in Advanced Ship Design”, Ref.: 159652-1-2009-1-BE-ERA MUNDUS-EMMC.

I would like to express my deep sincere appreciation to my supervisor, Professor Adrian Lungu, for his support. I really appreciated guidance, patience, and encouragement that he gave me. Knowledge which he transferred to me is useful not only for completing this thesis in the best way but also for my future.

Thank you to everyone who contributed to the project with their time and effort: Mr. Costel Ungureanu for his help and advice in making the master study such a rewarding experience, Professor Dan Obreja and Mr. Florin Pacuracu for their help with some of the experiments in towing tank during my Internship, Professor Lionel Gentaz and David Le Touze for their knowledge on CFD and their useful advice, Professor Philippe Rigo for the opportunity to study and open my vision, and especially Ms. Audrey Mellote for all her assistance.

My gratitude also goes to my best colleagues Krzysztof Patalong and Darie Bogdan for their useful discussions and support during the study and research period.

Finally, I want to dedicate this work to my parents who supported me in every possible way and to my girlfriend, Trang, for her endless patience, support and love when most required.

8. REFERENCES

- [1] **Achenbach E.**, *Distribution of local pressure and skin friction around a circular cylinder in cross-flow up to $Re = 5.10^6$* , Journal of Fluids Mechanics, 1968, Vol. 34.
- [2] **Achenbach E.**, *Influence of surface roughness on the cross-flow around a circular cylinder*, J. Fluid Mech. 46, 321-335, 1971.
- [3] **Ahmed F and Rajaratnam N**, *Flows around bridge piers*, J Hyd Eng 124(3):288-300, 1998.
- [4] **Anagnostopoulos P., Minear R.**, *Blockage effect of oscillatory flow past a fixed cylinder*, Applied Ocean Research 26, 147-153, 2004.
- [5] **Andrew Sleigh**, *An introduction to Fluid Mechanics*, University of Leeds, 2001.
- [6] **Anderson Jr.**, *Computational Fluid Dynamics: The basics with applications*, McGraw Hill, 1995.
- [7] **Baker C. J.**, *The laminar horseshoe vortex*, Journal of Fluid Mechanics, 1979.
- [8] **Ballio F., Guadagnini A., Malavasi S.**, *Stresses due to a horseshoe vortex at a surface-cylinder intersection*, 1998.
- [9] **Bearman P. W., Graham J. M. R., Naylor P. & Obasaju E. D.**, *The role of vortices in oscillatory flow about bluff cylinders*, In Proc. Intl Symp. on Hydrodyn. in Ocean Engng, Trondheim, Norway (ed. K. M. Gisvold et al.). Norwegian Hydrodynamic Laboratories, Norwegian Institute of Technology, 1981.
- [10] **Bengt Fornberg**, *Steady Viscous Flow past a circular cylinder up to Reynolds number 600*, Journal of computational physics, 1985.
- [11] **Berger E. & Wille R.**, *Periodic flow phenomena*, Ann. Rev. Fluid Mech. 4, 313-340, 1972.
- [12] **Besir Sahin, N. Adil Ozturk, Huseyin Akilli**, *Horseshoe vortex system in the vicinity of the vertical cylinder mounted on a flat plate*, Flow measurement and Instrumentation, 2007.
- [13] **Blackburn H. M. and Schmidt S.**, *Large eddy Simulation of flow past a circular cylinder*, 14th Australasian Fluid mechanics conference, 2001.
- [14] **Blazek J.**, *Computational Fluid Dynamics: Principles and Applications*, Elsevier, 2001.
- [15] **Bloor M.S.**, *The transition to turbulence in the wake of a circular cylinder*, J. Fluid Mech. 19, 290-304, 1964.
- [16] **Bouard R. & Countanceau M.**, *The early stage of development of the wake behind an impulsively started cylinder for $40 < Re < 10^4$* , J. Fluid Mech, 583-607, 1980.

- [17] **Braza M, Chassaing P, Ha Minh H**, *Prediction of large scales transition features in the wake of a circular cylinder*, Phys. Fluids, 1990, Vol.A2, p. 1461-1471.
- [18] **Britter R. E., Hunt J. C. R. and Mumford J. C.**, *The distortion of turbulence by a circular cylinder*, Journal of Fluid Mechanics, 1979.
- [19] **Cantwell B. & Coles D.**, *An experimental study of entrainment and transport in the turbulent near wake of a circular cylinder*, J. Fluid Mech. 136, 321-374, 1983.
- [20] **Cheol Woo Park, Sang Joon Lee**, *Free end effects on the near wake flow structure behind a finite circular cylinder*, Department of mechanical engineering, Pohang University of Science and technology, South Korea, 2000.
- [21] **Chou JH, Chao SY**, *Branching of a horseshoe vortex around surface-mounted rectangular cylinders*, Exp Fluids 28:394-402, 2000.
- [22] **Costel Ungureanu, Adrian Lungu**, *Numerical simulation of the turbulent flow around a strut mounted on a Plate*, University of Galati, Romania, 2009.
- [23] **Costel Ungureanu, Adrian Lungu**, *Numerical study of a 3D Junture flow*, University of Galati, Romania, 2008.
- [24] **David Le Touze**, *Introduction to the simulation of turbulence*, Fluid Mechanics Laboratory, Ecole centrale Nantes, 2011.
- [25] **Delaney N.K. & Sorensen N.E**, *Low speed drag of cylinders of various shapes*, NACA Tech. Note 3038, 1953.
- [26] **Devenport W. J., Simpson R. L., Dewitz M. B., Agarwal N. K.**, *Effects of a leading-edge fillet on the flow past an appendage-body junction*, AIAA J 30(9):2177-2183, 1992.
- [27] **Devenport W. J., Simpson R. L.**, *Time-dependent and time-averaged turbulence structure near the nose of a wing-body junction*, J Fluid Mech 210:23-55, 1990.
- [28] **Dillion-Gibbons C.J., Wong C.Y., Chen L. and Soria J.**, *Cylinder wake-boundary layer interaction in the near field*, Laboratory for Turbulent Reseach in Aerospace and combustion Monash University, Australia, 2007.
- [29] **Ferziger Joel H., Milovan Peric**, *Computational Methods for Fluid Dynamics*, Third Edition, Springer, 2002.
- [30] **Gokhan Kirkil, George Constantinescu and Robert Ettema**, *The horseshoe vortex system around a circular bridge pier on a flat bed*, Stanley Hydraulics Laboratory, The University of Iowa, USA.
- [31] **Ishima T., Sasaki T., Gokan Y., Takahashi Y., Obokata T.**, *Flow characteristics around and inclined circular cylinder with fin*, 14th Int Symp on Applications of laser techniques to Fluid mechanics, Lisbon, Portugal, 2008.

- [32] **Jiang Chun Bo, Du Li Hui and Liang Dong Fang**, *Study of concentration fields in turbulent wake regions*, Journal of Hydraulic research, 2003, Vol. 41.
- [33] **Jiyuan Tu, Guan Heng Yeoh, Chaoqun Liu**, *Computational Fluid Dynamics: A Practical Approach*, Butterworth-Heinemann, 2008.
- [34] **Jurij Sodja**, *Turbulence models in CFD*, University of Ljubljana, Slovenia, 2007.
- [35] **Kai Fan Liaw**, *Simulation of flow around Bluff bodies and bridge deck sections using CFD*, PhD thesis, University of Nottingham, England, 2005.
- [36] **Konstantinos Marakkos and John T. Turner**, *Vortex generation in the cross-flow around a cylinder attached to an end-wall*, Optics and laser technology, 2005.
- [37] **Kovaszny L.S.G.**, *Hot wire investigation of the wake behind cylinders at low Reynolds numbers*, Proc. Roy. Soc. A 198, 174-190, 1949.
- [38] **Krajnovic S. and Davidson L.**, *Flow around a three dimensional bluff body*, 9th international symposium on flow visualization, 2000.
- [39] **Lionel Gentaz**, *CFD for Ship hydrodynamics*, Fluid Mechanics Laboratory, Ecole centrale Nantes, 2011.
- [40] **Lourenco L. M. & Shih C.**, *Characteristics of the Plane Turbulent Near Wake of a Circular Cylinder. A Particle Image Velocimetry Study*, (data taken from Beaudan & Moin 1994).
- [41] **Martinuzzi R, Tropea C**, *The flow around surface-mounted, prismatic obstacles placed in a fully developed channel flow*, J Fluids Eng 115:85-92, 1993.
- [42] **Meng Wang, Pietro Catalano and Gianluca Iaccarino**, *Prediction of high Reynolds number flow over a circular cylinder using LES with wall modeling*, Annual Research Briefs, 2001.
- [43] **Meng Wang, Pietro Catalano, Gianluca Iaccarino and Parviz Moin**, *Numerical simulation of the flow around a circular cylinder at high Reynolds numbers*, International journal of Heat and fluid flow, 2003, Vol. 24.
- [44] **Morkovin, M.V**, *Flow around a circular cylinder. A kaleidoscope of challenging fluid phenomena*, ASME Symp. On Fully Separated Flows, Philadelphia, Pa., 102-119, 1964.
- [45] **Nakayama Y., Boucher R. F.**, *Introduction to Fluid mechanics*, Butterworth-Heinemann, 2000.
- [46] **Norberg C.**, *Effects of Reynolds number and a low-intensity free-stream turbulence on the flow around a circualt cylinder*, Publication No. 87/2, Department of Applied Thermodynamics and Fluid Mechanics, Chalmer University of Technology, 1987.

- [47] **Norberg C.**, *Flow around a circular cylinder: Aspects of fluctuating lift*, Journal of Fluids and Structures, 2001, Vol. 15.
- [48] **Ong L.** and **Wallace J.**, *The velocity field of the turbulent very near wake of a circular cylinder*, Springer-Verlag, 1996.
- [49] **Pattenden R. J.**, **Turnock S. R.**, **Zhang X.**, *Measurements of the flow over a low-aspect-ratio cylinder mounted on a ground plane*, Exp Fluids 39:10-21, 2005.
- [50] **Patrick Beaudan and Parviz Moin**, *Numerical experiments on the flow past a circular cylinder at sub-critical Reynolds number*, Report No. TF-62, 1995.
- [51] **Reichl P.**, **Hourigan K.** and **Thompson M. C.**, *Flow past a cylinder close to a free surface*, Journal of Fluid Mechanics.
- [52] **Roshko A.**, *On the development of turbulent wakes from vortex streets*, NACA Rep. 1191, 1954a.
- [53] **Roshko A.**, *On the drag and shedding frequency of two-dimensional bluff bodies*, NACA Rep. 3169, 1954b.
- [54] **Roshko A.**, *Experiments on the flow past a circular cylinder at very high Reynolds number*, J. Fluid Mech. 10, 345-356, 1961.
- [55] **Ryan Merrick**, **Girma Bitsuamlak**, *Control of flow around a circular cylinder by the use of surface roughness: A computational and experimental approach*.
- [56] **Sadathosseini S. H.**, **Mousaviraad S. M.**, **Firoozabadi B.** and **Ahmadi G.**, *Numerical Simulation of free surface waves and wave induced separation*, Scientia Iranica, 2008.
- [57] **Sarpkaya T.&Isaacson M.**, *Mechanics of Wave Forces on Offshore Structures*, Van Nostrand Reinhold, 1981.
- [58] **Schewe G.**, *Sensitivity of transition phenomena to small perturbations in the flow around a circular cylinder*, J. Fluid Mech. 172,33-46, 1986
- [59] **Shih W.C.L.**, **Wang C.**, **Coles D.** and **Roshko A.**, *Experiments on flow past rough circular cylinders at large Reynolds numbers*, Journal of Wind Engineering and Industrial Aerodynamics, 1993, Vol. 49.
- [60] **Simpson R. L.**, *Junction flows*, Annu Rev Fluid Mech 33:43-415, 2001.
- [61] **Sumner D.**, **Heseltine J. L.**, **Dansereau O. J.P.**, *Wake structure of a finite circular cylinder of small aspect ratio*. Exp Fluids 37:720-730, 2004.
- [62] **Sumer B.M.**, **Christiansen N.** and **Fredsoe J.**, *The horseshoe vortex and vortex shedding around a vertical wall-mounted cylinder exposed to waves*, Department of Hydrodynamics and water resources, Technical University of Denmark, Demark, 1997.

- [63] **Takafumi Nishino, Graham T. Roberts and Xin Zhang**, *Detached-eddy simulation of flow around a circular cylinder in ground effect*, The seventeenth International Symposium on Transport Phenomena, 2006.
- [64] **Taneda S.**, *Experimental investigation of the wakes behind cylinders and plates at low Reynolds numbers*, J. Phys. Soc. Japan 11, 302, 1956.
- [65] **Thompson Joe F., Soni Bharat K., Weatherill Nigel P.**, *Handbook of Grid Generation*, CRC press, 2008.
- [66] **Tritton D.**, *Experiments on the flow past a circular cylinder at low Reynolds numbers*, Journal of Fluid Mechanics, 1959, Vol.6, p. 547-567.
- [67] **Uberoi M.S. & Freymuth P.**, *Spectra of turbulence in wakes behind circular cylinders*, Phys. Of Fluids 12, No. 7, 1359-1363, 1969.
- [68] **Visbal, M.R.**, *Structure of Laminar Juncture Flow*, in AIAA Journal, 29, 8, (1991).
- [69] **Volker Bertram**, *Practical Ship Hydrodynamics*, Butterworth-Heinemann, 2000.
- [70] **Wang J. M., Bi W. T. and Wei Q. D.**, *Effects of an upstream inclined rod on the circular cylinder flat plate junction flow*, Springer-Verlag, 2009.
- [71] **Wei Q. D., Chen G., Du X. D.**, *An experimental study on the structure of juncture flows*, J Vis 3(4):341-348, 2001.
- [72] **Wieselsberger C.**, *Versuche uber den luftwiderstand gerundeter und kantiger korper*, in: L. Prandtl(Ed.), *Ergebnisse Aerodyn. Versuchsanstalt Gottingen*, Vol. II. Liferung, 1923, p. 23.
- [73] **Williamson C. H. K.**, *Sinusoidal flow relative to circular cylinders*, J. Fluid Mech. 155,141-174, 1985.
- [74] **Williamson C. H. K., Brown G. L.**, *A series in $1/\sqrt{\text{Re}}$ to represent the Shouhal-Reynolds number relationship of the cylinder wake*, Journal of Fluids and structures, 1998, Vol. 12.
- [75] **Zdravkovich M.**, *Flow Around Circular Cylinders*, Fundamental Vol. 1, Oxford University Press., Oxford, England, 1997.
- [76] **Zhao Wei, Huhe Ao-de**, *Numerical study of the turbulent flow around a circular pier*, Journal of Shanghai University, 2007.